Non-contact Internal Probing of High Speed Microelectronic Circuits using Electrostatic Force Microscopy

by

Dharmand Noruttun

A Thesis
Submitted to the Faculty of Graduate Studies
in Partial Fulfilment of the Requirements
for the Degree of

Master of Science

Department of Electrical and Computer Engineering
University of Manitoba
Winnipeg, Manitoba
Canada

©Dharmand Noruttun
1997

National Library of Canada

Acquisitions and Bibliographic Services

395 Wellington Street
Ottawa ON K1A 0N4
Canada

Bibliothèque nationale du Canada

Acquisitions et services bibliographiques

395, rue Wellington
Ottawa ON K1A 0N4
Canada

Your file Votre référence

Our file Notre référence

The author has granted a non-exclusive licence allowing the National Library of Canada to reproduce, loan, distribute or sell copies of this thesis in microform, paper or electronic formats.

L'auteur a accordé une licence non exclusive permettant à la Bibliothèque nationale du Canada de reproduire, prêter, distribuer ou vendre des copies de cette thèse sous la forme de microfiche/film, de reproduction sur papier ou sur format électronique.

The author retains ownership of the copyright in this thesis. Neither the thesis nor substantial extracts from it may be printed or otherwise reproduced without the author's permission.

L'auteur conserve la propriété du droit d'auteur qui protège cette thèse. Ni la thèse ni des extraits substantiels de celle-ci ne doivent être imprimés ou autrement reproduits sans son autorisation.

0-612-23444-4

Canadä

THE UNIVERSITY OF MANITOBA

FACULTY OF GRADUATE STUDIES

*****

COPYRIGHT PERMISSION PAGE

NON-CONTACT INTERNAL PROBING OF HIGH SPEED MICROELECTRONIC CIRCUITS USING ELECTROSTATIC FORCE MICROSCOPY

BY

DHARMAND NORUTTUN

A Thesis/Practicum submitted to the Faculty of Graduate Studies of The University

of Manitoba in partial fulfillment of the requirements of the degree

MASTER of SCIENCE

DHARMAND NORUTTUN 1997 (c)

Permission has been granted to the Library of The University of Manitoba to lend or sell copies of this thesis/practicum, to the National Library of Canada to microfilm this thesis and to lend or sell copies of the film, and to Dissertations Abstracts International to publish an abstract of this thesis/practicum.

The author reserves other publication rights, and neither this thesis/practicum nor extensive extracts from it may be printed or otherwise reproduced without the author's written permission.

Abstract

Continuing progress in the microelectronics world has enabled the development of faster, denser and more complicated circuits. These technological advancements have rendered the internal probing of these circuits both difficult and necessary for performance evaluation and failure analysis. Existing probing techniques do not satisfy the combined requirements of high spatial resolution, high temporal resolution, non-invasiveness, high sensitivity, absolute voltage measurement and simplicity. An alternative internal probing technique based on the electrostatic force microscope (EFM) is investigated in this research. The localized electrostatic interaction between a small conducting probe and the test point is used for non-contact measurement of signals on microelectronic structures. A heterodyne technique is employed to measure periodic high frequency digital and sinusoidal signals using the EFM instrument. Vector voltage measurements are performed on the internal nodes of a commercial MMIC amplifier and a MHMIC phase shifter. A nulling technique is used for absolute voltage measurements of sinusoidal signals up to *2GHz*. A pulse sampling heterodyne technique is used for the measurement of arbitrary periodic digital patterns. Measurements of *1Gb/s* digital patterns are demonstrated on the internal nodes of a BiCMOS circuit.

Acknowledgements

I would like to thank Dr. G. Bridges for his help, guidance and support. Dr. Bridges leaves upon me a strong impression of a very kind and understanding person and a dedicated professor and researcher. I consider myself very fortunate for being given the opportunity to work on this project under his supervision.

Thanks also to Dr. D. Thomson and all the members of the SPM group for their assistance and participation in this work. A special thanks to Dr. R. Said for his effort and patience during the completion of this project. His invaluable contribution is very much appreciated.

The assistance of the technical staff in the department is gratefully acknowledged. I would also like to thank H. Pollit-Smith for designing the BiCMOS test circuit.

Finally I would like tc thank all the members of my family. Without their support this work would not have been possible. Special thanks to Anushka for her patience and understanding and for encouraging me during this research work.

The research reported in this thesis was financially supported by the University of Manitoba and the Federal Government's Networks of Centers of Excellence Program/ Micronet.

TABLE OF CONTENTS

Abstract i
Acknowledgements ii
List of Figures vi
List of Tables xiv
List of Acronyms xv

Chapter 1

Introduction 1
1.1 Motivation 1
1.2 Thesis Outline 3

Chapter 2

Review of Internal Probing Techniques 4
2.1 Contact Probes 4
2.1.1 Passive Low Impedance Probes 4
2.1.2 Passive Medium Impedance Probes 7
2.1.3 Active Very High Impedance Probes 7
2.2 Electron-Beam and Optical Probes 8
2.2.1 Electron Beam Testing 8
2.2.2 Electro-Optic Sampling 10
2.2.3 Photoconductive sampling 12
2.3 Electromagnetic Probes 13

Chapter 3

Electrostatic Force Microscopy 16
3.1 Scanning Probe Microscopy 16

3.2 Operating Principle of EFM. 21
3.3 Probe characterization 22
3.3.1 Wire Probe. 23
3.3.2 Micromachined Cantilevers 25
3.4 Deflection Sensors 27
3.4.1 Fiber Interferometer Detection Technique 29
3.4.2 Beam Bounce Detection Technique 32
3.5 Characterization of EFM 36
3.5.1 Spatial Resolution 36
3.5.2 Invasiveness 38
3.5.3 Sensitivity 40
3.6 Voltage Measurement Schemes 42
3.6.1 DC Measurement 42
3.6.2 Measurement of High Frequency Sinusoidal Signals 44
3.6.2.1 Sinusoidal modulation 46
3.6.2.2 Square wave modulation 48

Chapter 4

Vector Voltage Measurement 50

4.1 Introduction 50
4.2 The EFM Probing Instrument 51
4.3 High Frequency Probe Effects 53
4.4 Double-Path Modulation 57
4.4.1 Measurement Results 60
4.5 I/Q Modulation. 72
4.5.1 Measurement Results 79
4.6 Mixer Modulation 87
4.6.1 Measurement Results 91

Chapter 5

Pulse Sampled Waveform Measurement 100

5.1 Measurement Technique 100

5.2 Experimental Set-Up 104

5.3 Measurement on a Microstrip Interconnect 106

5.4 Measurement on a BiCMOS Integrated Circuit 109

5.4.1 Propagation delay measurement 113

5.5 Instrument Sensitivity 115

Chapter 6

Conclusion 120

References 123

List of Figures

Figure **Page**

2.1 Microwave probe types; (a) Coaxial probe, (b) microstrip probe, (c) coplanar probe. 5

2.2 Measurement of a test FET using two ground-signal-ground probes [Strid86]. . . . 6

2.3 Schematic illustration of the principle of pulse e-beam testing. The test circuit is driven by a repetitive stimulus $v_c(t)$ which is synchronised with the beam blanking control signal that generates the electron pulses. Analysis of the secondary electrons emitted at the test point permits the measurement of $v_c(t)$ [Winkler90]. . 9

2.4 Possible probing geometries of coplanar devices for electro-optic probing; (a) probe tip geometry for direct probing of the electric field in a linear electo-optic substrate, (b) probe tip geometry for external probing of the stray field from the coplanar lines. 10

2.5 Schematic of the electro-optic probing [Takahashi95]. A polarised optical beam is focused into an electro-optic crystal placed in close proximity over a test point. 11

2.6 Top view illustration of a photoconductive sampling probe with a $5\text{-}\mu m$ high Ti tip [Pfeiffer95]. 13

2.7 Reactive near-field probing of a microstrip line by capacitive coupling of the electric field with the centre conductor of a coaxial probe.. 14

2.8 Inductive near-field probing; (a) magnetic field coupling to a double loop probe, (b) schematic of a double-loop probe [Osofsky 92].. 14

2.9 Block diagram of a field measurement system [Gao 95]. The probe is scanned over a planar test circuit. 15

3.1 Schematic illustration of the scanning tunneling microscope. An enlarged view of the tip-surface interaction in a constant current mode is also shown.. 17

3.2 Schematic illustration of the magnetic force microscope [Rugar 90]. 20

3.3 Illustration of the Electrostatic Force interaction between conducting probe and a test point. 21

3.4 Photograph of a typical wire probe used in this research. The left (probing) end is free to vibrate while the other end is attached to the center conductor of a coaxial cable. 23

3.5 Frequency response of a wire cantilever. Theoretical data is calculated for f_r = *1.168 kHz, Q= 272*. 25

3.6 (a) Schematic illustration of a micromachined cantilever coated with a gold metal layer; (b) SEM micrographs of a Si_3N_4 cantilever (top) and the pyramidal tip (bottom) [Wiesendanger 94]. 26

3.7 Frequency response of a gold coated commercial Si_3N_4 cantilever. The theoretical data is calculated with f_r = *12.275 kHz* and Q = *32*. The experimental data was processed using a 10-pt smoothing routine and every tenth data point is dis played in the graph. 27

3.8 Simple model for the capacitance between a probe tip and a sample. The tip is modelled as a sphere. 28

3.9 Schematic illustration of the fiber interferometer detection technique. 29

3.10 Enlarged view of the core region of the fiber over a cantilever's surface showing multiple reflections of the light beam between the fiber-end and the cantilever [Mulhern 91]. 30

3.11 Normalized output of the interferometer as a function of the fiber-cantilever spacing D for different values of r_2. An air-glass interface is assumed with r_1=*0.2* and the wavelength of light λ = *845nm*. 31

3.12 Illustration of the beam bounce detection technique. A laser beam is focused onto the probing end of a cantilever probe and then reflected into a position sensitive detector (a split photodiode detector). 33

3.13 Detection of the optical beam as it is deflected. The shift in the optical spot is measured from the difference of the signals from the two photodiode detectors. The parameter, w, completely defines the beam power distribution and it is described in [3.12]. 34

3.14 Calculated force per unit area induced on a ground plane as a function of the radial distance from the tip axis. The tip is positioned $0.1\mu m$ above the circuit surface [Said 95]. 37

3.15 The vertical force on the probe tip and its first derivative as the probe is scanned over a $3\mu m$ wide interconnect line with a tip to sample spacing of $1\mu m$ [Said 95]. 38

3.16 Resistive, capacitive and inductive loading effects from a probing device. 39

3.17 Implementation of the nulling technique for the measurement of a local DC potential. 44

3.18 Schematic illustration of the heterodyne vector voltage measurement using a sinusoidal modulation scheme. 46

3.19 Relative probe deflection as a function of probe-circuit phase difference for the cases when $A=V_c$, $A < V_c$ and $A > V_c$. 47

4.1 (a) Photograph of the EFM probing instrument; (b) close-up view of a micromachined probe positioned over a test circuit. 52

4.2 (a) Circuit model for probe-circuit arrangement, (b) resulting circuit assuming the coupling capacitance $C(x,y,z)$ as an open circuit. 54

4.3 Simulated return loss, S_{11}, as a function of the normalized open-circuit length l/l. 55

4.4 Return loss, S_{11}, measured on a network analyzer as a function of frequency for a fixed line length. 56

4.5 Probe matching at a frequency f_0 by adjusting the effective length of open circuit line and using a directional coupler to measure the reflected power. 57

4.6 Schematic illustration of the double-path square wave modulation scheme. 58

4.7 Schematic representation of the measurement system used for vector voltage measurement at *1GHz* using a double-path square wave modulation scheme. . . . 60

4.8 Forward reflection parameter (S_{11}) of thru-line as measured on a network analyzer. 61

4.9 Forward transmission parameter (S_{21}) of thru-line as measured on a network analyzer.. 62

4.10 Normalised deflection signal as the probe signal parameter A is varied for test circuit signal amplitudes of *0.206V* and *0.320V*. 63

4.11 Probe parameter A as a function of circuit signal amplitudes V_c. A straight line is fitted onto the measured data points. 64

4.12 Normalised deflection signal as the phase of the probe signal is varied. The phase of the test circuit signal (V_c = *0.206V*) was initially determined as f_c = 238° and the probe signal adjusted to null the deflection with ϕ_p set as 238°. Both the measured and the theoretical responses are plotted.. 65

4.13 Photograph of the Texas Instrument Low Noise Amplifier used as a test circuit in EFM vector voltage measurements. The integrated circuit is packaged by bonding to the microstrip lines.. 66

4.14 Forward transmission parameter (S_{21}) of Ti-LNA as measured on a network analyzer.. 67

4.15 Forward reflection parameter (S_{11}) of thru-line as measured on a network analyzer. 67

4.16 Texas Instrument Low Noise Amplifier (TI LNA); microphotograph of the circuit (top) and the circuit schematic representation of the MMIC (bottom). 68

4.17 Measurement system for contact probing with an active probe (Picoprobe). Direct contact is made by a fine tungsten tip to a test point on the circuit.. 69

4.18 Calibration curve for active contact probe measurement system at *1GHz*. Results are plotted from two measurement attempts and a straight line is fitted

through the measured points.. 70

4.19 Schematic representation of the I/Q Modulator. The RF signal can be represented as a vector sum of the two orthogonal I and Q components. 73

4.20 Illustration of square wave modulation using the I/Q modulator for the case when $0^o < \phi < 90^o$.. 74

4.21 Characterization of the performance of the I/Q modulator. LO frequency was 881MHz. The peak-to-peak magnitude of the RF output was measured as the DC voltage at port I was varied with port Q grounded. A straight line is fitted through the measured data points.. 75

4.22 Block diagram of the measurement system using the I/Q modulator for vector voltage measurement at *881MHz*. 79

4.23 Determination of the circuit signal phase by locating the two null points. Both the measured data and the theoretical fit are displayed. 80

4.24 Experimental and theoretical response of the probe deflection as a function of the phase of the probe signal ϕ_p with $\phi_c = 327^o$ and the probe parameter $A = V_c$. 81

4.25 Theoretical response of the probe deflection at *fr* as the probe parameter *A* is varied for the cases when V_c = *0.05, 0.1, 0.2, 0.3* and 0.*4 V*. 82

4.26 Experimental nulling curves where the probe deflection is plotted as a function of the probe parameter *A* for V_c = *0.08, 0.12, 0.15, 0.20* and *0.25 V*. 83

4.27 Calibration curve for amplitude measurement. The probe parameter A is plotted as a function of the circuit signal amplitude for r_1 = *1.6, 1.7* and *1.8*. A straight line is fitted on the experimental data.. 84

4.28 Capacitive coupling effect between a micromachined probe and a device under test. A static equivalent circuit model for the coupling effect is also given.. 85

4.29 Functional schematic of M1H mixer [RELCOM]. 87

4.30 Modulator circuit for MIH mixer. A low frequency square wave signal is used to modulate the high frequency signal. The input impedance of the sources used

is 50Ω . . . 87

4.31 Mixer performance. The peak-to-peak amplitude of the high frequency carrier is plotted as a function of a DC modulating signal level. . . . 89

4.32 Experimental set-up for heterodyne vector voltage measurement using a mixer square wave modulation scheme. . . . 90

4.33 Relative deflection, Δz, of the probe as a function of the probe parameter, A, with $V_c = 171mV$ and $\phi_p = \phi_c$. . . . 91

4.34 Calibration curve showing A as a function of V_c. A straight line is fitted through the results obtained from two separate experiments.. . . . 92

4.35 The normalised probe deflection as a function of the probe-circuit phase difference, $[\phi_p - \phi_c]$. Both the measured and theoretical results are normalised.. . . . 92

4.36 Microphotograph of the MHMIC phase shifter (top) and its circuit schematic (bottom). . . . 95

4.37 The forward reflection and transmission parameters S_{11} (top) and S_{21} (bottom) of the phase shifter with $V_{bias} = -2.0V$. . . . 96

5.1 (a) Example of a periodic voltage waveform $v_c(t)$ to be measured, (b) sampling signal $v_s(t)$ with same periodicity as $v_c(t)$. Here $v_s(t)$ is sampling the test signal $v_c(t)$ at the instant $t = \tau$. . . . 102

5.2 Block diagram of the pulse sampling technique. A photograph of a test circuit is shown with the EFM probe positioned over a test point of interest. . . . 102

5.3 Generation of the test circuit ($v_c(t)$) and probe pulse sampling ($v_p(t)$) signals.. . . 105

5.4 Sampling pulse waveform $v_p(t)$ with a repetition frequency of $125MHz$ as captured on an oscilloscope. Some non-idealities in $v_p(t)$ are present. The FWHM of the pulse is estimated at $250ps$. . . . 106

5.5 Measurement on a microstrip interconnect line at 125 Mb/s; (a) Applied digital pattern from generator measured on a oscilloscope (1010100110010101), (b) waveform measured using EFM.. . . . 107

5.6 Measurement on a microstrip interconnect line at 1 Gb/s; the applied digital pattern $v_c(t)$ (01011001), the EFM result and convolution of $v_c(t)$ with $v_s(t)$ are shown. 107

5.7 Measurement on a microstrip interconnect line at 1 Gb/s (Enlarged view of a rising edge); Rise time of applied pattern ~ 180 ps compared with rise times of measured waveform and convolved result (~380 ps).. 108

5.8 Measurement on a microstrip interconnect line at 1 Gb/s; (a) Applied digital pattern $v_c(t)$ (0011001010111100), (b) waveform measured using EFM (3 point smoothing). 109

5.9 Microphotograph of Nortel BiCMOS inverter chain showing EFM probe. The circuit schematic is at the bottom with the inset showing the structure of the CMOS inverters. 110

5.10 Measurement of an 8-bit 1 Gb/s digital pattern (01100101) at test pads A, C and D. Results from active contact probing and EFM (non-contact) probing are presented for each test point. 111

5.11 Measurement of an 4-bit 0.5 Gb/s digital pattern (1010) at test pads A. Results from (a) Cadence SpectreS simulation, (b) EFM probing and convolution of the simulated waveform shown in (a) with sampling pulse shown in Figure 5.3, (c) active contact probing are shown. 113

5.12 Measurement of an 4-bit 0.5 Gb/s digital pattern (1010) at test pads A, C, E and G. Results from (a) Cadence SpectreS simulation, (b) EFM probing and (c) active contact probing are shown. 114

5.13 Cadence simulation of the inverter chain without test pads. Simulated waveforms at points in the circuit corresponding to test pads A, C, E and G are shown. 115

5.14 Delay measurements on a microstrip interconnect line. (a) Applied signal delayed by 10, 20, 50 and 100 ps as measured on an oscilloscope, (b) waveforms measured by EFM, (c) and (d) show an enlarged view of the curves in (a)

and (b).. 116

5.15 Plots showing the results obtained by measuring the rising edge of the same signal 10 times.. 117

5.16 (a) Repeated sampling (51 times) of points at time t = *1.9 ns* and *3.0 ns* plotted over *0-8ns* pattern. (b) Set of four measurements (101 data points in each) at t = *3.0 ns* with data in (i), (ii) and (iii) averaged 1000 times and those in (iv) averaged 10000 times. (AU stands for arbitrary units).. 117

5.17 Repeated sampling (81 times) of signal at time t = *1.0, 2.35, 4 ns* plotted over 8ns long pattern.. 119

List of Tables

Table **Page**

1 Vector waveform measurement of TI-LNA at *1GHz* 71

2 Forward transmission parameter, S_{21}, of the TI-LNA. 71

3 Response of the modulator as a function of I and Q modulating signals 76

4 Phase measurement using I/Q modulation at *881MHz* 81

5 Measurement on TI-LNA using I/Q Modulation. 86

6 Vector voltage measurement on TI-LNA at *2GHz*. 93

7 Measurement of TI-LNA S_{21} at *2GHz* 94

8 S-parameters of the phase shifter at *1.7GHz*. *96*

9 EFM and contact probing results at *1.7GHz*. 97

10 Comparison of the relative phase shift ($\Delta\phi$) at *1.7GHz*. 98

11 HP 80000 Data Generator System. 104

List of Acronyms

AFM	Atomic Force Microscopy/Microscope
EFM	Electrostatic Force Microscopy/Microscope
LNA	Low Noise Amplifier
SPM	Scanning Probe Microscopy/Microscope
STM	Scanning Tunneling Microscopy/Microscope

Chapter 1

Introduction

1.1 Motivation

Rapid advances in the microelectronics field have enabled the development of faster, denser and more complicated integrated circuits (ICs). The ability to test the performance of a particular technology underlies the progress in developing that technology. It is therefore important to develop appropriate tools to accurately evaluate the performance of these circuits and devices. The increasing chip complexity have made circuit modeling difficult and the prediction of a circuit behaviour by computer simulations alone are inadequate. Accurate measurements for device evaluation are therefore essential. On-chip waveform measurements are often required for complete characterization of a device and for failure analysis purposes. Measurements within a circuit are carried out using internal probing techniques with the device driven by an external source.

The complexity of very-large-scale-integrated (VLSI) circuits present a number of challenges during testing at the chip level. The ideal probing technique would enable measurements with high temporal and spatial resolution, high sensitivity and low invasiveness. The measurement method should also be simple to operate and enable accurate extraction of voltage levels. Currently available instruments do not completely satisfy these requirements. It is therefore important to develop alternative probing techniques. Present measurement requirements demand probing techniques capable of measuring GHz signals with sub-micron spatial resolution and mV sensitivity.

In this research, the application of the electrostatic force microscope for non-contact internal probing of high speed microelectronic circuits is investigated. The electrostatic force microscope (EFM) is a member of the family of scanned probe microscopes which are capable of measuring features and properties of surfaces with extremely high spatial resolution. Different techniques, based on signal mixing, are developed to enable measurements of high frequency signals using the electrostatic force microscope. Measurement of high frequency sinusoidal signals as well as periodic digital waveforms are demonstrated using the instrument.

The research project presented in this thesis forms part of an ongoing research on the use of an EFM-based instrument for non-contact probing of integrated circuits. This research project was initiated in the department a few years ago and a number of professors, post doctoral fellows and graduate students are involved. Two types of EFM instruments were used in this project. The main contributions from the members of the group are mentioned here. The first instrument, based on a fiber-interferometer deflection sensor, was constructed by Raa Said. The second stage which employs a beam bounce deflection sensor was designed and constructed by Richard Qi. Some of the sections dealing with the EFM characterization in chapter 3 are obtained from Raa Said's PhD thesis [Said 95]. The investigation of the spatial resolution, for instance, requires accurate modeling of the probe-circuit interaction and this work has already been completed by a member of the group [Said 95]. These sections are included for the sake of producing a more complete document. The test circuit use for on-chip sampling measurements (chapter 5) was designed by Hugh Pollit-Smith.

The author's main contribution in the project was the analysis and implementation of the three modulation techniques in the heterodyne vector voltage measurement discussed in chapter 4. The author was also responsible for the implementation of a high frequency, narrow pulse generation system for on-chip pulse sampling measurements presented in chapter 5.

1.2 Thesis Outline

A brief outline of the thesis is presented in this section. In chapter 2, some of the common techniques used for testing high speed integrated circuits and devices are briefly discussed. The operating principle as well as the capabilities and limitations of these instruments are mentioned.

The electrostatic force microscope (EFM) is introduced in chapter 3. The origin of this microscope is presented first and then the principle behind the EFM instrument is discussed. The cantilever probes and their deflection sensors used in the instrument are characterized. The performance of the instrument in terms of spatial resolution, voltage sensitivity and invasiveness are discussed. A heterodyne technique for high frequency vector voltage measurement based on amplitude modulation is described.

Chapter 4 describes the implementation of a heterodyne technique for high frequency vector voltage measurement. The difficulties encountered during high frequency measurements are introduced. The implementation of different modulation schemes are described. Experimental results from measurements performed on the internal nodes of a MMIC and a MHMIC are also presented.

In chapter 5 an on-chip sampling technique for probing periodic arbitrary waveforms is introduced. The technique is demonstrated by measuring high speed digital patterns on the internal node of a BiCMOS circuit.

Finally a conclusion of the thesis is provided in chapter 9.

Chapter 2

Review of Internal Probing Techniques

A number of diagnostic tools are available for the measurement of electrical signals at the internal nodes of circuits. In this chapter some of the common techniques used for testing high speed integrated circuits and devices are briefly discussed.

2.1 Contact Probes

Contact probing is a simple technique used for measuring internal signals of an integrated circuit by directly touching the sharp tip of a conducting probe with the test point. They have been used in the measurement of both microwave and high-speed digital circuits. Three main types of contact probes are available: passive low impedance wafer probes, passive medium impedance probes and active very high impedance probes.

2.1.1 Passive Low Impedance Probes

Microwave wafer probes are low impedance passive probes. They provide very high bandwidth and are often used in conjunction with a network analyzer for single or multiple port measurement. These probes allow measurement to be made at the wafer level as opposed to the input/output connections of a packaged device accessed by a conventional network analyzer. Furthermore the cost of packaging devices as their operating frequen-

cies extend into the *GHz* range can become very expensive and device testing at the wafer level becomes an attractive solution. High frequency probes up to 120 GHz are commercially available [GGB] and microwave probes are widely used in FET, passive element and MMIC characterization. These measurements enable database generation used for inputing device/subcircuit parameters into a circuit simulator for parameter optimization and process control [Jones 87].

Measurements at *GHz* frequencies with wafer probes require the use of controlled impedance probes that provide the characteristic impedance (usually 50Ω) down to the wafer level connection. Minimal inductive and capacitive parasitic effects are desirable to avoid pulse distortion and timing errors. Microwave probes are commercially available in coaxial, microstrip and coplanar configurations [Rabjohn 86]. Coaxial probe tips are formed by extending the centre conductor beyond the outer shield and sharpening the probing tip as shown in Figure 2.1(a). A 50Ω impedance is provided to within a few millimetres of the tip. In the microstrip configuration a short needle probe is attached to the microstrip feed line. The main drawback of these type of probes are the parasitic inductance of the tip and the lack of an RF ground close to the test point.

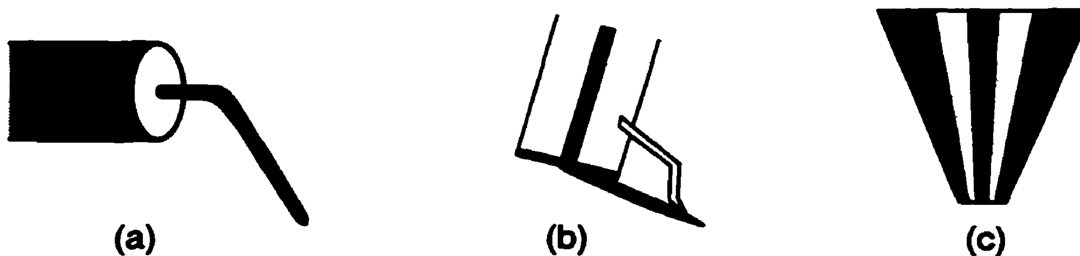

Figure 2.1: Microwave probe types; (a) Coaxial probe, (b) microstrip probe, (c) coplanar probe.

In a coplanar waveguide the signal line is located between two ground lines on the same side of a substrate. The lines are tapered in width to match the probe point to the device-pad size. Direct contact is made at the tip end avoiding the problems associated with inductive needles. The main disadvantage of coplanar probes are their size which limits the number of probes that can be used on a circuit.

The use of coplanar probes in the characterization of a test FET is illustrated in Figure 2.2 [Strid 86]. In this set-up the S-parameters of the device were obtained up to *26GHz* with the aid of a network analyser.

In contact wafer probing, circuits have to be especially designed in order to accommodate the probes. This limits the number test points which may not be adequate for complete characterization of a circuit. Moreover direct measurements at internal test points are not feasible as the probe low impedance load would disturb the normal operation of the device.

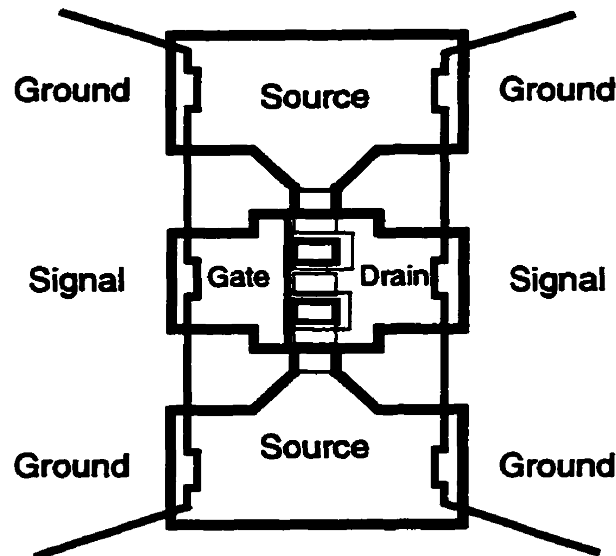

Figure 2.2: Measurement of a test FET using two ground-signal-ground probes [Strid 86].

A low-loss microwave wafer probe with a GaAs directional time-domain reflectometer (TDR) IC directly mounted on the probe has been used in vector network analysis to *120GHz* [Yu 93]. Time-domain on-wafer measurement with a *500GHz* bandwidth has been reported [Shakouri 93]. A nonlinear transmission line (NLTL) pulse generation system was used to generate picosecond transients and a GaAs IC attached to the probe served as a TDR sampler.

2.1.2 Passive Medium Impedance Probes

Resistive divider probes are examples of passive medium impedance probes. An example of a commercial resistive divider probe has a *450Ω* resistor in the probing tip [Cascade]. In a *50Ω* system the probe results in a 10:1 attenuation and the input impedance is *500Ω*. The measurement bandwidth of these probes lie in the DC to *10GHz* range. Probes with input impedances up to *5kΩ* are also available. The medium impedance probes can be used for internal probing in *50Ω* systems. One important limitation is the larger capacitive loading from these probes.

2.1.3 Active Very High Impedance Probes

Internal signals of a device can also be measured by active probes as compared to the passive ones discussed so far. Active probes provide very high input impedance but are limited in bandwidth and dynamic range. A commercially available active probe (Picoprobe) is used in this research [GGB]. The input connects directly to the unprotected gate of an MOS transistor through a probing needle making the probe sensitive to destruction by electrostatic discharge. These needles are usually made of tungsten and can be sharpened to less than *0.5μm* point radius. One example of this type of probe has an input capacitance load of *0.04pF* and a DC to *1GHz 3-dB* bandwidth. There is usually a trade-off between bandwidth and loading.

2.2 Electron-Beam and Optical Probes

2.2.1 Electron Beam Testing

Electron beam (e-beam) testing is a commercially available tool for internal voltage measurement of integrated circuits and has been applied in industrial environments over the past two decades. The principle behind e-beam testing is the emission of secondary electrons by the probe area when focused with a beam of primary electrons. The analysis of the secondary electrons in terms of their energy by a retarding grid spectrometer enables the determination of the voltage on the internal test point being probed. A feedback loop is usually used to maintain the detector signal constant by adjusting the grid potential which then tracks the circuit voltage.

High frequency measurement is possible by sampling the test signal with short electron pulses and a schematic diagram illustrating this technique is shown in Figure 2.3 [Winkler 90]. The captured signal from the secondary electrons is usually very small and a repetitive sampling technique is needed to extend the temporal resolution of the measurement as compared to a real time system. Thus a repetitive stimulus $v_c(t)$ is also needed to drive the test circuit. The electron pulses are generated by chopping the beam with a blanking capacitor. The beam blanking control signal is synchronized with the repetitive circuit signal so that the same voltage is sampled at a fixed phase relation. The entire circuit signal can be mapped by shifting the phase relation between $v_c(t)$ and the e-beam pulses.

Temporal resolution of the technique depends primarily on the e-beam pulse width. The e-beam probing technique is noninvasive especially when low energy probe beams are used although radiation damage and charge trapping are possible at higher energies. Spatial resolution under $1 \mu m$ can be routinely achieved [Corsi 94]. E-beam testing is a powerful tool for the high frequency internal diagnostics of circuits. However the instru-

ment is expensive and complicated to operate. Measurements are made in vacuum and therefore complicated test circuit fixtures are needed. Furthermore extensive calibration procedures are necessary for absolute voltage measurement.

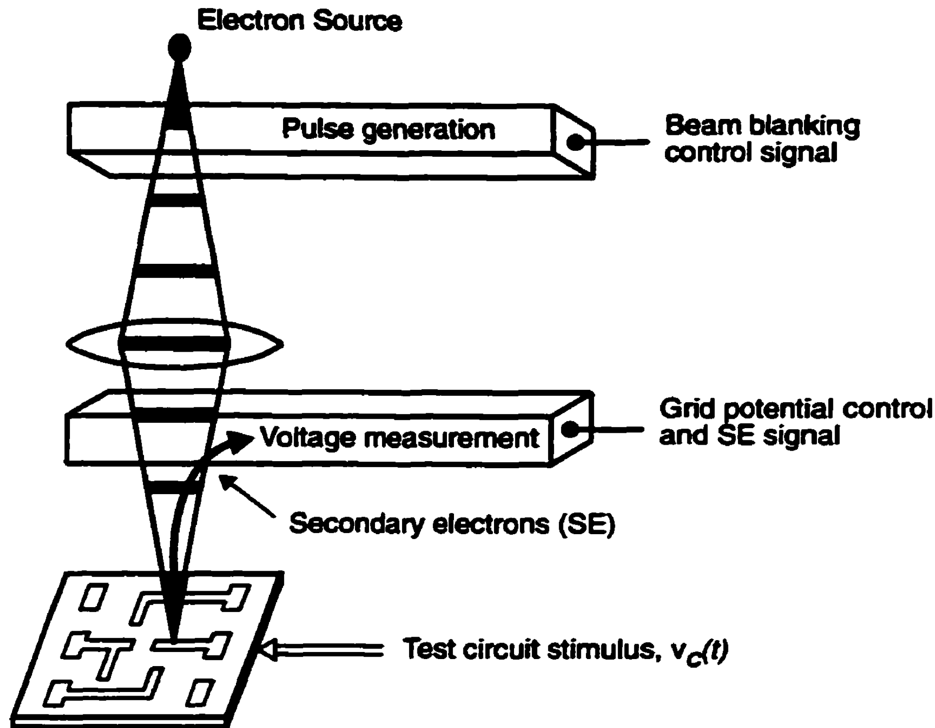

Figure 2.3: Schematic illustration of the principle of pulse e-beam testing. The test circuit is driven by a repetitive stimulus $v_C(t)$ which is synchronised with the beam blanking control signal that generates the electron pulses. Analysis of the secondary electrons emitted at the test point permits the measurement of $v_C(t)$ [Winkler90].

Photoemission probing is a technique similar to the e-beam probing [Clauberg 90]. The test point on a circuit is focused with a laser beam resulting in the emission of secondary electrons. The energies of these electrons are then analyzed to obtain the test signal. Both real-time (continuous laser beam) and sampling mode (pulsed laser beam) measurements are possible.

2.2.2 Electro-Optic Sampling

This technique employs the electro-optic effect which is the change in the birefringence properties of certain crystals when placed in an electric field. This results in a change of the polarization of light propagating through such a crystal. By monitoring the polarization of an optical probe beam, the electric field resulting from voltages on a circuit can be investigated. Since the optical probe is spatially localized and can be focused to $\sim 1 \mu m$ diameter the technique can be applied to internal probing of ICs [Wiesenfeld 90]. Substrate materials that exhibit a linear electro-optic effect such as GaAs and InP can be probed directly as shown in Figure 2.4(a). An indirect probing configuration is shown in Figure 2.4(b) where an electro-optic crystal, typically $LiTaO_3$, is used as the probe tip and placed in close proximity to the test point. This would be the case for nonelectro-optic substrate such as silicon.

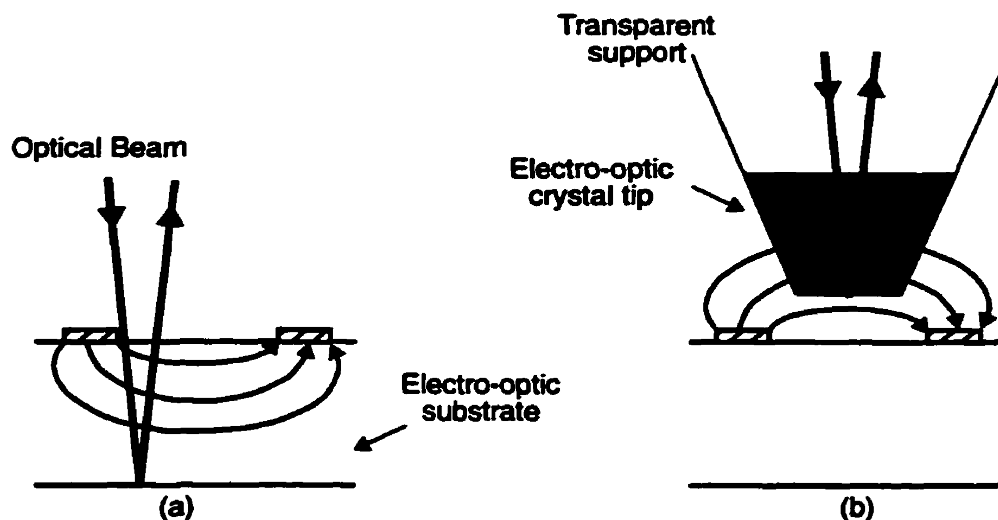

Figure 2.4: Possible probing geometries of coplanar devices for electro-optic probing; (a) probe tip geometry for direct probing of the electric field in a linear electo-optic substrate, (b) probe tip geometry for external probing of the stray field from the coplanar lines.

The principle of electro-optic probing is depicted in Figure 2.5 [Takahashi 95]. An electro-optic crystal probe is positioned over some test point and a laser beam is focused into the probe and reflects off a mirror attached to the bottom. The polarization of the laser

beam depends on the circuit signal after passing through the crystal. The use of polarizing beam splitter together with the photodetector enables the determination of the circuit signal by a lock-in amplifier or an oscilloscope. A continuous laser beam is used in a real time system while measurement of high speed signals involves a sampling technique where the optical beam is a train of short pulses that acts as sampling gates. As in all repetitive sampling techniques the signal to be measured on the DUT is repetitive. Advances in laser technology have enabled the generation of very short pulses, less than *100fs* in some of the fastest systems, which provides a very high temporal resolution.

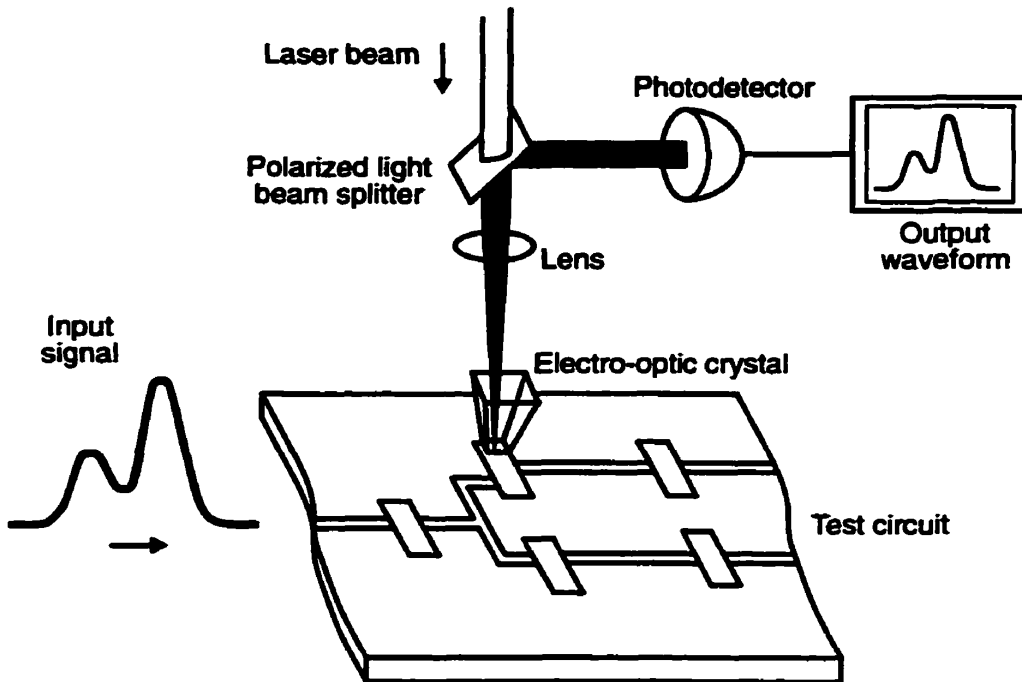

Figure 2.5: Schematic of the electro-optic probing [Takahashi95]. A polarised optical beam is focused into an electro-optic crystal placed in close proximity over a test point.

Electro-optic probing have been used in a number of applications such as the internal field probing of sub-micron MMIC devices [David 95] and the measurement of internal signals of integrated circuits [Wiesenfeld 90]. The electro-optic technique has also been utilized in the characterisation of ultrafast pulses on MMIC devices using a time domain network analyser system [Lee 90]. One example of a reported sampling system has a frequency bandwidth of *10GHz* and a minimum detectable voltage of $0.4\ mV/\sqrt{Hz}$ [Taka-

hashi 95]. Temporal resolution is determined mainly by the pulse width in the sampling beam although factors such as response time of the electro-optic effect and transit time effects are relevant as well especially for subpicosecond resolution [Wiesenfeld 90]. Spatial resolution of the technique depends on the spot size of the focused beam and a resolution of $0.5\mu m$ has been achieved in a direct electro-optic probing system [David 95]. However the electro-optic system suffers from limited spatial resolution when its application is extended to silicon-based circuits since it relies on fringing effect of the circuit field into the probing crystal. Accurate probe positioning is difficult in indirect probing and the measurement becomes sensitive to crosstalk effects.

Electro-optic probing operates in a non-contact mode and measurements are expected to be non-invasive. While this is true for direct probing the close placement of the probe tip in indirect probing may lead to the perturbation of the electric waveform due to its high permittivity resulting in circuit malfunction and measurement errors [Mertin 93]. Although the technique provides excellent temporal resolution it remains a complex and expensive technique as far as the laser system is concerned. Extensive calibration steps are required for absolute voltage measurement as the technique senses the electric fields from the test signals.

2.2.3 Photoconductive sampling

In photoconductive (or optoelectronic) sampling techniques photoconductive switches are used to measure internal signals of high speed circuits and devices. Photoconductive switches are usually fabricated on doped semiconductor material with a semiconductor gap between metal electrodes. A metal-semiconductor-metal photoconductive sampling probe which integrates the photoconductive switch is illustrated in Figure 2.6. In this case a Ti tip is used to contact test points in a circuit at the probing end.

A reported switch has a high impedance, about $30M\Omega$, under normal condition which then drops to $1k\Omega$ when the semiconductor gap is optically excited [Pfeiffer 95]. The use

of narrow laser pulses to excite the switch allows high speed signals to be sampled by this technique. A laser beam is usually split into two parts with one beam focused on a biased photoconductive switch to generate the high frequency electrical excitation of the device under test. The other beam is used to excite the probe switch and the phase variation between the two laser beams allows the signal on a circuit to be sampled.

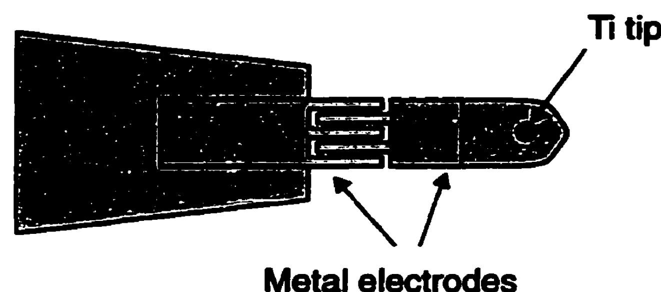

Figure 2.6: Top view illustration of a photoconductive sampling probe with a $5\text{-}\mu m$ high Ti tip [Pfeiffer 95].

Temporal resolution is limited by the lifetime of the charge carriers in the semiconductor and a resolution of $2.7ps$ has been reported [Kim 93]. Voltage sensitivity in the μV range has also been achieved and spatial resolution is limited by the diameter of the probing tip. Loading in this case is only due to the capacitive effect of the switch/contact area.

In another measurement system photoconductive switches form an integral part of a circuit and the photoconductive sampling technique has been used to characterize MMICs in the GHz range [Lee 90].

2.3 Electromagnetic Probes

Electromagnetic probes are used in the reactive near-field probing of planar circuit surfaces. The technique relies on the capacitive or inductive coupling between the near-field of the test circuit and miniature probes. In capacitive near-field probing the fringing electric field from a circuit is investigated. As the probe is positioned close to the test point a signal is induced in it which can then be measured. The principle behind this technique

is illustrated in Figure 2.7 where the centre conductor of a coaxial cable acts as the probe. This probing method has proved to be useful in the design of microwave circuits and for antenna diagnostics [Gao 96]. The shrinking dimensions of MMIC's have created the need for probes capable of high spatial resolution. The use of micromachined probes in near-field probing have been reported with a spatial resolution of *15μm* [Bridges 92a].

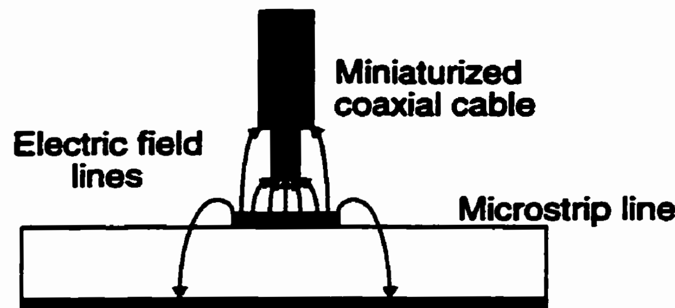

Figure 2.7: Reactive near-field probing of a microstrip line by capacitive coupling of the electric field with the centre conductor of a coaxial probe.

The principle behind inductive near-field probing is the coupling between the magnetic field lines from a test circuit and a loop probe. This is demonstrated in Figure 2.8. Also shown in Figure 2.8 is a schematic of a double loop magnetic field probe [Osofsky 92]. The double loop improves the performance of the probe by minimising the coupling from near-uniform fields arising from distant sources.

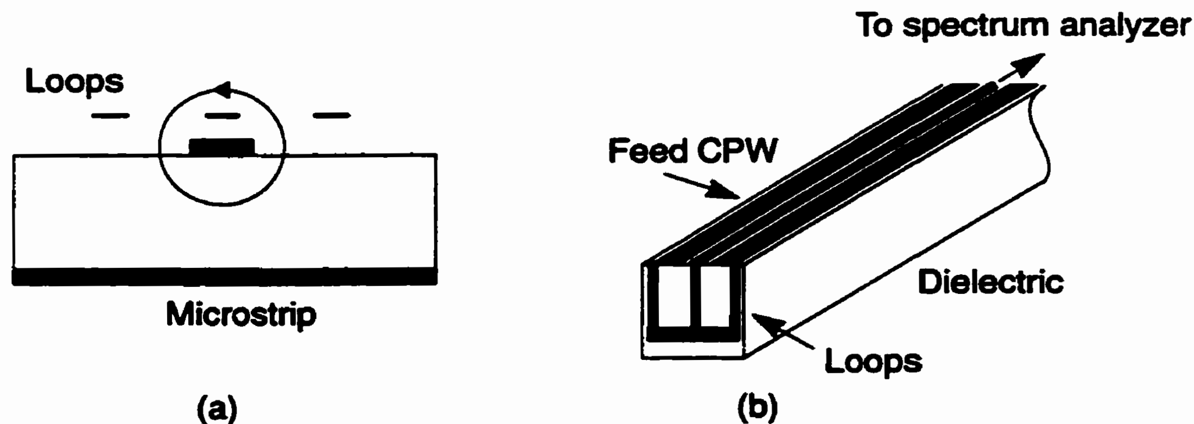

Figure 2.8: Inductive near-field probing; (a) magnetic field coupling to a double loop probe, (b) schematic of a double-loop probe [Osofsky 92].

A miniature magnetic field probe has been used for measuring surface current distribution on planar circuits in the *5-20GHz* band [Gao 95]. The block diagram of a near-field measurement system is shown in Figure 2.9. The probe is mounted on a table and is movable in three dimensions. As it is scanned over a circuit under test the induced signal is measured by a network analyzer.

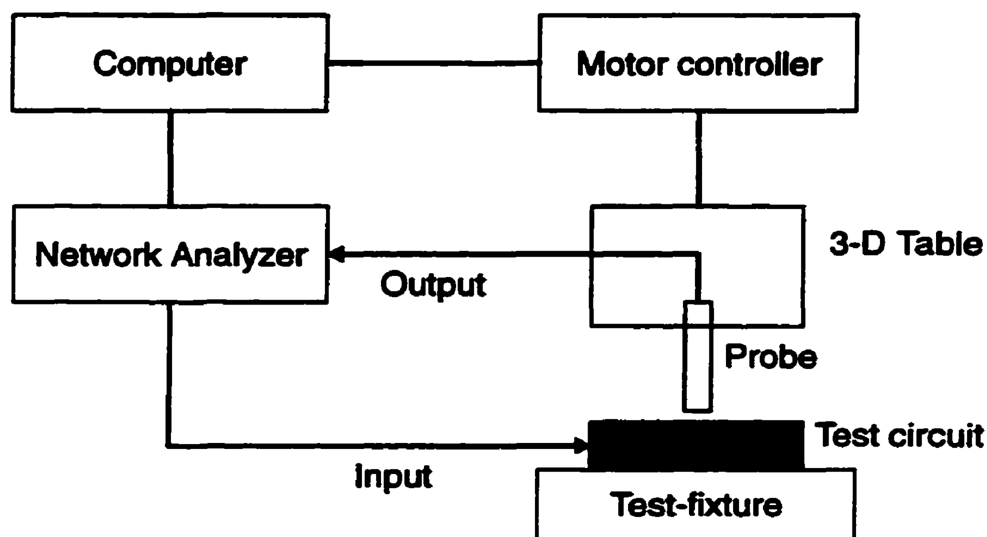

Figure 2.9: Block diagram of a field measurement system [Gao 95]. The probe is scanned over a planar test circuit.

Near-field probing is a simple method capable of high frequency measurement with a large bandwidth. The technique, however, suffers from limited spatial resolution and absolute measurement is impossible without calibration.

Chapter 3

Electrostatic Force Microscopy

Electrostatic force microscopy (EFM) is a member of the growing family of scanned probe microscopy (SPM) techniques. The origin of these microscopes is presented first and then the EFM instrument used in this research is described. The operating principle as well as the capabilities and limitations of the instrument are discussed.

3.1 Scanning Probe Microscopy

Scanning probe microscopes are a set of instruments used for resolving features and properties of surfaces on a microscopic scale [Wickramasinghe 89]. Originally developed to measure surface topography, SPMs have proved to be useful in a variety of applications. They have been used to investigate the mechanical, electrical, magnetic and thermal properties of surfaces. Measurement in all SPM instruments involves the near-field interaction between a small probe and a surface under investigation. Extremely high spatial resolution is achieved by using a very sharp probe tip with a radius of curvature on the order of a few nanometers and by keeping the tip-to-sample spacing within a nanometer.

Conventional techniques used for studying the morphology of surfaces such as optical microscopes and scanning electron microscopes (SEM) suffer from resolution limitations due to diffraction effects (the Abbe limit). SPMs provide an alternative tool that overcomes such limitations. Contrary to optical and electron microscopes SPM can also pro-

vide measurement in three dimensions.

The scanning tunneling microscope (STM) was the first SPM instrument developed and enabled measurements with atomic resolution for the first time [Binnig 82]. The operation of the STM is remarkably simple. As outlined in Figure 3.1, a sharp conducting tip is scanned over a conducting sample. A bias voltage is applied between the tip and the sample resulting in a tunneling current as the tip is brought to within a few Angstroms of the sample surface. The motion of the tip is controlled on such a fine scale by piezoelectrics (materials that deform very slightly in the presence of an electric field). Due to its exponential dependence on the tip-sample spacing, the tunneling current provides a very sensitive measure of separation. The instrument is usually operated in a constant current mode by using the tunneling current in a feedback loop. As the tip is scanned in a raster pattern the feedback loop causes the tip to track the sample surface with very high precision and the control signal provides the image data.

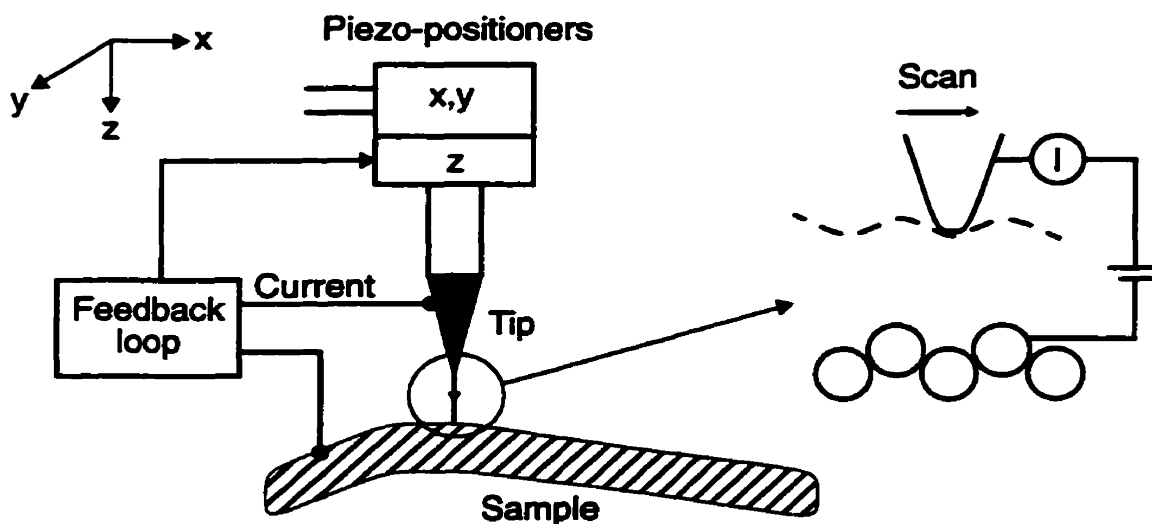

Figure 3.1: Schematic illustration of the scanning tunneling microscope. An enlarged view of the tip-surface interaction in a constant current mode is also shown.

The outstanding results from the STM generated a lot of interest in the technique and a whole new set of instruments, the scanning probe microscopes, were developed. The

atomic force microscopy (AFM) was developed to overcome an important limitation of the STM which is the need for conducting surfaces [Binnig 86]. Similar to the STM, the AFM operates by scanning a sharp tip over a sample. However it is the force acting on the probe as the tip interacts with surface that is monitored. In this method the tip is found at the end of a long cantilever with a low spring constant. The tip is pushed against the sample by a very low specified force in contact AFM. The force is usually in the range of atomic forces (about $10^{-9}N$) resulting in elastic deformation of the surface. A feedback loop is used to maintain a constant force and thus a fixed tip-to-sample spacing. As the probe is scanned over the surface an image of the sample topography is recorded. The cantilever deflection was detected by using the tunneling current on the back side of the cantilever in the original instrument. In later versions of the AFM simpler optical detection techniques were employed to measure the probe deflection.

Aside from topography, other surface properties have also been investigated using these microscopes. A modified version of the AFM uses thermal imaging to detect device failures in microelectronics [Lai 85]. A thermocouple junction was formed by using chromel and alumel to form a V-shaped cantilever. A diamond tip which has a very high thermal conductivity was attached at the probing end. The probe could thus map temperature variation and device failures were located in the form of hot or colds spots resulting from short or open circuits.

Scanning tunneling potentiometry is a modification of the STM which allows simultaneous mapping of topographic and electric potential data on material surfaces [Muralt 87]. The potential distribution under operating conditions and related properties such as the extent of space-charge regions next to p-n and material junctions can be investigated.

The scanning capacitance microscope (SCM) is capable of mapping two-dimensional carrier and dopant density quantitatively in semiconductor devices with nanometer scale spatial resolution [Huang 96]. A conducting tip is brought to the surface of the sample and a high sensitivity capacitance sensor measures the capacitance between the tip and the sample. An AC bias voltage applied to the sample changes the capacitance detected due to

semiconductor depletion. The instrument is operated in a feedback loop so that a constant AC capacitance is maintained. Dopant density profiles are derived from the SCM data using a quasi-one-dimensional analytical model. Another technique that allows dopant profiling in semiconductors is the scanning resistance microscope (SRM) [Shafai 94]. Here a conducting probe is used to perform localized resistance measurements which are used to delineate between regions of different doping types and concentrations.

All the microscopes discussed so far involve operations in contact mode. In certain applications non-contact measurements are desirable. By increasing the tip-surface separation beyond *10-100 nm* only the long range forces such as Van Der Waals, electrostatic and magnetic forces remain. The magnitude of these forces at relatively large separation may be considerably smaller than forces encountered in contact mode and therefore the detection of the force on the probe is usually different. The cantilever is vibrated near its resonant frequency as compared to the quasi-static forces that are encountered in contact force microscopy. The change in the resonant frequency as a result of tip-sample force interaction is measured and this a.c detection method is sensitive to force gradients rather than the interaction forces themselves. The enhanced amplitude of vibration which is proportional to the force can also be detected.

Magnetic force microscopes (MFM) evolved from the AFM and employs a sharp magnetic tip attached to a cantilever probe [Rugar 90]. The tip is placed in close proximity to the sample and interacts with the stray magnetic field emanating from the sample. A schematic of the instrument is presented in Figure 3.2. The cantilever is mounted on a piezoelectric bimorph which is driven close to the resonant frequency of the cantilever. The presence of a force gradient due to the interaction of the tip with the magnetic field alters the resonant frequency of the cantilever. This shift in resonance will change the oscillation amplitude of the probe which is detected by an optical fiber-based interferometer. A feedback loop maintains a constant level of interaction (constant vibration amplitude) by piezoelectrically adjusting the tip-to-sample spacing. The microscope has been used to study the structure of recording track written on disks and other magnetic media.

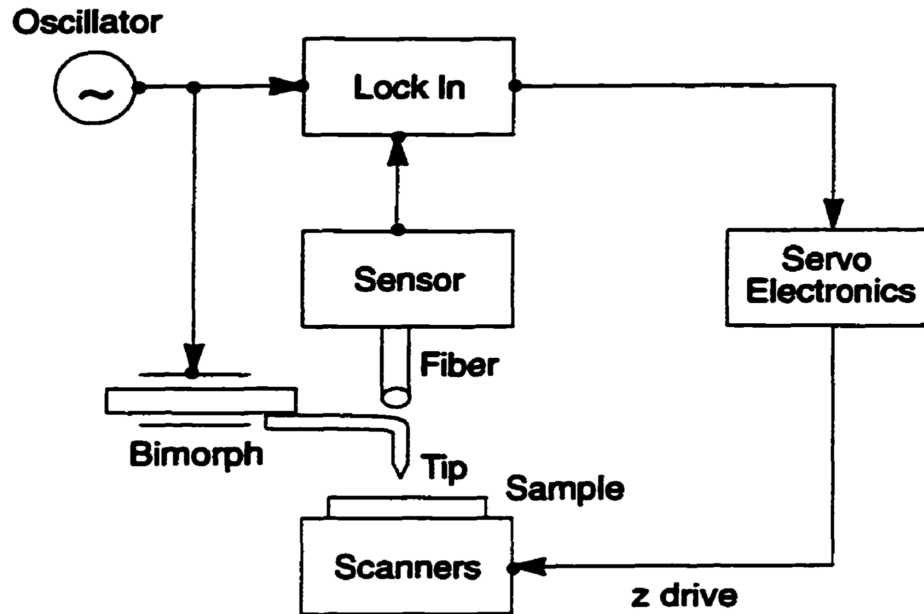

Figure 3.2: Schematic illustration of the magnetic force microscope [Rugar 90].

Magnetic force microscopy has also been applied in the internal current probing of integrated circuits [Campbell 93]. A magnetic probe is scanned over a current carrying conductor and images the magnetic field emanating from the current flow. Current directions and magnitudes have been analyzed with a sensitivity of ~ *1mA dc* and ~ *1μA ac*.

The electrostatic force microscope is a specialized instrument that has been developed for application in the microelectronics field [Wickramasinghe 89]. Localised potential is measured by monitoring the electrostatic force between a conducting probe and the sample. The instrument has been used in the deposition and the imaging of localized surface charges on insulators [Stern 88] and the measurement of contact potential difference between different materials [Nonnenmacher 92]. Ferroelectric domain walls have also been investigated where the microscope is sensitive to the stray electric field emanating from the surface [Saurenbach 90]. When a voltage is applied between the probe and a semiconductor sample, dopant profiling is possible [Huang 92]. The potential difference

mobilizes the conduction electrons or holes resulting in a charged region beneath the probe. The resulting electrostatic force is detected and provides a measure of the dopant concentration. The instrument used in this research is based on the electrostatic force microscope and is presented in more details in the following sections.

3.2 Operating Principle of EFM

The EFM instrument operates by sensing the mechanical deflection of a small non-contacting probe which is caused by the electrostatic force between the tip of the probe and the circuit being measured. As illustrated in Figure 3.3 the sharp tip of a cantilever probe is positioned in close proximity to the test point on the circuit where the local voltage $v_c(x,y,t)$ is to be measured.

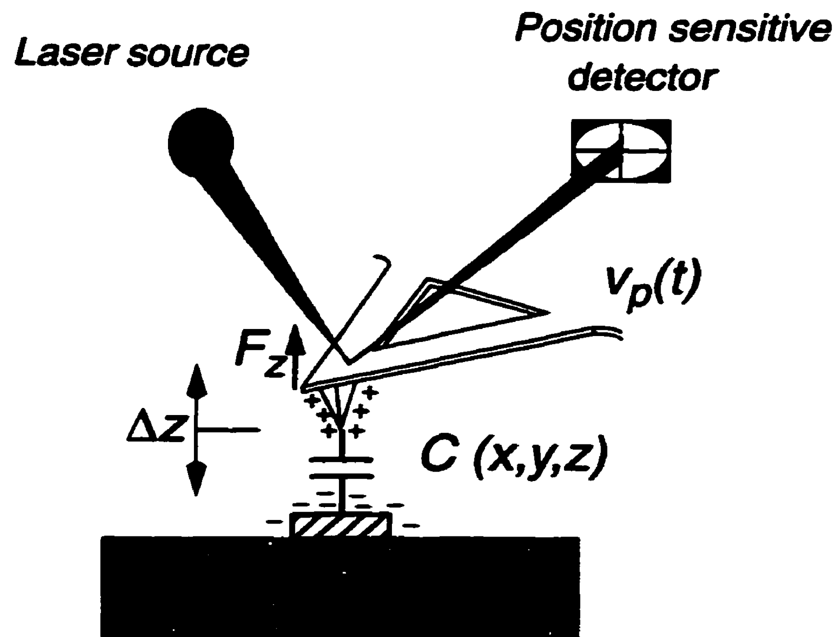

Figure 3.3: Illustration of the Electrostatic Force interaction between conducting probe and a test point.

An adjustable voltage $v_p(t)$ is externally applied to the conducting probe. The probe tip and circuit test point are not in contact and form a small localized capacitor $C(x,y,z)$ which

charges up when there is a potential difference between them. The charge on the capacitor produces an attractive force F_z which then results in a mechanical deflection, Δz, of the probe beam. Thus, by monitoring the deflection using a position sensing detector, the force and subsequently the potential difference between the probe and circuit can be measured. The z-component of the Coulomb force can be derived from the energy in the capacitor ($E = \frac{1}{2}CV^2$) as

$$F_z = \frac{1}{2}\frac{\partial}{\partial z}C(x, y, z)\left(v_p(t) - v_c(x, y, t)\right)^2. \quad [3.1]$$

Here *C(x,y,z)* is the capacitance between the probe and the circuit and is dependent on the probe tip geometry and its position above the circuit surface. An accurate estimate of the capacitance for various probe geometries (including passivated test circuits) can be determined using a static integral equation solution [Bridges 92b]. While the determination of *C(x,y,z)* is necessary for the characterization of the instrument in terms of spatial and temporal resolutions, this capacitance is not required for the voltage measurement schemes used in this research. These measurement techniques are discussed later in the thesis. The force F_z on the probe as defined by equation [3.1] causes a deflection of the beam whose magnitude will depend on the mechanical characteristics of the beam due to geometry and material properties. The probe characteristics and the deflection sensors used are described in more details in the following sections.

3.3 Probe characterization

One of the main components in the EFM instrument is the cantilever probe that senses the electrostatic force between the probe tip and a test point. The deflection of the probe is determined by both the applied force and mechanical properties of the cantilever. The properties of the cantilever, of particular importance, are its spring constant and its resonant frequencies. In this research project cantilever probes made from a thin wire as well as commercially available microfabricated (micromachined) probes were used.

3.3.1 Wire Probe

A photograph of a typical wire probe is shown in Figure 3.4. One end of a thin wire is bent to form a probing tip while the other end is attached to a fixed support. In this manner the probe acts as a cantilever with the tip end being free to vibrate. A sharp tip, with a typical radius of curvature of about *200nm*, is formed by electrochemically etching the wire. A typical probe is fabricated with *127-μm* thick molybdenum wire about *1cm* in length with the last *mm* or so bent to form a probing tip.

Figure 3.4: Photograph of a typical wire probe used in this research. The left (probing) end is free to vibrate while the other end is attached to the center conductor of a coaxial cable.

The spring constant, k, of cantilevers, which for small deflections is defined as the ratio of the applied force to the resulting deflection, represents the rigidity of the probe or its resistance to deflects. This is an important parameter to characterize a probe and small spring constants are usually desirable. The spring constant of a cantilever is given by

$$k = \frac{3EI}{l^3} \qquad [3.2]$$

where E is the modulus of elasticity, I is the moment of inertia and l is the length of the cantilever. For a cantilever with a circular cross-section, as is the case for a wire probe, the moment of inertia $I = \pi d^4/64$ where d is the diameter of the wire. For a typical probe prepared using a *127-μm* diameter Molybdenum wire ($E = 3.2 \times 10^{11}\ N/m^2$) and about *1cm* in length with the last *2mm* bent to form the probing tip the spring constant is estimated to be *22.5N/m*.

The resonant properties of a cantilever in force microscopes is of utmost importance. In microscopes that operate in contact mode the resonant frequency will dictate the speed of the measurement or how fast the surface can be tracked. In microscopes that sense long range forces such as the EFM the resonant frequency is important since the cantilever vibration at off-resonant frequencies is very small and thus very difficult to detect. The natural resonant frequency of a cantilever occurs when the only force acting on the cantilever is its distributed weight. By solving the homogeneous equation of motion of an isolated cantilever, the fundamental resonant frequency is given by [Said 95]

$$\omega_0 = \sqrt{\frac{k}{0.235m + m_{tip}}}. \qquad [3.3]$$

In [3.3] m is the mass of the cantilever beam and m_{tip} is the lumped mass of the tip at the free end. A wire probe similar to the one shown in Figure 3.4 has a resonant frequency on the order of *1KHz*. When the cantilever vibrates under the influence of an external applied force of unit amplitude in a damped medium the frequency response is given by

$$|G(\omega)| = \frac{(\omega_r/\omega)\,(Q/k)}{\sqrt{1 + Q^2\left(\frac{\omega_r}{\omega} - \frac{\omega}{\omega_r}\right)^2}} \qquad [3.4]$$

where ω_r is the resonant frequency under the influence of external and damping forces [Albrecht 91]. Q is the quality factor of the cantilever and is defined as $\omega_r/\Delta\omega$, $\Delta\omega$ being the 3-dB bandwidth of the cantilever's frequency response. Equation [3.3] is valid for high-Q cantilevers when ω_r is approximately equal to ω_0. At resonance the amplitude of vibration is enhanced by the cantilever's Q factor ($|G(\omega_r)| = Q/k$). The frequency response of a typical wire probe was determined experimentally by sweeping the frequency of a sinusoidal driving signal and recording the resulting vibration of the probe by a deflection sensor. The normalized results are shown in Figure 3.5. The resonant frequency of the cantilever is estimated at *1.168kHz*. A normalized theoretical response is calculated and by fitting the theoretical curve to the measured response in Figure 3.5 the quality factor, Q, of the cantilever is deduced to be *272*.

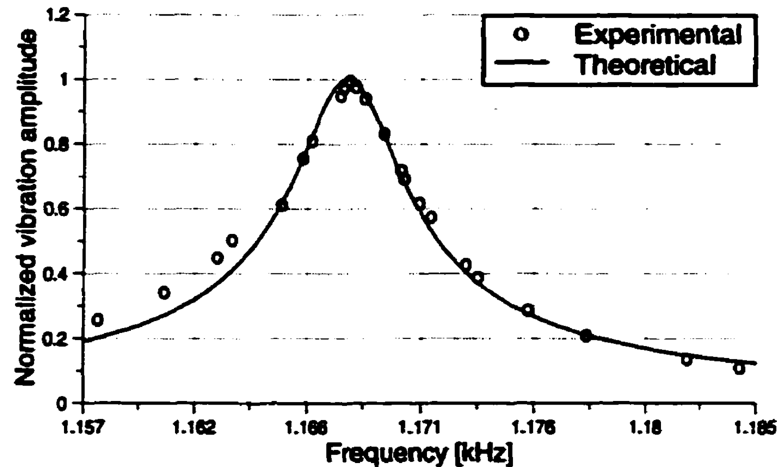

Figure 3.5: Frequency response of a wire cantilever. The theoretical data is calculated for f_r = *1.168 kHz, Q= 272.*

3.3.2 Micromachined Cantilevers

Cantilevers with high resonant frequencies are desirable in order to minimize sensitivity to mechanical vibrations and acoustic noise. Equation [3.3] suggests that the resonant frequency of a cantilever could be increased by raising the spring constant, *k*, or lowering the mass of the cantilever. Cantilevers with high spring constants are not an attractive solution since the same force would now produce smaller deflections which are more difficult to detect. To raise the resonant frequency the mass of the cantilever should be lowered and this is achieved by using microfabrication technologies. Cantilever probes microfabricated from silicon dioxide, silicon nitride (Si_3N_4) and pure silicon using photolithographic techniques are available. For a Si_3N_4 rectangular beam *200μm* long, *30μm* wide and *1μm* thick the spring constant is estimated at *1.125N/m* ($\rho = 3100\ kg/m^3$ and $E = 1.5 \times 10^{11}\ N/m^2$). Using [3.3], the resonant frequency is calculated to be about *500KHz*.

In this research commercially available Si_3N_4 cantilevers were used. The V-shaped cantilever, illustrated in Figure 3.6a, provides increased lateral stiffness as compared to

rectangular beams. Typical dimensions of one cantilever probe use in this research are also indicated in Figure 3.6a. For the geometry of these cantilevers the determination of the spring constant is more involved and numerical techniques based on finite element methods have been used [Neumeister 94]. A typical probe is *0.6µm* thick with a spring constant of *0.064N/m* according to the manufacturer's specifications [PSI]. A pyramidal tip is located at the probing end of the cantilever. The tip height and the width of the pyramid's base are about *4µm* each. A radius of curvature of about *300nm* is possible for the probing tip. The cantilever was coated with a thin gold film to make it conducting and usable in the EFM instrument. The gold coating also provides a reflective surface for the optical deflection detection technique used. SEM micrographs of a commercial Si_3N_4 cantilever with integrated pyramidal tip is shown in Figure 3.6b.

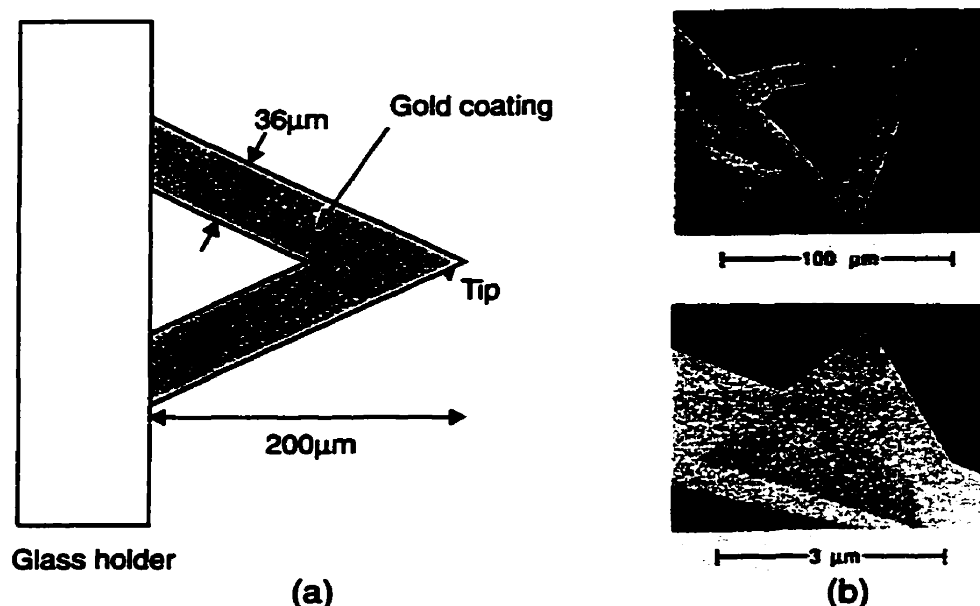

Figure 3.6: (a) Schematic illustration of a micromachined cantilever coated with a gold metal layer; (b) SEM micrographs of a Si_3N_4 cantilever (top) and the pyramidal tip (bottom) [Wiesendanger 94].

The frequency response of a typical micromachined cantilever probe was experimentally investigated. No external driving force was needed since oscillations from thermal excitation are large enough due to the extremely low mass of the cantilever. The resonant frequency of the cantilever was found to be *12.275kHz* and a quality factor of *32* was obtained.

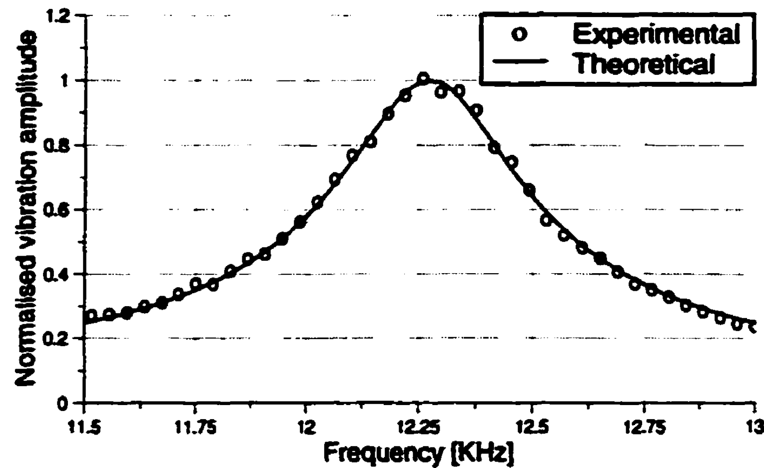

Figure 3.7: Frequency response of a gold coated commercial Si_3N_4 cantilever. The theoretical curve is calculated with f_r = *12.275 kHz* and *Q* = *32*. The experimental data were processed using a 10-pt smoothing routine and every tenth data point is displayed in the graph.

Recently the design of microfabricated probes with integrated waveguides was reported [Bohm 96a]. Metal coated commercial probes were modified to produce coplanar waveguides using a focused ion beam. The goal is to create a *50Ω* transmission line up to the very end of the cantilever probe to improve measurement bandwidth in a *50Ω* system for *mm*-wave applications.

3.4 Deflection Sensors

Accurate detection of the probe's deflection in the EFM instrument is important. The deflection amplitude in a typical experiment is very small and its detection is not an easy task. A sample calculation based on a very simple model of the electrostatic force interaction between the probe and a sample is presented. The probe tip is modeled as a sphere of radius, *r*, over a ground plane representing the sample as shown in Figure 3.8. The probe voltage is v_p which is also the potential difference between the tip and the sample.

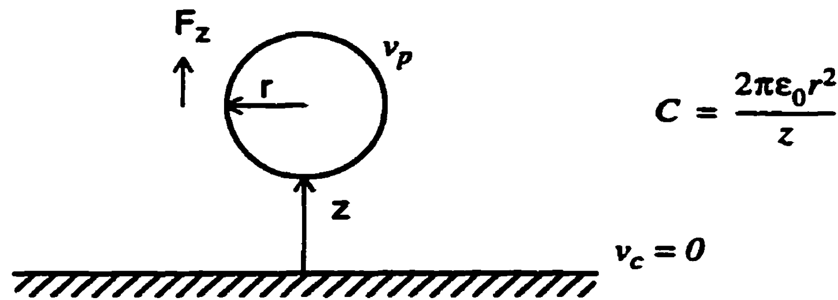

Figure 3.8: Simple model for the capacitance between a probe tip and a sample. The tip is modelled as a sphere.

A parallel plate model is used for the capacitance, C, between the probe and the sample with the effective area of the capacitor plate approximated as $2\pi r^2$ [Sarid 91]. The electrostatic force can then be written as

$$F_z = \frac{1}{2}\frac{d}{dz}C(x, y, z)\,[v_p - v_c]^2 = \frac{-\pi\varepsilon_0 r^2 v_p^2}{z^2}. \qquad [3.5]$$

For a typical wire probe described in Figure 3.4 the radius of curvature r is about $200nm$. If the tip to sample separation is $0.5\mu m$ then the resulting force F is equal to $4.45 \times 10^{-12} N$. Using $22.5N/m$ as the spring constant the static deflection of the probe is estimated at $2 \times 10^{-4} nm$. Modulating the probe voltage at the resonant frequency of the probe results in a larger amplitude of deflection due to the Q-factor (272) of the cantilever. In this case the deflection becomes $0.055nm$.

The first AFM used a scanning tunneling microscope at the end of the cantilever to detect the bending of the lever [Binnig 86]. Since then a number of different techniques have been used to sense the probe deflections in force microscopes. In one scheme the capacitance between a conducting probe and a wire is used to sense any deflection [Neubauer 90]. In this research two different optical methods have been utilised. The first one is based on an optical fiber interferometer while the second one utilises a laser beam-bounce detection system. These methods are discussed next.

3.4.1 Fiber Interferometer Detection Technique

The displacement sensor utilized in this research is similar to a standard interferometer based system except that a Super Luminescent Diode (SLD) is used instead of a laser source. The use of an SLD source overcomes problems associated with optical feedback gain in laser sources [Song 94]. The technique behind the sensor is outlined in Figure 3.9. Light from the source is launched in a fiber and reaches a cleaved fiber end after going through a 2 x 2 directional coupler.

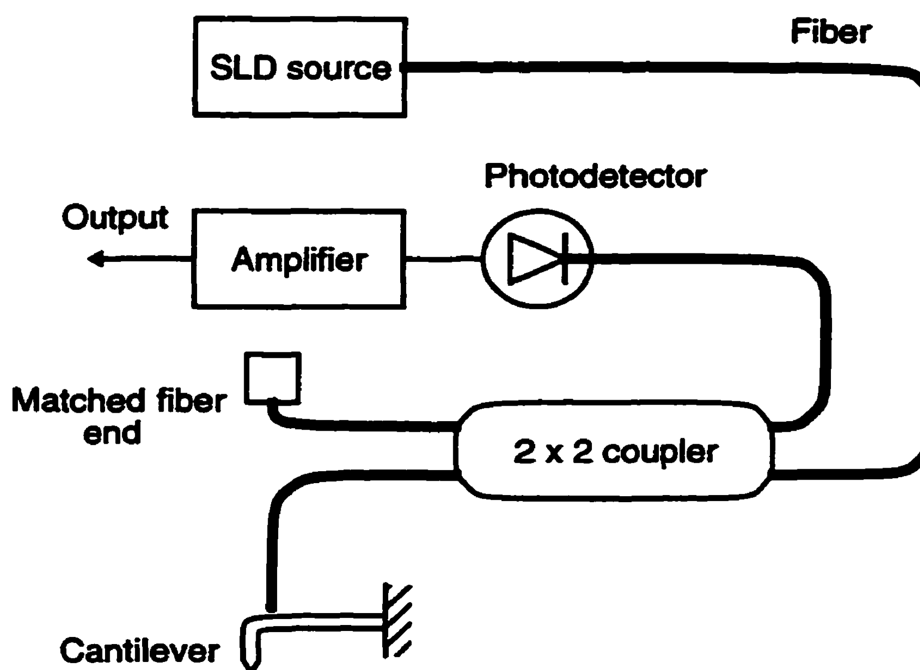

Figure 3.9: Schematic illustration of the fiber interferometer detection technique.

At the fiber-air interface, part of the light is reflected back into the fiber and the rest is transmitted into the cavity between the fiber and the cantilever surface as shown in Figure 3.10. The light then undergoes multiple reflections in the cavity and some of the light is scattered back into the fiber off the cantilever which interferes with the beam initially reflected from air-fiber interface. The total power reflected back into the fiber depends on the phase difference between the two beams and hence on the fiber-cantilever spacing D. The reflected light reaches the directional coupler where half of the power reaches a pho-

todiode detector and the other half goes to the source. The photodiode detector then outputs a signal which is a function of the cantilever deflection.

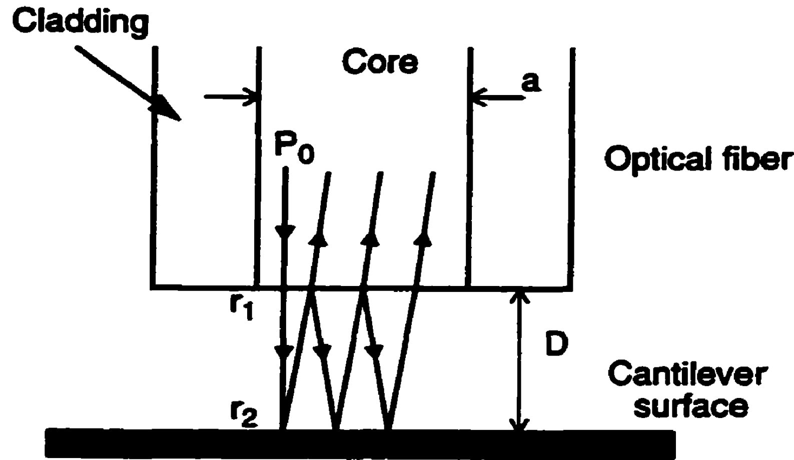

Figure 3.10: Enlarged view of the core region of the fiber over a cantilever's surface showing multiple reflections of the light beam between the fiber-end and the cantilever [Mulhern 91].

The reflected power (P_r) normalised with respect to the incident power P_0 is estimated as [Mulhern 91]

$$\frac{P_r}{P_0} = \frac{(r_1^2 + r_2^2) - 2r_1r_2\cos\left(\frac{4\pi D}{\lambda}\right)}{(1 + r_1^2r_2^2) - 2r_1r_2\cos\left(\frac{4\pi D}{\lambda}\right)} \qquad [3.6]$$

where λ is the wavelength of the light beam, D is the fiber-cantilever separation and r_1 and r_2 are the fiber-air and air-cantilever reflection coefficients respectively. It is interesting to note from equation [3.6] that for a perfect reflector at the cantilever's surface ($r_2 = 1$) the reflected power is constant irrespective of D and therefore no useful signal is derived. Similarly if $r_2 = 0$ the interferometer output is constant and cannot be used to sense any deflections. Thus the air-cantilever reflection coefficient should lie between *0* and *1* for proper operation of the sensor. The normalised reflected power is plotted for several values of r_2 with r_1 set at *0.2* which is typical of an air-glass interface. The wavelength of the light used in our interferometer system is *845nm*.

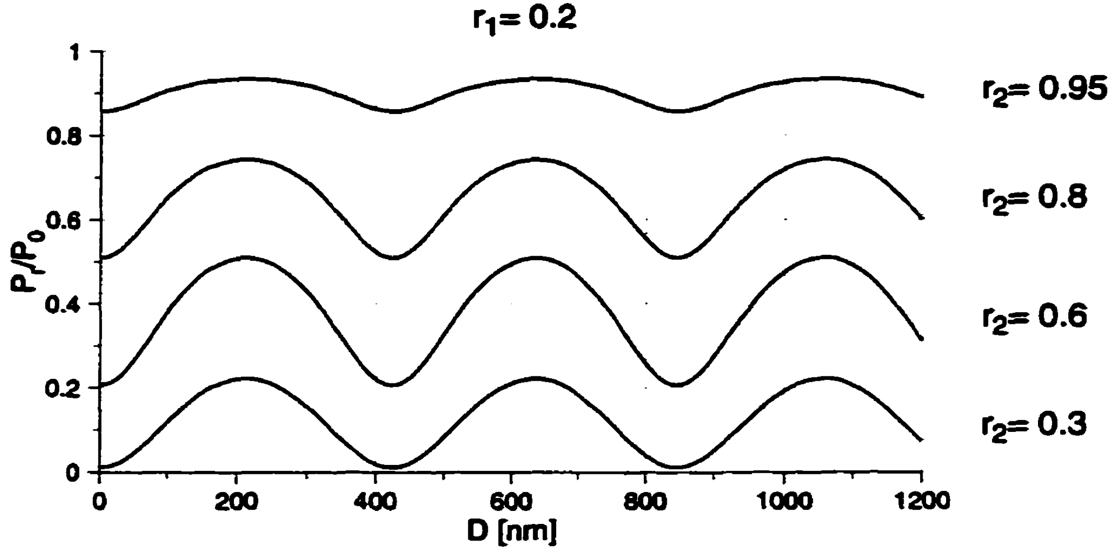

Figure 3.11: Normalized output of the interferometer as a function of the fiber-cantilever spacing D for different values of r_2. An air-glass interface is assumed with $r_1=0.2$ and the wavelength of light $\lambda = 845nm$.

For maximum sensitivity the fiber-cantilever spacing, D, is selected at the point of steepest slope on the normalised power curves. The derivative of the normalized reflected power with respect to the fiber-cantilever spacing D is obtained as

$$\frac{d}{dD}(P_r/P_0) = \frac{2r_1r_2\frac{4\pi}{\lambda}\sin\left(\frac{4\pi D}{\lambda}\right)(1+r_1^2r_2^2-(r_1^2+r_2^2))}{\left[(1+r_1^2r_2^2)-2r_1r_2\cos\left(\frac{4\pi D}{\lambda}\right)\right]^2}. \qquad [3.7]$$

The typical deflection of the cantilever probe is much smaller than the wavelength $\lambda=845nm$ which implies that the slope on the normalised power curve is constant for a given spacing D. The reflected power is thus linearly proportional to the probe deflection.

Equation [3.5] is valid only for small cantilever-fiber separation. In reality the light exiting the fiber diverges resulting in a spreading cone with a half angle typically in the range of 5°-10°. The light spreading results in a progressive reduction in the intensity of the higher order reflections. This effect is modeled by making r_2 a decreasing function of the fiber-cantilever spacing D. Thus the fiber-cantilever separation cannot be made too

large and this is one limitation of the system. The typical spacing is usually less than $10\mu m$.

The performance of the interferometer is primarily limited by two types of noise. The first one is the shot noise which arises from the random arrival of photons at the detector surface. The other noise source is the $1/f$ noise resulting from low frequency fluctuations in the optical output of the light source. Other noise sources such as the $60/50\ Hz$ electromagnetic interference can be minimized by good design. The noise level in the SLD interferometer was measured to be $0.03nm$ in a $0.1\text{-}5000\ Hz$ bandwidth and $10^{-4}\ nm/\sqrt{Hz}$ at frequencies above $400Hz$ [Song 94].

The use of a fiber-optic interferometer using a *GaAlAs* diode laser source has been reported [Rugar 89]. A noise level below 0.1 Angstrom over a $0\text{-}1\ kHz$ bandwidth has been achieved and a flat noise spectrum with a spectral density of $5.5 \times 10^{-5}\ nm/\sqrt{Hz}$ above $1kHz$ was obtained. The interferometer was used in an atomic force microscope for imaging graphite with atomic resolution.

3.4.2 Beam Bounce Detection Technique

The beam bounce detection technique (or optical beam deflection technique) is a reliable and simple detection method [Meyer 88]. It is widely used in research and commercially available SPMs [DI, PSI]. The method is illustrated in Figure 3.12 where a laser beam is reflected off the probing end of the cantilever probe. Since the surface area available for optical reflection is small when microfabricated cantilever probes are used, the laser beam is focused onto the cantilever. The deflection of the cantilever is then detected by a position sensitive detector (usually a split photodetector). In Figure 3.12 the length of the cantilever probe is l and the lever-photodetector spacing is M.

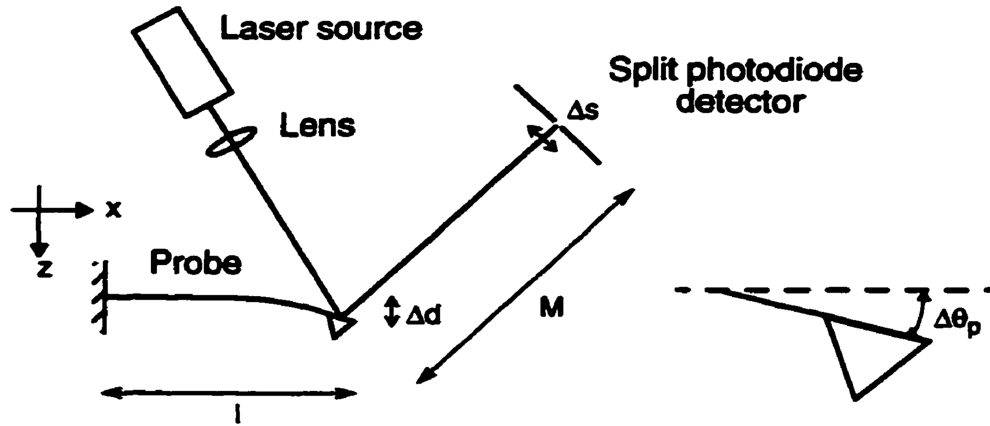

Figure 3.12: Illustration of the beam bounce detection technique. A laser beam is focused onto the probing end of a cantilever probe and then reflected onto a position sensitive detector (a split photodiode detector).

The deflection along the cantilever due to a vertical force (F) applied at a position $x = x_0$ is given by [Dimarogonas 96]

$$z = \frac{F}{6EI}x^2(3x_0 - x)\,. \qquad [3.8]$$

For small deflections the angle at the end of the cantilever is given by

$$\Delta\theta_p \approx \frac{dz}{dx} = \frac{Fl^3}{2EI} \qquad [3.9]$$

where $x_0 = x = l$ (for a force applied on the tip of the cantilever). Using equation [3.2] and $F = kz$,

$$\Delta\theta_p = \frac{3\Delta d}{2l}\,. \qquad [3.10]$$

The deflection of the cantilever produces a linear deflection of the optical beam at the plane of the photodetectors, Δs, given by

$$\Delta s = 3\frac{M}{l}\Delta d \qquad [3.11]$$

assuming $\Delta s << M$. A factor of 2 is introduced since the angular deflection of the reflected beam is twice the angular deflection of the cantilever. The beam deflection results in more

optical power falling on one side of the split detector than the other. This change is detected by taking the difference of the signal from the two photodiodes as shown in Figure 3.13.

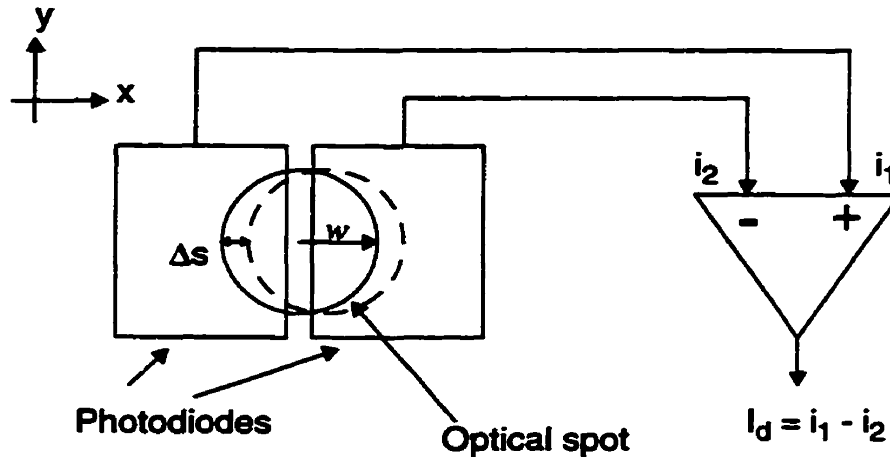

Figure 3.13: Detection of the optical beam as it is deflected. The shift in the optical spot is measured from the difference of the signals from the two photodiode detectors. The parameter, *w*, completely defines the beam power distribution and it is described in [3.12].

In order to find the relation between the cantilever deflection, Δd, and the resulting signal detected (I_d), a few assumptions are made. The optical beam can be assumed to be monochromatic with a gaussian power distribution. This is valid for the laser diode sources often used in these optical deflection systems. The irradiance, I, which is the power incident per unit area, is given in both polar and cartesian forms by [Meyer-Arendt 89]

$$I = I_0 e^{-\left(\frac{2r}{w}\right)^2} = I_0 e^{-\frac{4}{w^2}(x^2+y^2)} \qquad [3.12]$$

In [3.12], w is the distance from the origin at which I drops to $1/e^4$ of I_0. The power of the laser beam falling on the photodetector is found by integrating the irradiance over the incident surface. To find I_d, the photocurrent from each detectors have to be evaluated. A unity conversion efficiency is assumed meaning that the current is equal to the number of photons falling per unit time multiplied by the unit of charge (q). The number of photons per unit time is proportional to the power of the beam. The analysis is further simplified by

assuming a negligible gap between the two photodiodes. Thus, the amount gained by one cell is the same as the one lost by the other. The deflection signal, I_d, is found by integration of the normalized gaussian distribution in [3.12] and is given by

$$I_d = 2Nq\int_0^{\Delta s}\int_{-Y}^{Y}\frac{e^{-\frac{4}{w^2}(x^2+y^2)}}{w^2\pi/4}dxdy. \qquad [3.13]$$

In [3.13], N is the total number of photons in the beam incident on the detectors per unit time and can be found from the total optical power. Since $Y \gg w$ the integration can be simplified as

$$I_d = \frac{4Nq}{w\sqrt{\pi}}\int_0^{\Delta s} e^{-\frac{4}{w^2}x^2}dx. \qquad [3.13a]$$

Changing variables with $t = 2x/w$, equation [3.13a] can be written as

$$I_d = \frac{2Nq}{\sqrt{\pi}}\int_0^{\frac{2\Delta s}{w}} e^{-t^2}dt. \qquad [3.14]$$

The solution of [3.14] has the form of an error function with

$$I_d = Nq\,erf\left(\frac{2\Delta s}{w}\right). \qquad [3.15]$$

Since Δs is often much smaller than w, [3.15] can be further approximated as

$$I_d = Nq\left(\frac{2\Delta s}{w}\right)\frac{2}{\sqrt{\pi}}. \qquad [3.15a]$$

Using [3.11] and substituting for Δs in [3.15a] we obtain

$$I_d = \frac{12NqM}{wl\sqrt{\pi}}\Delta d. \qquad [3.16]$$

Thus the output signal from deflection system is linearly proportional to the cantilever deflection. At first sight the sensitivity of the system can be enhanced by increasing the distance (M) between the cantilever and the detector. However this comes with a degradation in the spot size of the laser beam due to diffraction. The optical deflection system suf-

fers from similar noise sources (shot noise, *1/f* noise) found in the interferometer technique. The sensitivity of both the beam bounce technique and the interferometer technique has been shown to be the same and a minimum detectable displacement of a typical optical beam deflection technique was reported as $7.9 \times 10^{-6}\ nm/\sqrt{Hz}$ [Putman 92].

3.5 Characterization of EFM

In this section the spatial resolution, invasiveness and the sensitivity characteristics of the EFM are discussed. These criteria are used to evaluate the performance of the instrument in terms of its capabilities and limitations.

3.5.1 Spatial Resolution

Spatial resolution is an important quantity that characterizes the performance of the EFM and other force microscopes. It evaluates the representation of the actual distribution of the quantity under investigation by the measurement results. In the EFM the potential on a test structure is measured by sensing the electrostatic force on the probe resulting from the capacitive coupling with the test point. Spatial resolution describes how localised the probe-circuit coupling is. The electrostatic force depends on the tip-circuit geometry and in reality it is a weighted sum of the electrostatic forces induced by different points on the circuit.

The spatial resolution of the instrument can be predicted by the theoretical modeling of the probe-circuit interaction. In the thesis by Raa Said [Said 95], the electrostatic force between a tip geometry and a circuit surface was calculated by evaluating the induced charge on the conductive surface of the probe. A static integral equation approach was used to formulate the problem which was solved using the method of moments. The force interaction was found for a wire probe similar to the one used in this research by carefully modelling the tip geometry. Spatial resolution is also dependent on the circuit geometries

which are difficult to predict in practice. An infinite plane was considered and the force induced on the probe by different points on the surface was evaluated by calculating the force on these points due to the tip. The geometry exhibits radial symmetry and the force density (force per unit area) as a function of the radial distance from the tip axis is shown in Figure 3.14. The calculation was carried out for a tip-sample separation of *0.1μm* and with a potential difference of *1V* between the probe and the circuit.

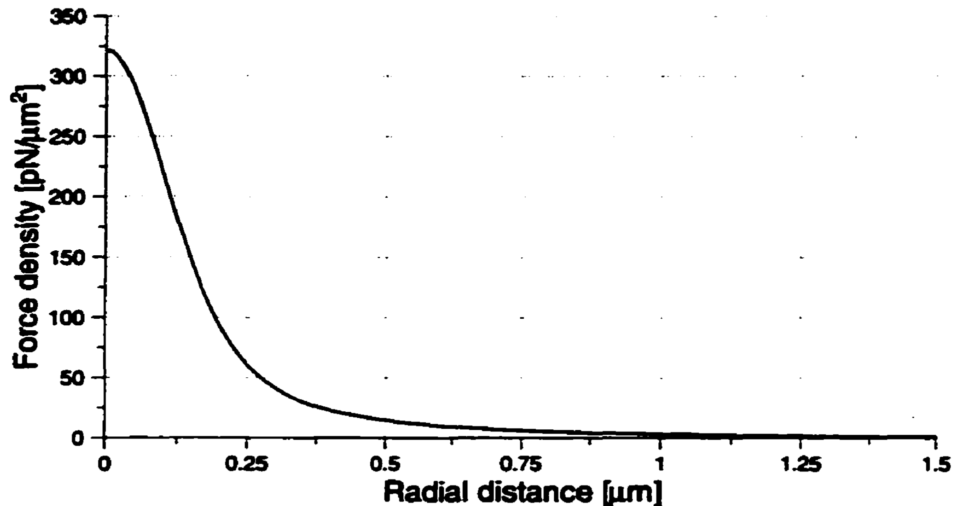

Figure 3.14: Calculated force per unit area induced on a ground plane as a function of the radial distance from the tip axis. The tip is positioned *0.1μm* above the circuit surface [Said 95].

The spatial resolution in this particular case is inferred as the size of the circuit surface that induces a specified fraction of the total electrostatic force found by integrating the area under the force density curve. For a tip-circuit separation of *0.1μm* and a fraction value of *1/2* the spatial resolution was found to be *0.7μm*. For a separation of *1.0μm* the resolution was found to be *15.0μm*. The resolution is thus strongly dependent on the probe-circuit separation. The results presented here are for a uniform potential distribution with dimensions much larger than the probe. A similar approach has been used to evaluate the geometrical resolution in a scanning force microscope [Mueller 94]. The electrostatic force interaction of a micromachined probe over a coplanar waveguide test structure on a GaAs substrate was modeled. The spatial resolution was defined as the diameter of the circle where the force per effective area reduces to *1/e* of its maximum. The resolution was found to be *300nm* for a tip-sample separation of *100nm*.

The resolution was further investigated by scanning the tip of a wire probe over a *3μm* wide interconnect lying *1μm* over a ground plane [Said 95]. The vertical force, F_z, on the tip is plotted as a function of the lateral displacement in Figure 3.15. In these calculations a tip-sample spacing of *1μm* was used together with a probe-circuit potential difference of *1V*. The spatial resolution calculated from the half bandwidth at half maximum is better than *4μm*. The first derivative of the force ($\partial F_z/\partial z$) is also calculated. In the EFM it is the probe deflection which is proportional to the force that is usually detected. By monitoring the force gradient a better spatial resolution is possible as indicated in Figure 3.15.

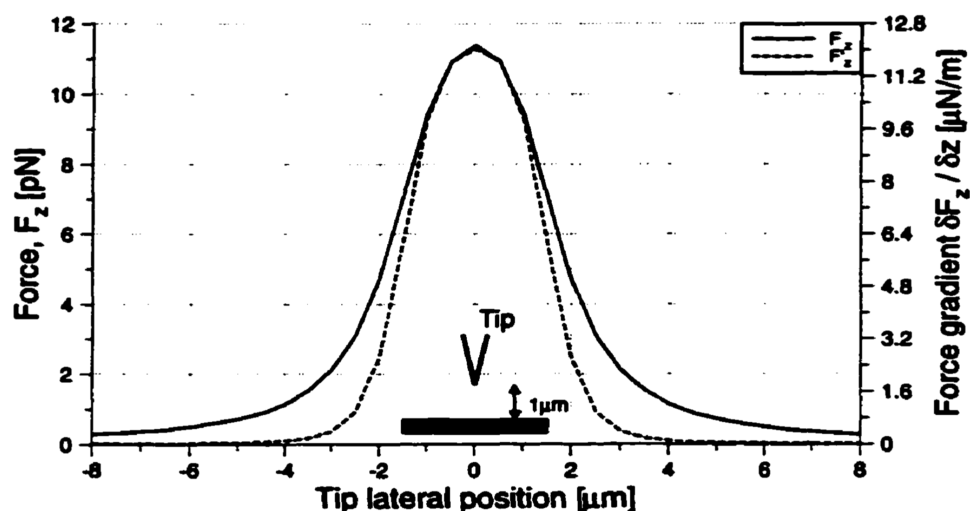

Figure 3.15: The vertical force on the probe tip and its first derivative as the probe is scanned over a *3μm* wide interconnect line with a tip to sample spacing of *1μm* [Said 95].

3.5.2 Invasiveness

The invasiveness of a probing technique is the degree of undesirable disturbance of the circuit's normal operation. When measuring internal nodes of a circuit the parasitic loading from the probing device can alter the signal being sensed. In an ideal world a probe would be noncapacitive, noninductive and would have an infinite resistance so that an exact replica of the signal being probed is obtained. A generalized diagram of the sources of loading introduced by a probe is shown in Figure 3.16.

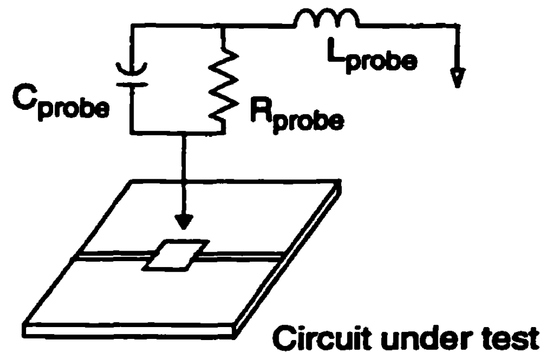

Figure 3.16: Resistive, capacitive and inductive loading effects from a probing device.

Resistive loading is significant if the input resistance is comparable to the circuit impedance. The main effect is to alter voltage levels and it results in amplitude attenuation, shifts in dc offset and changes in circuit bias. A functioning circuit can become non-functional from these adverse conditions. This would be the case when probing the internal node of a circuit in a *50Ω* system with a *50Ω* contact probe mentioned in section 2.1. Inductive loading tends to distort the signal being measured and ringing effects may be introduced. Capacitive loading primarily affects timing measurements. The probe's capacitance acts as a low-pass filter at high frequencies and shunts the high frequency components of a signal to ground thus affecting rise time and propagation delay measurements

In the EFM the probe operates in a non-contact mode and the main source of loading is the capacitive coupling between the conducting probe and the test point. The coupling capacitance between a wire probe and a test structure has been calculated [Said 95]. For a typical wire probe over a *3μm* wide and *600μm* long interconnect placed *1*μm over a ground plane the coupling capacitance is estimated at *250aF* for a tip-sample spacing of *1*μm. The parasitic shunt impedance from such a capacitance is about *7kΩ* at *100GHz* and this would have a negligible effect in applications involving *50Ω* systems often encountered in MMIC's. For timing measurements a test point resistance of *1kΩ* results in a time delay of *0.5ps* using the time constant definition $\tau = 2RC$. For a micromachined probe placed *1*μm over a *3*μm wide interconnect the coupling capacitance is estimated at *230aF* [Bridges 92b].

3.5.3 Sensitivity

The voltage sensitivity of a probing instrument is the minimum voltage that can be detected. Noise in the system ultimately limits the performance of a technique. In the EFM noise is translated into any signal detected by the deflection sensor that is not induced by the electrostatic force between the probe and a test point.

One source of error is the noise in the deflection system itself where the main cause in the optical techniques used in this research is the shot noise at the photodetectors. The noise level in the interferometer sensor was found to be $10^{-4}\ nm/\sqrt{Hz}$ for frequencies above $400Hz$. In the beam bounce detection technique the minimum deflection that can be measured is about $10^{-5}\ nm/\sqrt{Hz}$.

Other possible noise sources are the mechanical vibration of the positioning mechanisms, acoustic noise, electrical noise coupled to the probe from external sources, and the probe vibration due to thermal noise. Mechanical vibration can be minimised by using an air-damped bench and the rigidity of the constructed structure of the EFM instrument results in a resonant frequency much higher than the probe resonance. Noise from electrical coupling can be reduced by proper design and shielding.

The dominant noise source is the thermal vibration of the cantilever probes which are highly resonant and have very little mass. The thermal noise arises from the probe equilibrium with the environment temperature and its spectral content is similar to a white noise. Using the spectral density of thermal noise and taking into account the probe's frequency response, the mean-square deflection of the probe can be written as [Said 95]

$$\langle z_{th}^2 \rangle = \frac{4kk_BT_aB}{2\pi Q\omega_r}\int_0^{\infty}|G(\omega)|^2 d\omega. \qquad [3.17]$$

In [3.17] k_B is the Boltzman constant, T_a is the medium temperature and B is the measure-

ment bandwidth. The root-mean-square deflection at a frequency, ω, is obtained as

$$\langle z_{th}^2(\omega)\rangle = \sqrt{\frac{4Qk_BT_aB}{k\omega_r}} \cdot \frac{\omega_r/\omega}{\sqrt{1+Q^2\left(\frac{\omega_r}{\omega}-\frac{\omega}{\omega_r}\right)^2}} . \qquad [3.18]$$

For a typical wire probe (*Q = 272, k = 22.5N/m,* f_r *= 1.168kHz*) used in this research the RMS deflection induced by thermal noise is about 0.006 nm/$\sqrt{Hz}$. For a micromachined probe (*Q = 32, k = 0.064N/m,* f_r *= 12.275kHz*) the induced deflection is in the order of *0.01 nm/*$\sqrt{Hz}$. These numbers are higher than the noise level encountered in the optical detection systems meaning that the thermal noise of the cantilever probe is the dominating noise source in the instrument.

Using $Z(\omega) = F(\omega)G(\omega)$ the RMS deflection of the probe due to the electrostatic force at a specific frequency is obtained as

$$\langle z_F^2(\omega)\rangle = \langle F_z^2(\omega)\rangle^{1/2} \cdot \frac{(Q/k)\ (\omega_r/\omega)}{\sqrt{1+Q^2\left(\frac{\omega_r}{\omega}-\frac{\omega}{\omega_r}\right)^2}} \qquad [3.19]$$

where $\langle F_z^2(\omega)\rangle$ is the power spectral density of the electrostatic force F_z. From [3.18] and [3.19] a signal-to-noise ratio of *1* gives

$$\langle F_z^2(\omega)\rangle^{1/2} = \sqrt{\frac{4kk_BT_aB}{Q\omega_r}} . \qquad [3.20]$$

To find the voltage sensitivity the term $\langle F_z^2(\omega)\rangle$, using [3.1], can be written as

$$\langle F_z^2(\omega)\rangle^{1/2} = \frac{1}{2}\frac{\partial}{\partial z}C(x,y,z)\Delta V_{rms}(\omega) \qquad [3.21]$$

where $\Delta V_{rms}(\omega)$ is the RMS potential difference at the harmonic component ω.

The minimum RMS potential that can be detected is thus given by

$$\Delta V_{rms} = \frac{2}{\partial C(x,y,z)/\partial z}\sqrt{\frac{4kk_B T_a B}{Q\omega_r}}. \quad [3.22]$$

To determine the voltage sensitivity the term $\partial C(x,y,z)/\partial z$ is needed. For a wire probe ($Q = 272$, $k = 22.5N/m$, $f_r = 1.168kHz$) positioned over a $3\mu m$ wide interconnect, as discussed in section 3.5.1, $(\partial C(x,y,z)/\partial z)/2$ is equal to $11.4pF/m$ (from the force curve in Figure 3.15 where V_p-$V_c = 1V$). The voltage sensitivity is estimated as $50\ mV/\sqrt{Hz}$.

For a micromachined probe ($Q = 32$, $k = 0.064N/m$, $f_r = 12.275kHz$) similar to the one used in this research the capacitance derivative of the probe positioned over $1\mu m$ over a circuit surface is estimated at $50pF/m$ [Bridges 92b]. This results in a minimum detectable voltage of about $1\ mV/\sqrt{Hz}$.

3.6 Voltage Measurement Schemes

The circuit signal to be probed by the EFM instrument could be a DC voltage, a low frequency signal or a high frequency signal. In this section a DC measurement scheme for absolute voltage measurement using a nulling technique is presented. A heterodyne technique for the measurements of high frequency sinusoidal signals is also discussed. Measurement of periodic arbitrary waveforms using a pulse sampling technique is introduced in chapter 5.

3.6.1 DC Measurement

In DC measurement the circuit voltage can be represented as $v_c(x,y)$. The electrostatic force using [3.1] can be written as

$$F_z = \frac{1}{2}\frac{\partial}{\partial z}C(x,y,z)\left(v_p(t) - v_c(x,y) + \Delta\phi\right)^2. \quad [3.23]$$

In [3.23] the term $\Delta\phi$ is introduced to account for DC offsets effect due to contact potential differences and surface charging [Domansky 93]. The direct measurement of the force in order to induce the circuit voltage would require the knowledge of the coupling capacitance between the probe and the test circuit and therefore accurate probe positioning mechanism. A technique relying on a null-force rather that absolute force measurement is utilized [Weaver 91, Said 94a]. This nulling technique is implemented by driving the probe with a signal described by

$$v_p(t) = A + K\cos(\omega_p t) \qquad [3.24]$$

where A is a DC bias, K some adjustable parameter and ω_p usually chosen to be close to the probe resonant frequency ω_r. By expanding [3.23] the force can be rewritten as

$$\begin{aligned} F_z &= \frac{1}{2}\frac{\partial}{\partial z}C(x,y,z)\left(A + K\cos(\omega_p t) - v_c(x,y) + \Delta\phi\right)^2 \\ &= \frac{1}{2}\frac{\partial}{\partial z}C(x,y,z)\left\{\left[(A - v_c(x,y) + \Delta\phi)^2 + \frac{K^2}{2}\right]\right. \\ &\quad \left. + 2\,[A - v_c(x,y) + \Delta\phi]\,K\cos(\omega_p t) + \frac{K^2}{2}\cos(2\omega_p t)\right\} \end{aligned} \qquad [3.25]$$

Examination of [3.25] suggest that the force has a DC component which results in a static deflection of the probe as well as components at ω_p and $2\omega_p$. The force at ω_p is given by

$$F_z\big|_{wp} = \frac{\partial}{\partial z}C(x,y,z)\,[A - v_c(x,y) + \Delta\phi]\,K\cos(\omega_p t) \qquad [3.26]$$

The deflection of the probe is a function of both the probe mechanical properties and the frequency of the driving force. As mentioned earlier the deflection amplitude is enhanced by the cantilever's Q factor when the probe is driven close to its resonant frequency (ω_r). Thus the signal-to-noise performance of the instrument is improved by choosing ω_p close to ω_r and the probe deflection at ω_r is given by

$$\Delta z\big|_{\omega_p = \omega_r} \approx \frac{QF}{k} = \frac{\partial}{\partial z}C(x,y,z)\,\frac{Q}{k}\,[A - v_c(x,y) + \Delta\phi]\,K\cos(\omega_r t)\,. \qquad [3.27]$$

A block diagram showing the implementation of this measurement system is given in

Figure 3.17 where the probe is positioned in close proximity to the test point on a circuit. The circuit displacement can be controlled in all three axes. The probe deflection at ω_r is monitored by a sensor and a lock-in amplifier which is referenced to the probe signal frequency. The output of the lock-in amplifier is fed back to the probe after an integrator stage. The probe signal parameter A is thus adjusted until the deflection is nulled at which point $A \approx v_c$.

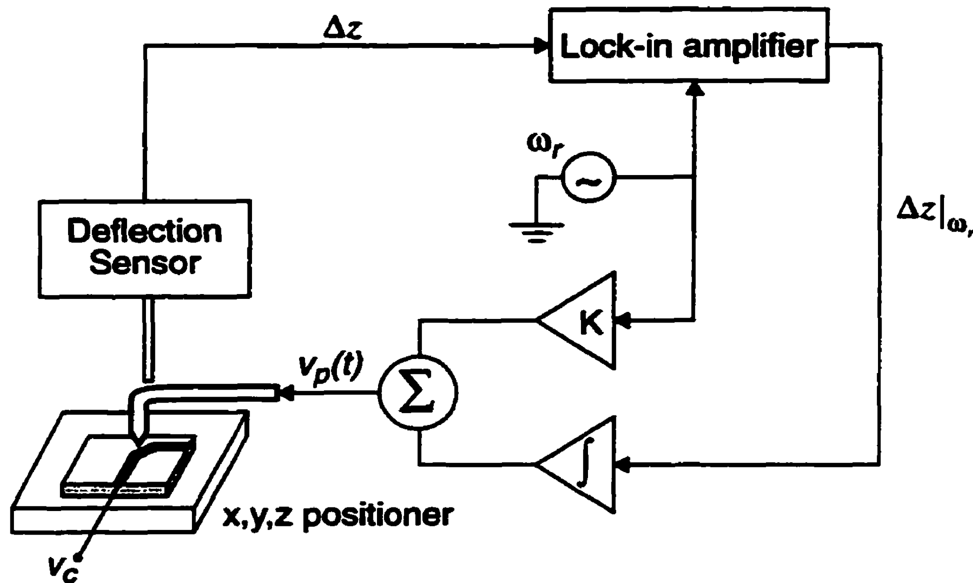

Figure 3.17: Implementation of the nulling technique for the measurement of a local DC potential.

3.6.2 Measurement of High Frequency Sinusoidal Signals

In the electrostatic force approach the probe frequency response is critical for measurements of high frequency signals. The probe deflection becomes very small for frequencies much higher than the resonant frequency of the cantilever probe. The electrostatic force has a square law dependence on the potential difference as indicated in [3.1]. Using the non-linear force-voltage relationship a mixing technique can be employed to down-convert a high frequency signal to a lower frequency at which the probe can deflect. A heterodyne technique is therefore employed for the probing such signals.

Signal mixing has been used in the measurement of high frequency signals using the scanning force microscope based on the electrostatic force interaction. There have been two approaches to using the signal mixing concept. The first uses a frequency modulation technique [Hou 92, Ho 93, Bloom 94, Bohm 94a, Bohm 94b, Nechay 95, Leyk 95, Bohm 96b]. Here a high frequency circuit signal was measured by using a probe signal with a slightly different frequency. When both the circuit and probe signals are referenced to a common ground, the non-linear force interaction results in sum and difference force terms. The difference frequency, or intermediate frequency (IF), and its relevant harmonics are chosen to be below the probe resonance. In this way the probe can respond to the resulting force terms. Using this method both high frequency periodic digital and sinusoidal signals were measured.

The second mixing approach uses an amplitude modulation technique [Bridges 93, Said 94b, Bridges 95]. Here the high frequency probe signal is modulated by a lower frequency (IF) signal. The square law force non-linearity results in a force term at the intermediate frequency. If the intermediate frequency is at or below the resonant frequency of the probe, high frequency periodic digital and sinusoidal signals can be measured.

In this research a heterodyne technique based on amplitude modulation at the probe resonant frequency is used for probing high frequency signals. In this chapter the heterodyne technique for measuring sinusoidal signals is formulated. Chapter 5 will deal with arbitrary waveforms. Both the magnitude and the phase of the circuit signal are important when dealing with sinusoidal signals. In the measurement scheme used in this research a nulling technique is utilized to determine both the magnitude and the relative phase of the test point signal thus enabling a vector voltage measurement. Assuming that the circuit under test is driven at specified frequency ω_0, the signal at the test point can be described by

$$v_c(x, y, t) = V_c \sin(\omega_0 t + \phi_c) . \qquad [3.28]$$

In implementing the amplitude modulation the use of a sinusoidal or square wave modulating signal is possible. Both schemes are discussed next.

3.6.2.1 Sinusoidal modulation

The voltage applied to the probe in this modulation scheme is described as

$$v_p(t) = (A + K\cos(\omega_r t))\sin(\omega_0 t + \phi_p) \quad [3.29]$$

where A, K and ϕ_p are user-controlled parameters. The method is illustrated by the schematic shown in Figure 3.18 where the circuit voltage $V_c\angle\phi_c$ is being probed. A high frequency source drives the circuit at ω_0 and a high frequency probe signal is also derived from the same source. A phase shifter in the circuit path to the probe allows the variation of ϕ_p with respect to ϕ_c. The signal is then modulated at the resonant frequency (ω_r) of the of the probe as shown in Figure 3.18.

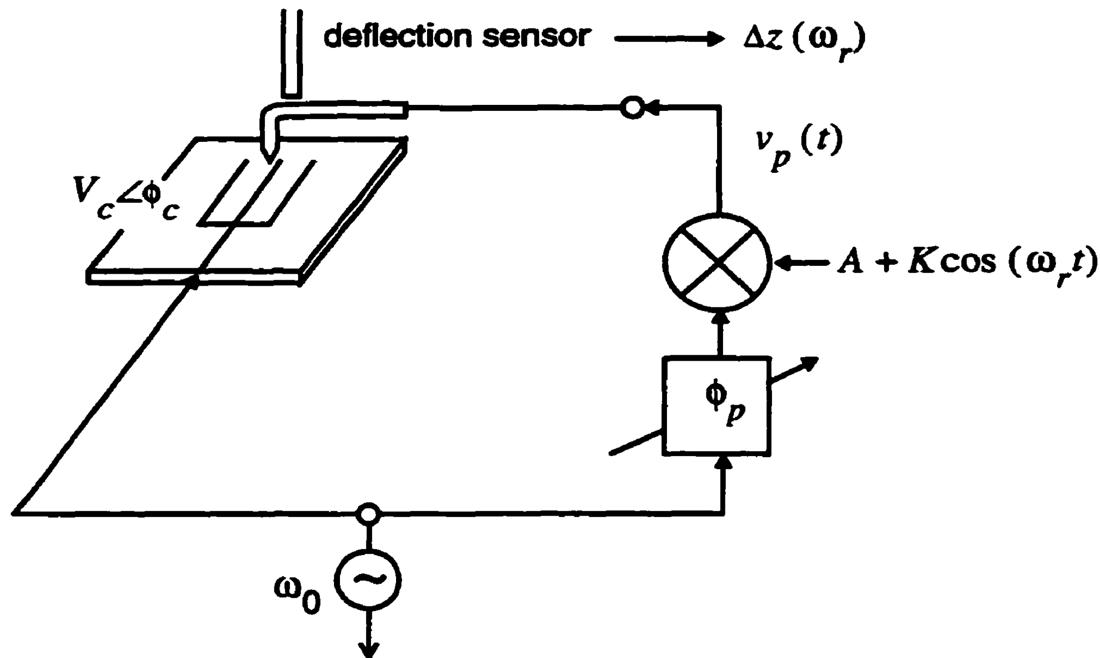

Figure 3.18: Schematic illustration of the heterodyne vector voltage measurement using a sinusoidal modulation scheme.

Using [3.23] the resulting force on the probe is given by

$$F_z = \frac{1}{2}\frac{\partial}{\partial z}C(x, y, z) \cdot \left([A + K\cos(\omega_r t)]\sin(\omega_0 t + \phi_p) - V_c\sin(\omega_0 t + \phi_c) + \Delta\phi\right)^2 \quad [3.30]$$

The square law in [3.30] produces a static force component as well as components at ω_r, $2\omega_r$, ω_0, $2\omega_0$, $\omega_0 \pm \omega_r$, $2\omega_0 \pm \omega_r$, and $2\omega_0 \pm 2\omega_r$. The force component at the resonant frequency w_r results in an enhanced deflection of the probe. Thus, only that component is detected using a lock-in amplifier and it is given by

$$\Delta z|_{w_r} = \frac{1}{2}\frac{\partial C}{\partial z} \cdot \frac{Q}{k} \cdot K[A - V_c \cos(\phi_p - \phi_c)] \cos(\omega_r t) . \qquad [3.31]$$

By adjusting the parameters A and ϕ_p until the deflection at ω_r is nulled both the circuit signal amplitude (V_c) and phase (ϕ_c) can be extracted. The ill-conditioned factors $C(x,y,z)$, Q and k are not required by using the nulling method. The term $\Delta\phi$ is absent in [3.31] and therefore the measurements do not suffer from DC offset effects. In [3.31] the determination of V_c and ϕ_c by using a nulling technique involves a dual optimization of the parameters A and ϕ_p. The unknown amplitude V_c is equal to A with the deflection nulled when $\phi_p = \phi_c$. This assumes prior knowledge of the phase and the accurate determination of phase requires the unknown voltage V_c. An algorithm has been developed that enables the determination of the phase initially and then the amplitude. The scheme is illustrated in Figure 3.19 where the relative amplitude of deflection of the probe at ω_r is plotted against the probe-circuit phase difference (ϕ_p - ϕ_c).

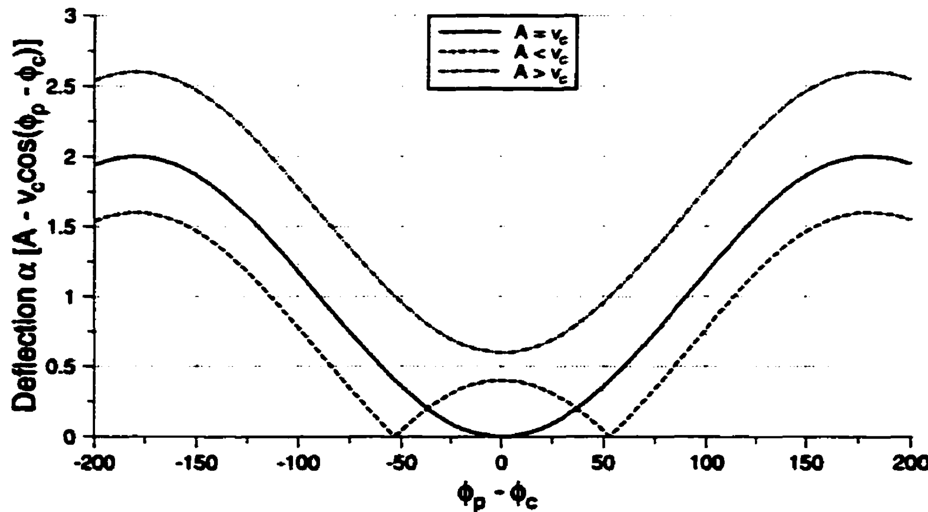

Figure 3.19: Relative probe deflection as a function of probe-circuit phase difference for the cases when $A=V_c$, $A < V_c$ and $A > V_c$.

When the probe parameter A is greater than the circuit voltage V_c the deflection is never nulled. With $A = V_c$ the circuit is only nulled at $\phi_p = \phi_c$ while with $A < V_c$ the deflection is nulled at two distinct places. The mean value of these two points, when they are less than 180° apart, is equivalent to $\phi_p - \phi_c = 0^o$. In practice A is easily chosen to be less than V_c and the phase ϕ_p varied to find the two null points. Once the phase has been determined the probe parameter A is adjusted until the deflection is nulled and the circuit signal amplitude is extracted as $V_c = A$.

3.6.2.2 Square wave modulation

In this scheme the heterodyne technique is similar to the case of sinusoidal modulation except that the probe signal is modulated by a square wave of the form $[A + KG_s(t)]$ where the fundamental harmonic of $G_s(t)$ is at the probe resonance ω_r. The motivation behind this technique is that the implementation of sinusoidal modulation can prove to be more difficult using simple electronics especially at high frequencies. The probe signal can be written as

$$v_p(t) = [A + KG_s(t)] \sin(\omega_0 t + \phi_p) \qquad [3.32]$$

where A, K and ϕ_p are adjustable parameters. The term $G_s(t)$ can be represented by its fourier series as

$$G_s(t) = \frac{4}{\pi}\sum_{n=1}^{\infty} \frac{1}{2n-1} \cos((2n-1)\omega_r t) . \qquad [3.33]$$

Using the force equation [3.23] the square law mixing results in a static force and components at $(2n-1)w_r$, ω_0, $2w_0$, and $\omega_0 \pm (2n-1)w_r$. The deflection at the probe resonance becomes

$$\Delta Z|_{w_r} = \frac{1}{2}\frac{\partial C}{\partial z} \cdot \frac{Q}{k} \cdot K \cdot \frac{4}{\pi}[A - V_c \cos(\phi_p - \phi_c)] \cos(\omega_r t) . \qquad [3.34]$$

This result is similar to the one obtained in [3.31] except for the factor $4/\pi$. A proce-

dure similar to previous case is utilized for the determination of (V_c,ϕ_c). Thus any modulation signal with a fundamental harmonic of ω_r can be utilised. The choice is however dictated by the simplicity in its implementation.

Chapter 4

Vector Voltage Measurement

In this chapter the application of the heterodyne technique to the vector voltage measurement of high frequency signals using the EFM instrument is demonstrated. The constructed probing instrument is described and difficulties encountered in measurement at radio frequencies (*GHz*) are discussed. Different implementations of the square wave modulation scheme (introduced in the previous chapter) are presented together with the measurement results.

4.1 Introduction

Rapid advances in the microelectronics field have made it possible for devices to become denser, faster and more complicated. The push towards high frequencies in the IC technology have resulted in gigahertz operating frequencies. Microwave Monolithic Integrated Circuits (MMIC's) components operating in the *GHz* range are routinely used in personal communication systems, cellular phones and other RF technologies. In the development of such devices accurate signal measurements at internal points are often required for design and performance verifications. The probing instrument presented in this research has the capability of becoming an important diagnostic tool.

Vector voltage measurement refers to the case where both the phase and amplitude of a circuit signal is extracted. The device under test is externally driven at a specified frequency and only the relative phase and magnitude of the circuit signal change as it propagates along the device. Thus measurement is made at a fixed frequency and possible

applications exist in analog and linear circuit testing. The use of the EFM instrument for probing signals in the *GHz* range introduces two important problems. Firstly, the accurate determination of the probe signal at the tip of the cantilever probe is difficult due to the discontinuity at the probing end. The signal applied to the probe and the signal at the probe tip is not necessarily the same since a small cable length along with discontinuities at the probe end can introduced a large phase change and result in signal mismatch. This effect is further discussed in section 4.3.

The second difficulty is the generation of the modulated probe waveform at high frequencies. The simpler square wave modulation scheme is usually chosen instead of the sinusoidal modulation scheme. Although commercial instruments are available to generate the square wave modulated signals the cost of these microwave instruments can be quite expensive. Vector voltage measurement of high frequency signals (up to *1GHz*) has been demonstrated using the square wave modulation scheme [Mittal 94]. One of the objectives of this thesis is to investigate different implementations of the square wave modulation scheme using simple and inexpensive electronics. The motivation was to simplify the measurement system, possibly with some automation, and also to extend the frequency range of the measurements. Three different methods are presented together with the results from measurements performed on a microstrip interconnect line as well as the internal nodes of a commercial MMIC and a MHMIC (Microwave Hybrid Monolithic Integrated Circuit).

4.2 The EFM Probing Instrument

A photograph of the EFM probing instrument that was constructed is shown in Figure 4.1(a). In this instrument an optical beam bounce detection technique is used to sense the deflection of a micromachined cantilever probe. A rigid aluminum structure holds the circuit positioner and the laser beam positioning and alignment mechanism. The aluminum structure eliminates the noise from low frequency vibrations. The photodiode detectors are also attached to the same aluminum structure.

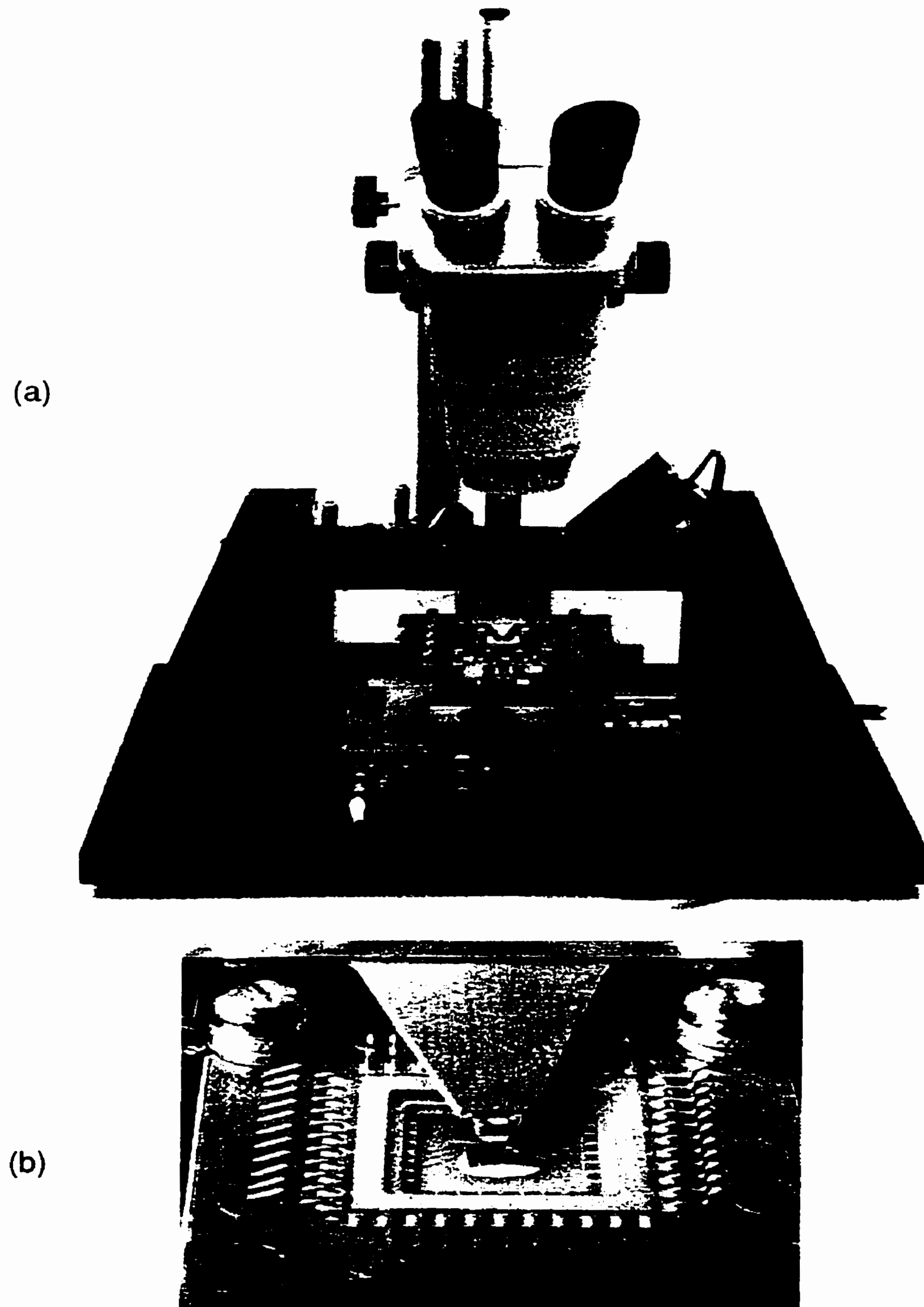

Figure 4.1: (a) Photograph of the EFM probing instrument; (b) close-up view of a micromachined probe positioned over a test circuit.

The circuit under test is usually mounted in a high speed test fixture which is placed on a three-axis positioner for moving the probe to the desired internal test point and for adjusting the tip-to-sample separation. Figure 4.1(b) shows a close-up view of a micromachined probe positioned over a test circuit. The cantilever probe is attached to one end of a coplanar waveguide which is then connected to the probe-signal generating circuit through an SMA connector and coaxial cables.

4.3 High Frequency Probe Effects

The determination of the probe signal is important in the implementation of the nulling technique for absolute voltage measurement. As mentioned in the previous section the probe signal reaches the micromachined cantilever tip after a transition from a coaxial cable to a coplanar waveguide. The coplanar transmission line was fabricated from a copper coated dielectric by rubbing the unwanted regions using a milling machine [T-Tech] and was designed for a characteristic impedance of *50Ω*. In the case of the molybdenum wire probe, the cantilever was simply attached to the center conductor of a semi-rigid coaxial cable. A feedthrough termination with a *50Ω* transmission line of adjustable length was used to match the discontinuous probe to the signal generating electronics.

A circuit model for the probe arrangement and its interaction with the test circuit is shown in Figure 4.2. The coplanar waveguide as well as the semi-rigid coaxial cable are modeled as a transmission line. A 50Ω system, which is often the case in practice, is used.

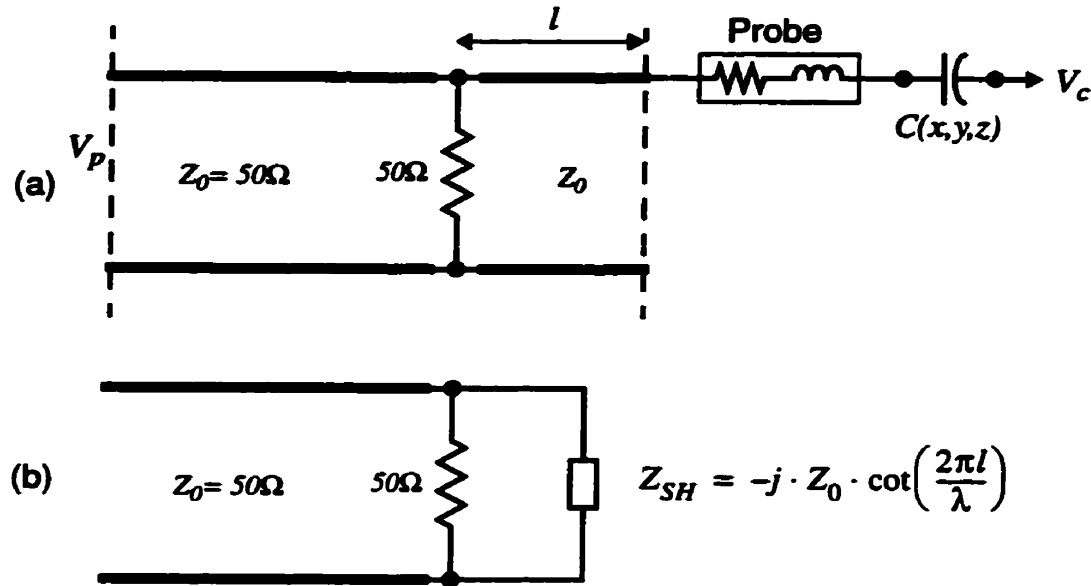

Figure 4.2: (a) Circuit model for probe-circuit arrangement, (b) resulting circuit assuming the coupling capacitance *C(x,y,z)* as an open circuit.

The probe and its capacitive coupling with the test circuit are represented by a lumped *RLC* model. The coupling capacitance, *C(x,y,z)*, is usually very small, on the order of *300aF*, as mentioned in chapter 3. The equivalent impedance at *10GHz* is still on the order of *50kΩ* and an open-circuit at the probing end is a reasonable assumption. The probe is thus modeled by an open-circuited *50Ω* line of length *l*. Using transmission line theory, the equivalent shunt impedance of the open line is calculated as

$$Z_{SH} = -j \cdot Z_0 \cdot \cot\left(\frac{2\pi l}{\lambda}\right) \qquad [4.1]$$

where λ is the wavelength associated with the signal frequency. The length of the line is thus critical to obtain a good match characterized by a low return loss. The equivalent load Z_L, in Figure 4.2(b), becomes $50Z_{SH}/(50+Z_{SH})$. The voltage reflection coefficient of the load impedance is given by

$$\Gamma = \frac{Z_L - Z_0}{Z_L + Z_0} = \frac{-1}{1 - 2j\cot(2\pi l/\lambda)}. \qquad [4.2]$$

The return loss S_{11} is thus obtained as

$$S_{11} = 20\log|\Gamma| = -20\log\sqrt{1 + 4\cot^2\frac{2\pi l}{\lambda}}. \qquad [4.3]$$

The return loss was calculated as a function of the normalized length (l/λ) and is plotted in Figure 4.3. From the result obtained, a good wide-band match could be achieved by terminating with the 50Ω impedance near the end of the probe so that $l \sim 0$. The problem with this arrangement is the heat produced by the load due to the probe voltage. The heating is sufficient to disturb the cantilever probe and results in a continuous mechanical drift of the probe. The probe deflection cannot be properly nulled in this case. An alternative method was employed where a feedthrough termination was used far from the probe. The feedthrough termination was fabricated by soldering a 50Ω chip resistor across the signal and ground lines of a coplanar transmission line. A coaxial cable was then used to carry the signal to the probe. The return loss of this system was measured on a network analyser and is shown in Figure 4.4.

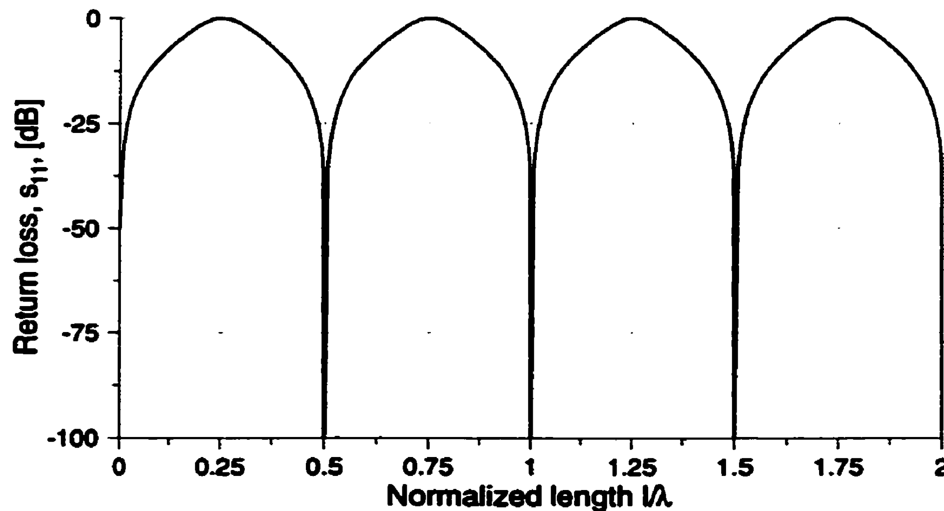

Figure 4.3: Simulated return loss, S_{11}, as a function of the normalized open-circuit length l/λ.

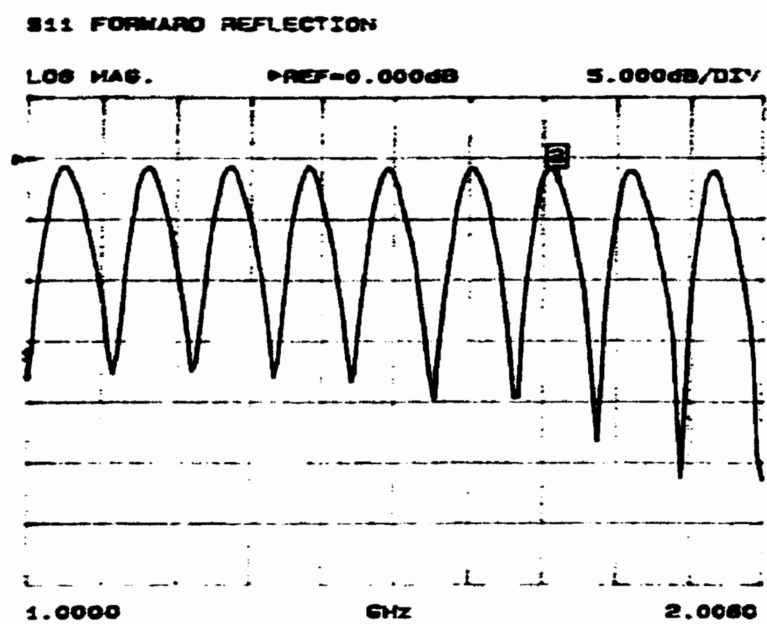

Figure 4.4: Return loss, S_{11}, measured on a network analyzer as a function of frequency for a fixed line length.

A narrow-band match is attained at the operating frequency of interest. This is not major concern since the modulating frequency (the probe resonance) is quite low - less than *15kHz* for the cantilevers used in this research. Thus, the signal applied to the probe is narrow-band at *GHz* frequencies and a good match at the carrier frequency also provides a match for the modulated signal. The main limitation of this matching technique is that measurement can be made only at one frequency at a time. The use of an electronic wide-band phase shifter would enable automatic matching of the probe. Measurements can then be performed at different frequencies similar to a network analyzer.

In the experimental set-up a manual phase shifter was inserted between the feedthrough termination and the probe so that the effective length of the open circuit line can be adjusted for a low return loss at the desired frequency. A directional coupler was used for this purpose as shown in Figure 4.5. The reflected power from the feedthrough termination at the desired RF frequency (f_0) was measured by a power meter using a directional coupler. The effective length between the feedthrough and the probe was adjusted

using the phase shifter until the reflected power was minimized. The resulting matched circuit is only valid at f_0.

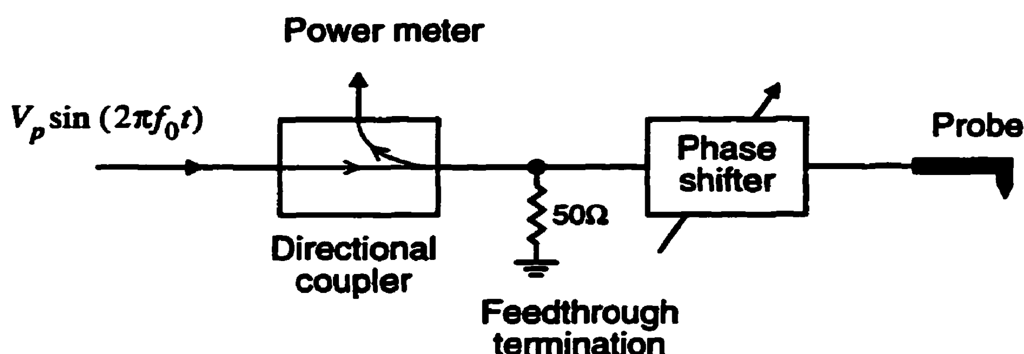

Figure 4.5: Probe matching at a frequency f_0 by adjusting the effective length of open circuit line and using a directional coupler to measure the reflected power.

The use of the heterodyne technique for vector voltage measurement using different implementations of the square-wave modulation technique is presented in the following sections.

4.4 Double-Path Modulation

The principle behind this modulation scheme is illustrated in Figure 4.6. The high frequency input signal ($\cos(\omega t)$) is fed to a 2 way-0° power divider. One of the divided outputs from the splitter goes through a biphase modulator that introduces a *0°* or *180°* fixed phase shift depending on the control signal. The high frequency signal is thus modulated by changing the control signal at the probe resonance f_r and can be written as $KG(t)\cos(\omega t + \theta)$ where θ accounts for the phase shift along that path. This modulates the RF carrier by a symmetrical square wave. The typical insertion loss for the modulator is about *4dB*.

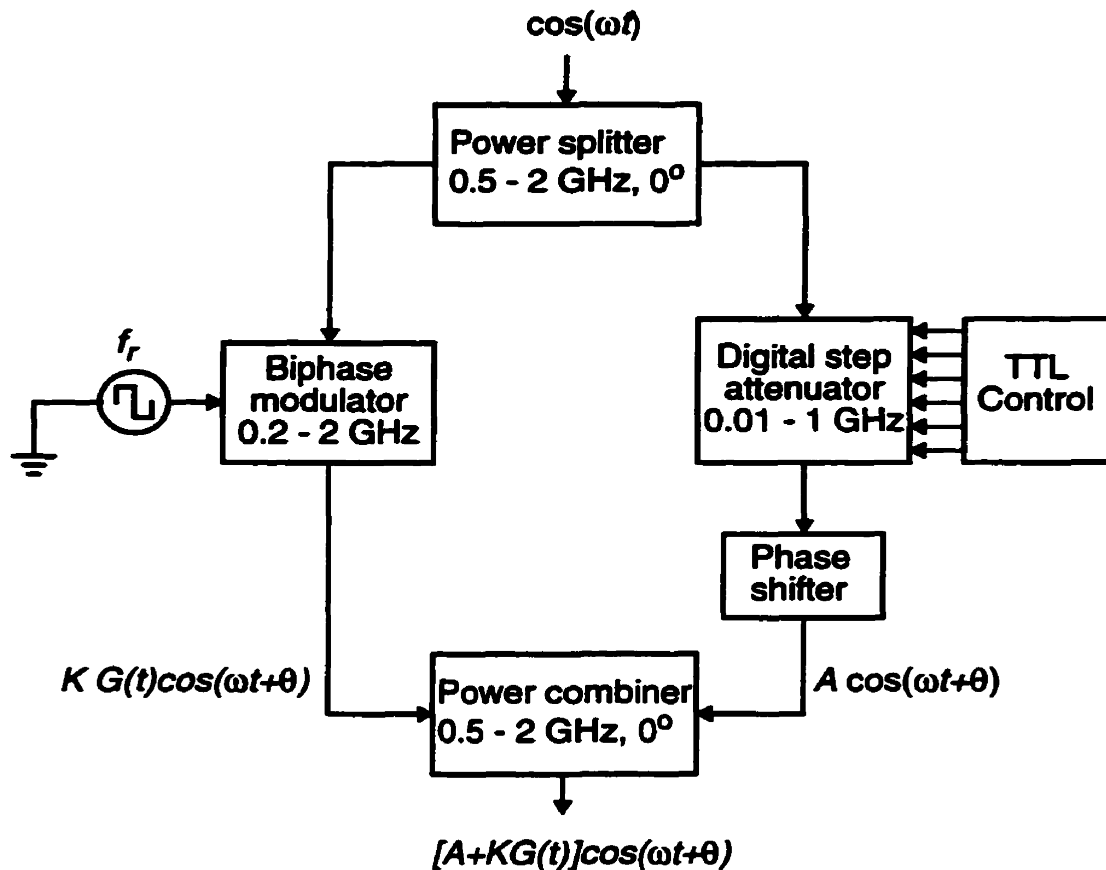

Figure 4.6: Schematic illustration of the double-path square wave modulation scheme.

The other half of the divided high frequency input is fed to a digital step attenuator (DSA) where the amplitude of the high frequency signal can be varied. The attenuation introduced by the DSA is controlled by six TTL inputs and can be varied between *0 - 31.5 dB* in steps of *0.5dB*. The minimum insertion loss with all attenuation elements bypassed was *4.0dB*. The phase change across each path is critical in this modulation scheme and has to be identical at all times. The performance of the step attenuator was investigated and the phase change across the element was found to be dependent on its control logic. Different attenuation levels introduced different phase shifts across the component. Thus a phase shifter was inserted to offset these phase changes. The high frequency signal that reaches the power combiner can thus be represented by $A\cos(\omega t + \theta)$. At the 2 way-0° power combiner the two signals are vectorially combined and since these signals are in phase the sum becomes an algebraic addition.

This modulation scheme was used for vector voltage measurement at *1GHz* and the experimental set-up of the measurement system is shown in Figure 4.7. The output from the local oscillator is passed through a low pass filter (LPF) with a cut-off frequency of *1GHz* to minimize higher harmonics. The RF signal is then split into two parts with the first one driving the device under test (DUT) while the probe signal is derived from the second divided signal. Attenuators are used in the test circuit path to vary the signal level.

The signal to the probe is modulated as described earlier and then amplified to increase the power level. The magnitude of the signal sent to the probe is limited by the 1-dB compression output of the amplifier which is *16dBm*. This ultimately sets an upper limit on the amplitude of the circuit signal that can be measured. A phase shifter is next introduced to vary the phase of the probe signal as required in the vector voltage measurement. An adjustable delay line was used as a phase shifter. It was a mechanical structure and the phase was varied manually. The insertion loss from the delay line was less than *0.5dB*. A *10dB* coupler together with a power meter was used to monitor the amplitude of the signal which is then sent through the 50Ω feed-through termination to the probe positioned over some test point. The deflection of the probe is sensed by the deflection sensor and the amplitude of vibration at resonance (f_r) is measured using a lock-in amplifier.

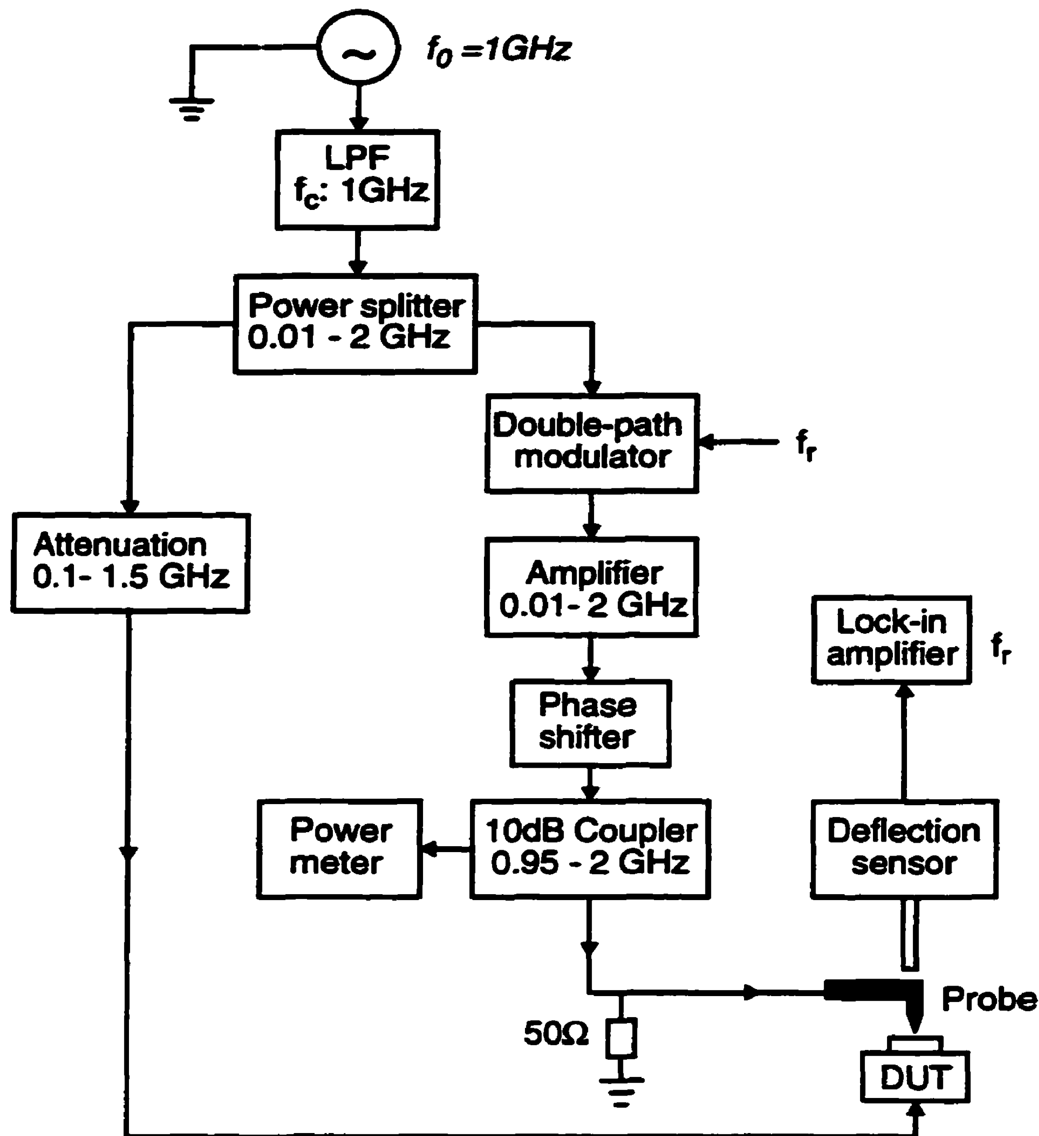

Figure 4.7: Schematic representation of the measurement system used for vector voltage measurement at *1GHz* using a double-path square wave modulation scheme.

4.4.1 Measurement Results

The use of the heterodyne technique in high frequency vector voltage measurement is demonstrated and measurement results are presented in this section. A wire probe was used in these measurements and its deflection was sensed by a fiber-optic interferometer.

The test situation would occur in linear circuits where the circuit signal is at a fixed driving frequency but undergoes changes in phase and magnitude as it propagates through various devices and components. The first test structure used to examine the performance of the measurement system was a microstrip feed-through line. The feedthrough line (thru-line) was selected since the signal on the line can be easily be characterised by measuring at its external ports. The microstrip transmission line was designed for *50Ω* impedance and was fabricated on a copper coated dielectric by rubbing out the unwanted copper using a milling machine [T-Tech]. The width of the line was calculated to be *2.25mm* for a *0.794mm* thick dielectric with $\varepsilon_r = 2.5$ using standard synthesis equations [Gupta 79]. SMA connectors were soldered at the ports of the transmission line. The performance of the microstrip structure was characterized by measuring its S-parameters on a network analyser. The forward reflection parameter S_{11} is shown in Figure 4.8. The return loss is better than *-19dB* indicating a good match at the input port.

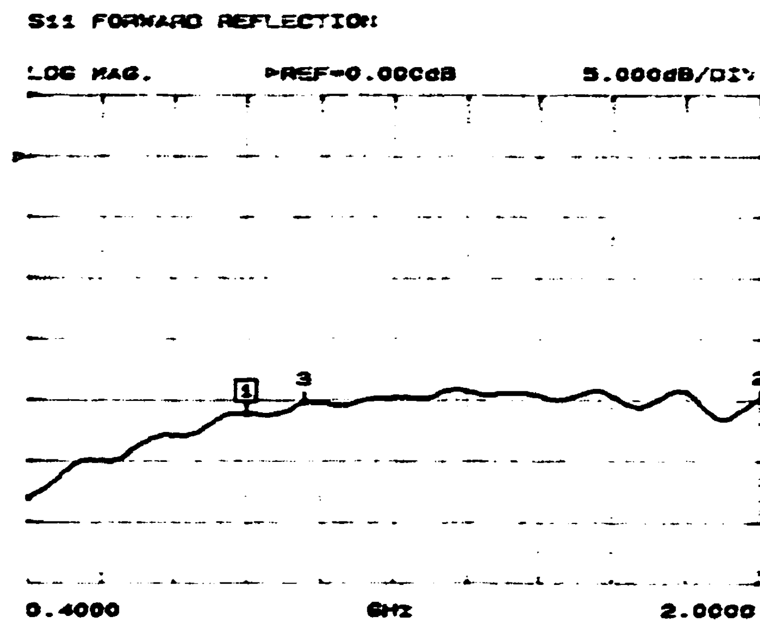

Figure 4.8: Forward reflection parameter (S_{11}) of thru-line as measured on a network analyzer.

The insertion loss was investigated by measuring the forward reflection parameter S_{21}, shown in Figure 4.9. An insertion loss better than *0.2dB* is obtained in the frequency range of *0.4-2.0 GHz*.

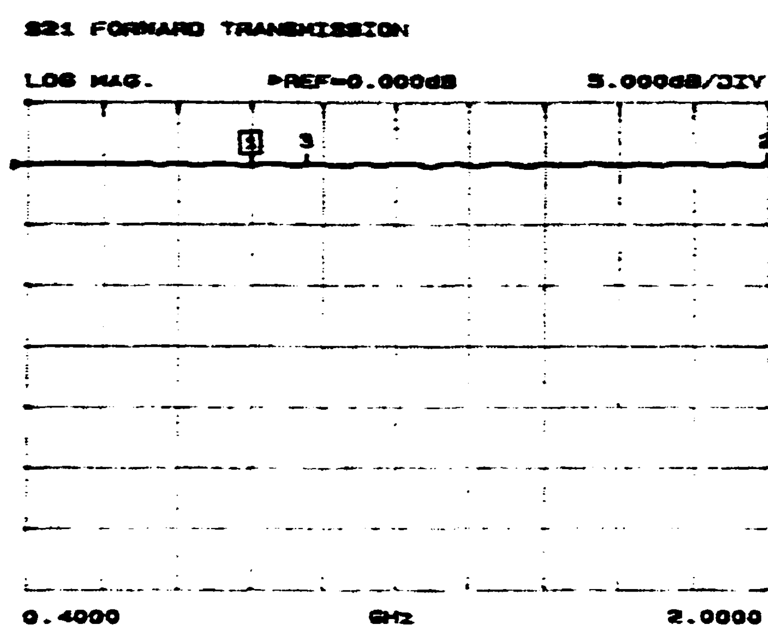

Figure 4.9: Forward transmission parameter (S_{21}) of thru-line as measured on a network analyzer.

Sinusoidal measurements were performed on the microstrip line by applying a signal, $v_c(t) = V_c \sin(2\pi f_0 t)$, to the input port. The amplitude of the circuit signal was varied by inserting attenuators in the signal path. The output signal was monitored on a high-speed sampling oscilloscope. In the heterodyne/nulling technique the circuit signal amplitude and phase are extracted by varying the probe parameters A and ϕ_p as discussed in chapter 3. The vibration amplitude of the probe at the resonant frequency is given by

$$|\Delta z|_{f_r} = \left|\frac{\partial}{\partial z}C(x, y, z) \cdot \frac{Q}{k} \cdot \frac{2}{\pi}[A - V_c \cos(\phi_p - \phi_c)]K\right|. \quad [4.4]$$

To determine the circuit signal amplitude, the phase of the probe signal is first adjusted until $\phi_p = \phi_c$ using the algorithm described in chapter 3. The parameter A was reduced by increasing the attenuation from the DSA in Figure 4.6 until $A << V_c$. The probe phase ϕ_p was manually changed using the mechanical phase shifter to obtain the two null points. Once the phase was set the amplitude, V_c, could be found by varying the parameter A until

the deflection is nulled. Figure 4.10 shows the probe deflection magnitude as a function of the probe parameter, *A*, for circuit signals amplitudes of *0.206V* and *0.320V*. The parameter *A* was extracted by measuring the power level of the probe signal using a *10dB* coupler and converting it into a voltage level.

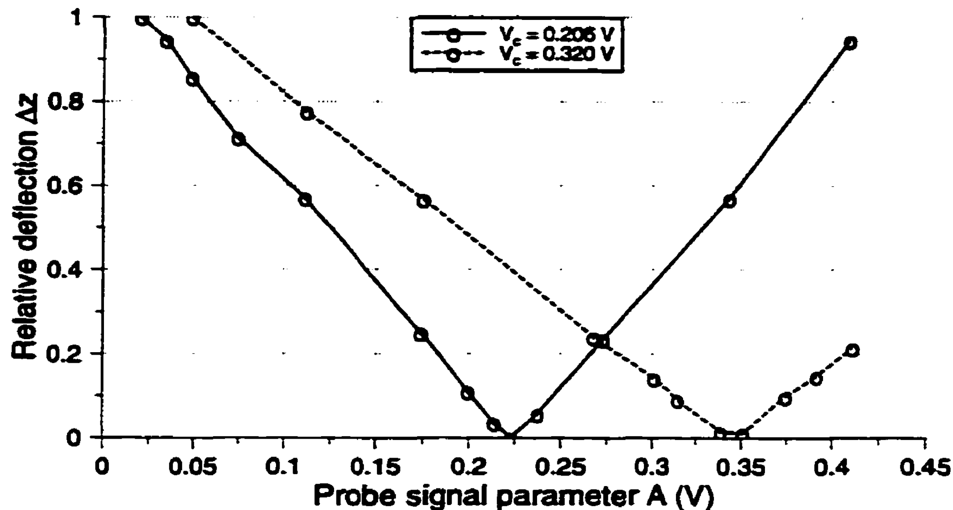

Figure 4.10: Normalised deflection signal as the probe signal parameter *A* is varied for test circuit signal amplitudes of *0.206V* and *0.320V*.

For the circuit signal amplitudes used the corresponding values of the probe parameter *A* were *0.223V* and *0.35V*. From these results, it is clear that $A \neq V_c$. This is due to losses in the signal path from where the coupler is placed to the probing tip and are difficult to characterize. Thus a calibration factor is required to translate the probe parameter, *A*, into an accurate value for the circuit signal amplitude. The probe parameter was determined for a number of different circuit signal amplitudes. These values of *A* are plotted as a function of the corresponding circuit signal amplitude V_c in Figure 4.11. A straight line fit indicates that a constant scaling factor is involved and it is easily determined from the graph.

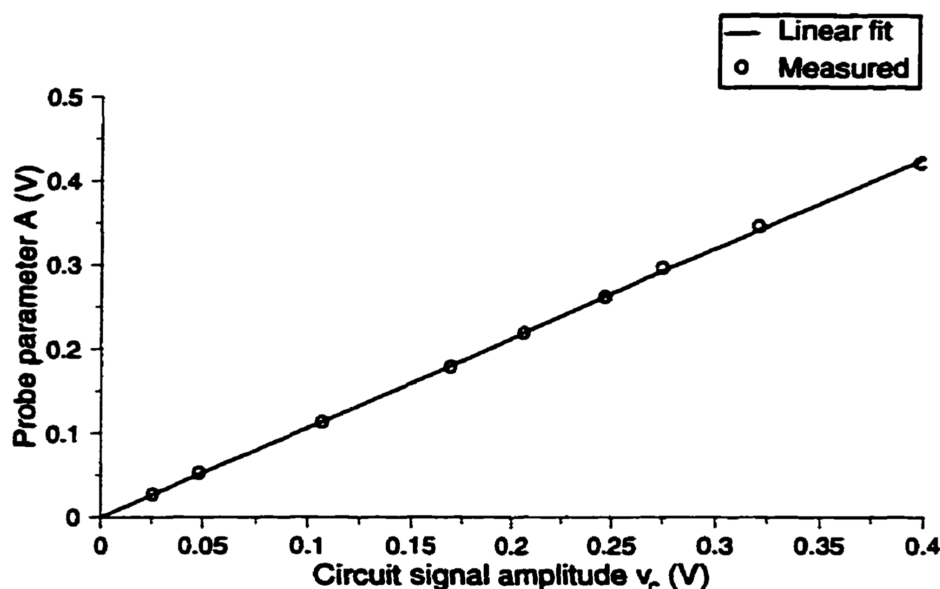

Figure 4.11: Probe parameter *A* as a function of circuit signal amplitudes V_C. A straight line is fitted onto the measured data points.

The maximum signal that can be measured is limited by the *1dB* compression output of the amplifier as mentioned earlier. The probe parameters *A* and *K* are limited by the amplifier output and one can only be increased at the expense of decreasing the other. A trade-off is chosen between the measurement range, defined by the *A* values, and the signal-to-noise ratio which depends on *K* (probe deflection $\propto K$). In the measurement system, the voltage sensitivity is determined primarily by the step size of the DSA used to vary the probe parameter *A*. The attenuation could be changed in steps of *0.5dB* resulting in a voltage sensitivity of *0.25dB*. The sensitivity in the phase measurements were estimated to be within $\pm 2^o$.

The measurement capability of the instrument was further investigated by varying the phase of the probe signal after the probe parameter *A* that minimises the deflection corresponding to a circuit voltage of *0.206V* has been determined. This result is shown in Figure 4.10. The resulting normalized deflection amplitude is plotted as a function of ϕ_p in Figure 4.12. The measured results matches well with the theoretical $[1 - \cos(\phi_p - \phi_c)]$ response.

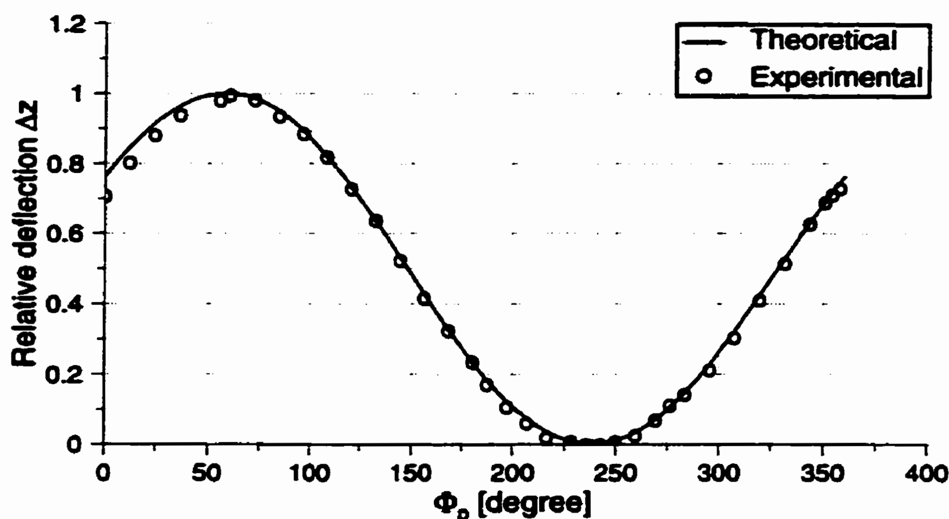

Figure 4.12: Normalized deflection signal as the phase of the probe signal is varied. The phase of the test circuit signal ($V_C = 0.206V$) was initially determined as $\phi_C = 238^o$ and the probe signal adjusted to null the deflection with ϕ_p set as 238°. Both the measured and theoretical responses are plotted.

While the measurements on the thru-line presented so far can be easily made using conventional methods they help to demonstrate the heterodyne technique and enabled the determination of the scaling factor involved in the EFM probing. It is important to note that the scaling factor remains unchanged regardless of the DUT. Thus, once determined with the thru-line, the same scaling factor can be used for all DUTs.

The next set of measurements were performed on the internal nodes of a commercial MMIC low noise amplifier (LNA) from Texas Instruments and they provide a more appropriate application of the EFM instrument. The amplifier is a GaAs monolithic low-noise-amplifier and has three FET stages with resistive feedback [TI-LNA]. The amplifier was packaged in a microstrip structure at Communications Research Centre, Ottawa [CRC1] and a photograph of the packaged circuit is shown in Figure 4.13.

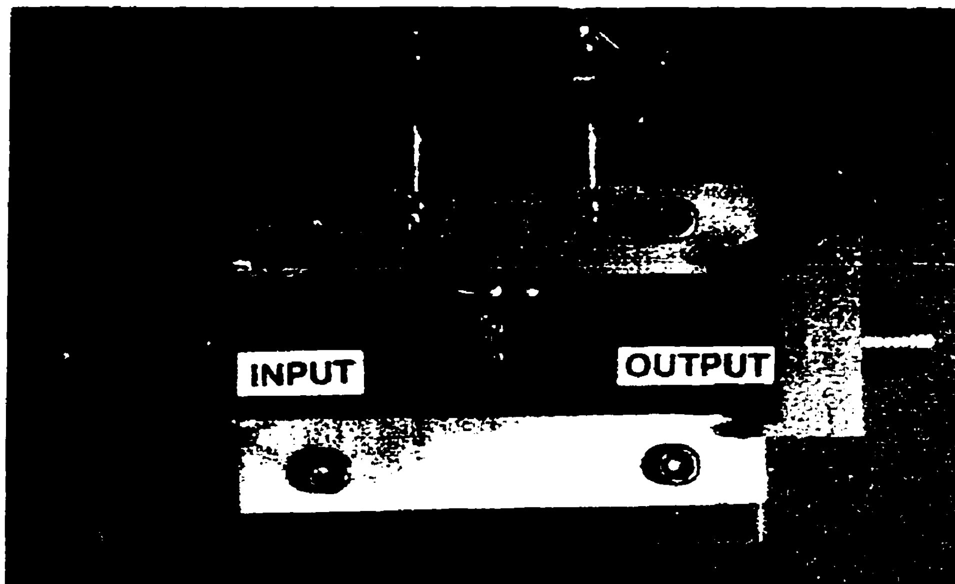

Figure 4.13: Photograph of the Texas Instrument Low Noise Amplifier used as a test circuit in EFM vector voltage measurements. The integrated circuit is packaged by bonding to the microstrip lines.

The nominal gain of the amplifier over a *0.1-3.5GHz* range is *18dB* and a single *+12V* power supply is required for its operation. The *1dB* compression output of the amplifier is *15dBm*. The performance of the amplifier was verified by measuring the forward transmission and reflection parameters on a network analyser. The S_{21} parameter is given in Figure 4.14 and the gain of the amplifier at *1GHz* is *17.4dB*. When measuring active devices such as amplifiers on a network analyzer care must be taken to avoid damage from the amplified output. A wideband *20dB* attenuation was used. The insertion loss of the attenuator was initially characterised and its effect was factored out from the measured results. The S_{11} parameter of the LNA is shown in Figure 4.15 and a return loss better than *15dB* is obtained at *1GHz*.

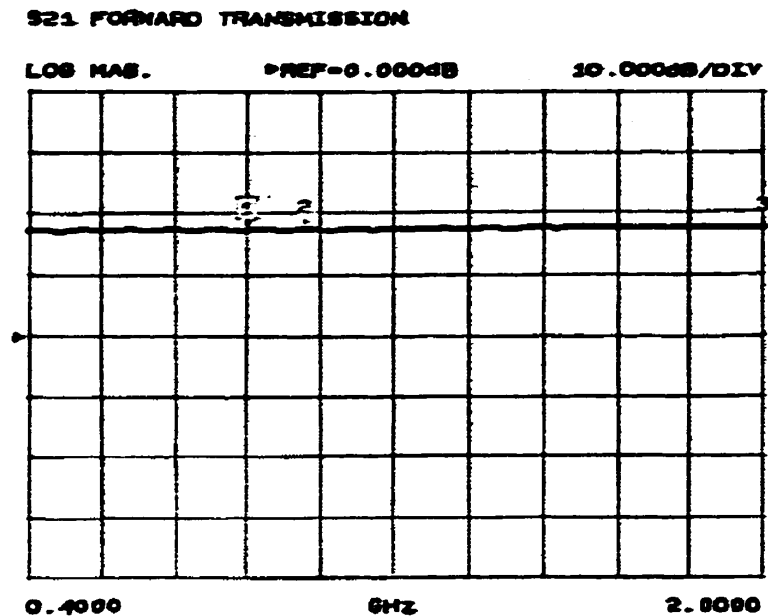

Figure 4.14: Forward transmission parameter (S_{21}) of Ti-LNA as measured on a network analyzer.

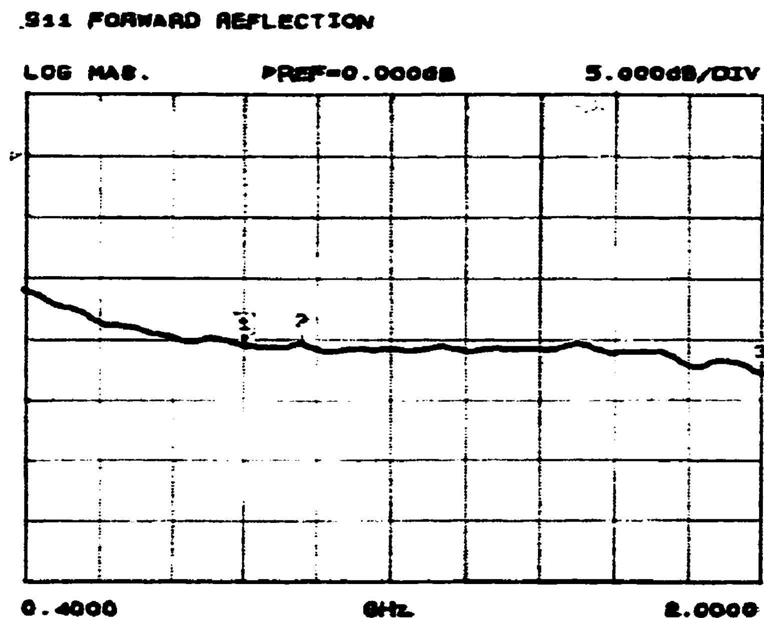

Figure 4.15: Forward reflection parameter (S_{11}) of thru-line as measured on a network analyzer.

A microphotograph of the amplifier layout and the circuit schematic are shown in Figure 4.16. Measurements were performed at the input and output pads and two internal

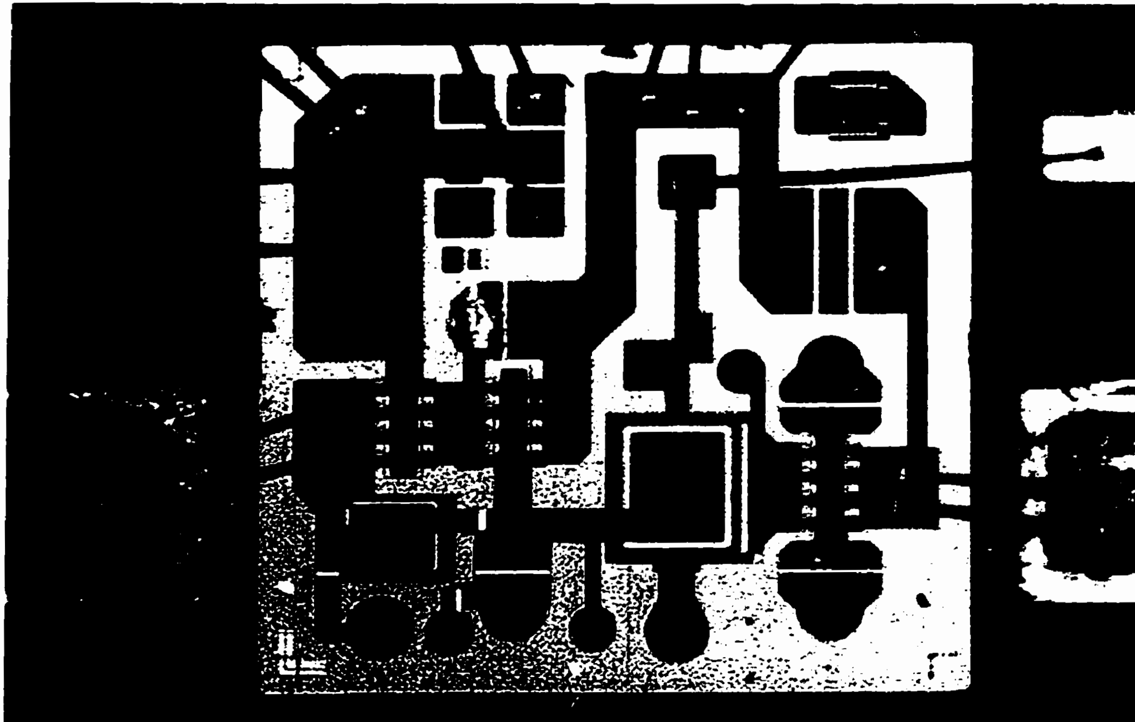

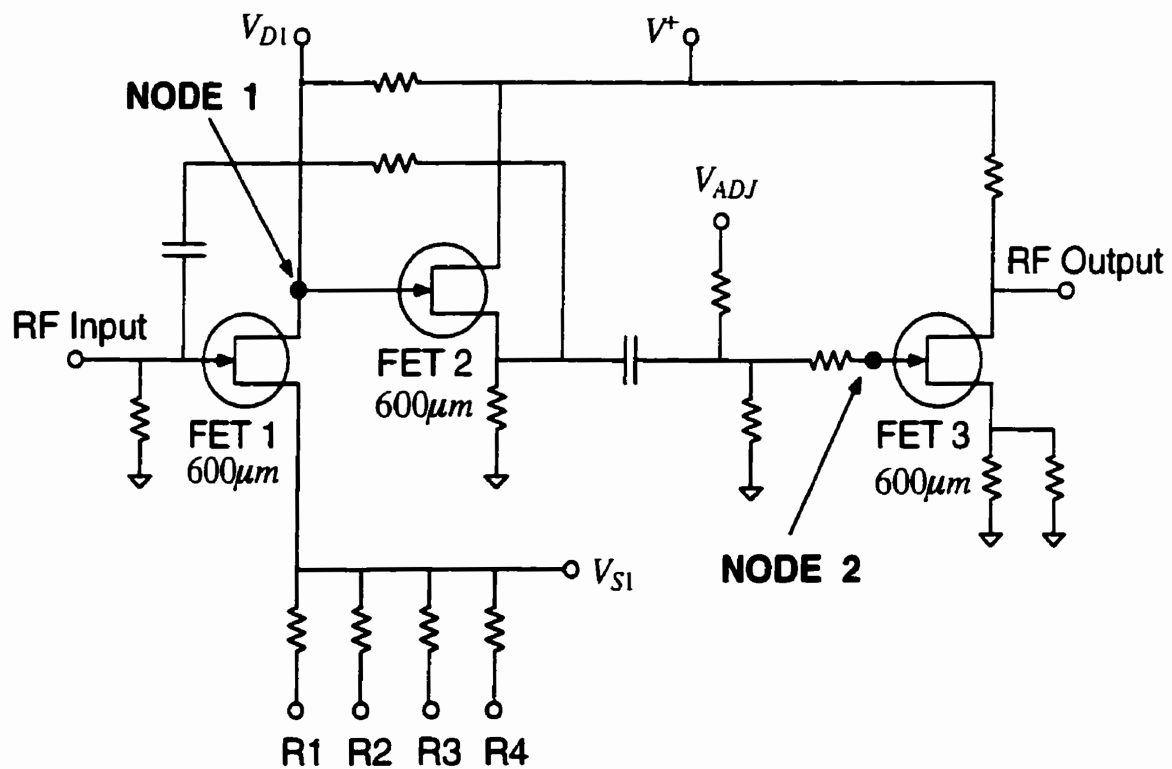

Figure 4.16: Texas Instrument Low Noise Amplifier (TI LNA); microphotograph of the circuit (top) and the circuit schematic representation of the MMIC (bottom).

nodes as identified in Figure 4.16. Node 1 is the output of the first FET while Node 2 is the input to the third FET. The input and output of the amplifier circuit was bonded to the pads lying on the microstrip lines where the measurements were made. The dimensions of the chip are about *1.5mm x 1.5mm*. While the signals at the input and output ports can be characterised by using a standard oscilloscope or network analyzer, the internal signals cannot be easily determined by conventional techniques.

For comparison purposes a high impedance active contact probe (Picoprobe from [GGB]) was used to measure the signals of the points of interest. The measurement system is shown in Figure 4.17.

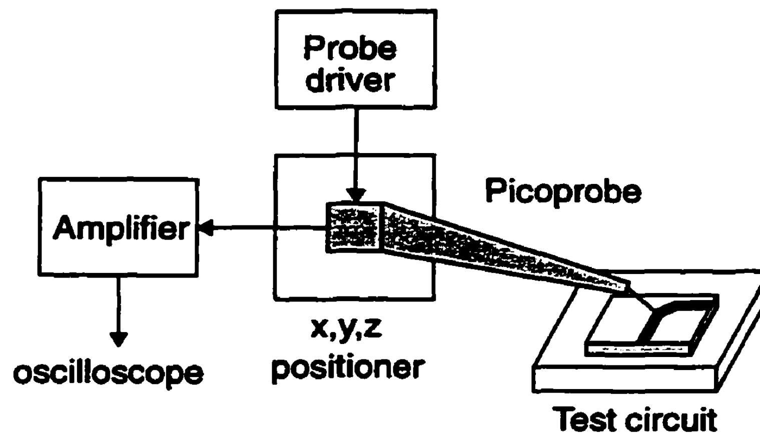

Figure 4.17: Measurement system for contact probing with an active probe (Picoprobe). Direct contact is made by a fine tungsten tip to a test point on the circuit.

An amplifier stage was used to increase the signal level obtained from the contact probe since the probe output is attenuated 20:1. The probe driver supplies the bias voltage for the MOS transistor located at the probing end. The probe tip is directly connected to the unprotected gate of the transistor resulting in a low capacitive load from the probe (*0.04pF* according to specifications). The probe has a bandwidth of *1GHz*. The operation of the probe-amplifier system was verified by measuring known signals on a thru-line at *1GHz*. The probe results are plotted as a function of the circuit signal amplitude in Figure 4.17. The measured points were fitted onto a straight line which can be used as a calibration curve. The maximum deviation of the measured points from the calibration curve was

less than *10mV*.

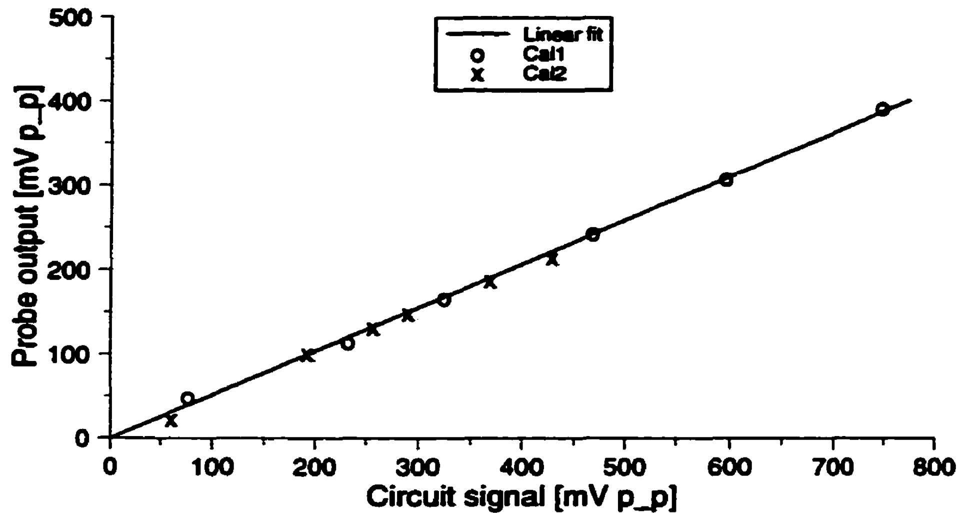

Figure 4.18: Calibration curve for active contact probe measurement system at 1GHz. Results are plotted from two measurement attempts and a straight line is fitted through the measured data points.

The results from the measurement of the LNA are presented next. The EFM probe was positioned approximately *1μm* over the test point. A small input signal was applied to the amplifier with the output connected to a *50Ω* input of an oscilloscope. In such a measurement set-up the output can be continuously monitored while the internal signals are being probed. A negligible disturbance of the output signal was observed during EFM probing showing the non-invasive nature of the measurement. In contrast, the output level changed by about *10mV* when the output pad was probed by the active contact probe due to the higher loading from the active probe (*0.04pF* compared to less than *1fF* for the EFM). Table 1 shows the results obtained by probing the four test points using the EFM and the active contact probe for similar input signal levels. The extracted phases of the signal were referenced to the output signal phase. The results from these measurements match quite well except for the phase of the input signal. The small voltage level made an accurate measurement of the phase by the active contact probe difficult. The voltage sensitivity is calculated using the *0.5dB* step size of the DSA. The probe parameter can be adjusted to within *0.25dB* of the circuit signal amplitude. Thus, the voltage sensitivity varies as the the amplitude of the test signal. This effect was observed experimentally.

The results in Table 1 together with the circuit topology shown in Figure 4.16 indicate that most of the signal amplification is done by the first FET. The other two transistors act as buffer stages. Circuit simulation was not possible since the FET parameters are not available.

Table 1: Vector waveform measurement of TI-LNA at *1GHz*

	Input	Node 1	Node 2	Output
EFM	$45.1 \pm 1.3\ mV$ $\angle 0^o \pm 2^o$	$359 \pm 10.5\ mV$ $\angle 165^o \pm 2^o$	$292 \pm 8.5\ mV$ $\angle 162^o \pm 2^o$	$384 \pm 11.2\ mV$ $\angle -38^o \pm 2^o$
Contact probe	$47.6\ mV$ $\angle ?$	$348\ mV$ $\angle 162^o$	$298\ mV$ $\angle 155^o$	$410\ mV$ $\angle -38^o$

For a properly matched amplifier, S_{21} is determined as the ratio of the output voltage to the input voltage. The S_{21} parameter is calculated from the probing results and compared in Table 2 with the specification data as well as the value obtained from the network analyzer measurement. The sensitivity in a S_{21} measurement by the EFM probe is *0.5dB* since the voltage sensitivity of the technique is *0.25dB*. The sensitivity in the contact probe measurement is estimated from the deviation of the measured data from the linear calibration curve in Figure 4.18. The lower gain from the network analyzer results are most likely due to mismatch and loss in the text fixture (Figure 4.13) used to mount the device. This does not effect the EFM results and is an advantage of the method.

Table 2: Forward transmission parameter, S_{21}, of the TI-LNA

Contact probe	EFM	Data sheet	Network analyzer
$18.5\ dB$	$18.6 \pm 0.5\ dB$ $\angle -38^o \pm 4^o$	$18.5\ dB$ $\angle -37^o$	$17.6\ dB$

The reference plane for the S_{21} parameter from the data sheet is specified as the center of the device bond pads. In the EFM probing, measurements were made on the bond pad

lying on the microstrip line of the package as indicated in Figure 4.16. The effect of the bond wires on the measurement results was investigated. The length, l, of the bond wire was estimated at $0.5mm$ and a diameter, d, of $22\mu m$ was assumed (a typical value). The main parasitic from a bond wire is its inductance which was estimated by

$$L = 0.2l\left[\ln\left(\frac{2l}{d}\right) - 1\right]. \qquad [4.5]$$

In [4.5] the inductance, L, is given in nH if l and d are in mm. The inductance of a single bond wire was estimated at $0.35nH$. From computer simulation using PUFF (a software for microwave circuit design) for two wires in parallel, the insertion loss across the bond wires was found to be negligible below $5GHz$. The phase change introduced was less than 2° at $1GHz$ and below 3° at $2GHz$.

The results presented in this section demonstrate that the heterodyne measurement system performs well. However, the practical implementation of the double path modulation technique used here is quite complex. A number of discrete components are used and careful calibration of each component is necessary. The digital step attenuator introduced a variable phase shift which necessitated the use of a phase shifter. Due to the lack of an electronic phase shifter, the heterodyne method could not be automated. The overall measurement system was quite complicated and tedious to operate. An alternative modulation technique was thus investigated with the intent to simplify the measurement technique. This method was based on an I/Q modulator and it is discussed next.

4.5 I/Q Modulation

The basis behind this modulation technique is the in-phase/quadrature (I/Q) modulator/demodulator schemes often used in digital communication systems. In the implementation of this modulation scheme a commercially available I/Q modulator (MIQC-895M) from Mini-Circuits was used [Mini-Circuits]. The MIQC-895M has a narrow carrier bandwidth between *868-895 MHz*. The modulator came as a plug-in chip and a printed circuit

board was prepared to mount the component using the milling machine [T-Tech].

The frequency range of the modulating signals is from DC to *2MHz*. The I/Q modulator consists of a 90° splitter, two mixers, and a 0° splitter/combiner as shown in Figure 4.19. The modulating signals are the I and Q signals which are upconverted by the mixers.

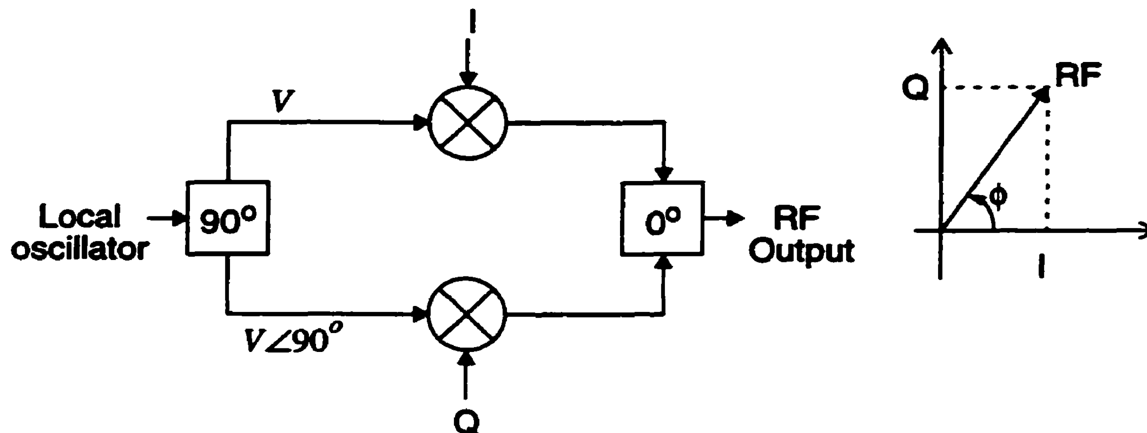

Figure 4.19: Schematic representation of the I/Q Modulator. The RF signal can be represented as a vector sum of the two orthogonal I and Q components.

The local oscillator signals to the mixers are 90° apart and therefore the outputs of the mixers are orthogonal. The RF signal can thus be represented in X-Y coordinates as magnitude of X-Y vectors. In digital audio, X is replaced by I (In-phase) and Y by Q (Quadrature), hence the name I/Q modulator.

The principle attraction of this component is its capability of modulating the amplitude as well as varying the phase of the probe signal as required in the heterodyne vector voltage measurement technique. A much simpler measurement system can thus be implemented. In the square wave modulation scheme, the signal sent to the probe is of the form

$$(A + KG(t)) \cos (w_0 t + \phi) \qquad [4.6]$$

where A, K and ϕ are user-controlled parameters. This modulation scheme is implemented using the I/Q modulator as illustrated in Figure 4.20. Synchronised square wave modulating signals are used at the I and Q ports. The frequency of the square wave signals is cho-

sen at the probe resonant frequency f_r. By varying the amplitude and DC offset of these signals the amplitude of the high frequency carrier can be modulated at f_r and its relative phase ϕ can also be changed. For a relative phase ϕ greater than 90° a phase difference between the modulating signal is introduced. If, for example, ϕ lies between 90° and 180° then the signal at the I-port lags the signal at the Q-port by 90°.

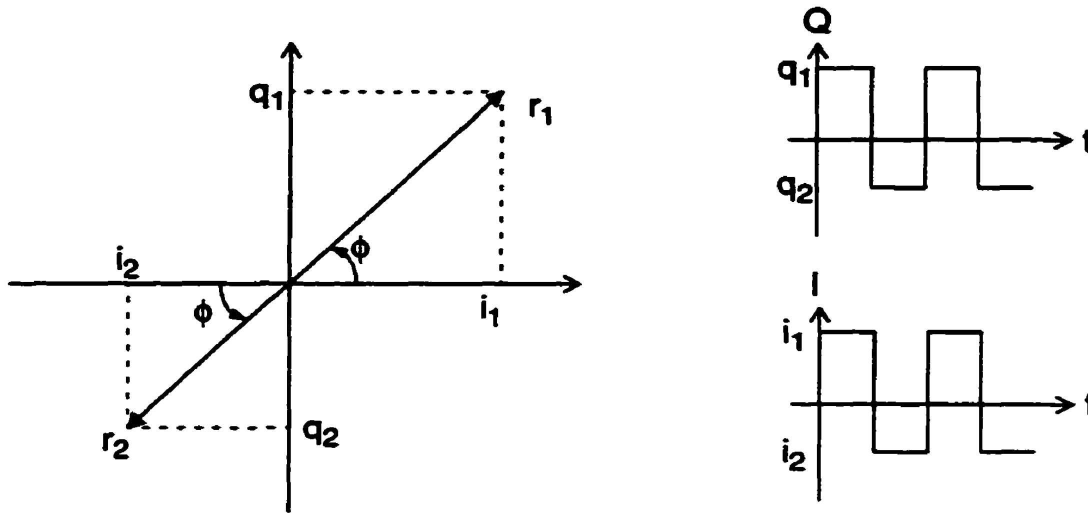

Figure 4.20: Illustration of square wave modulation using the I/Q modulator for the case when $0^o < \phi < 90^o$.

In Figure 4.20 the amplitude of the high frequency signal changes between r_1 and r_2 resulting in $A = (r_1 - r_2)/2$ and $K = (r_1 + r_2)/2$ in equation 4.6. For the case illustrated in Figure 4.20, both r_1 and r_2 are defined to be positive and r_1 is assumed to be greater than r_2. The parameters A and K are adjusted by changing the amplitude and offset of the modulating signals at the I and Q ports. If both vectors of the high frequency signal resulting from the modulation are of the same phase then r_2 is considered to be negative so that the same definitions for A and K, mentioned earlier, are valid (assuming $|r_1| > |r_2|$).

The performance of the mixers in the I/Q modulator is important for the measurement system and the component's behaviour was experimentally characterized to investigate deviations from linearity. In the first experiment the I/Q modulator was driven by a local oscillator at $881MHz$ with an input power of $9dBm$. A low-pass filter with a cut-off frequency of $1GHz$ was used to filter out the higher harmonics. A variable DC voltage was

applied to the I-port and the Q-port was grounded. As the DC voltage level at port I was varied the magnitude of the RF output was measured on an oscilloscope and the result is plotted in Figure 4.21.

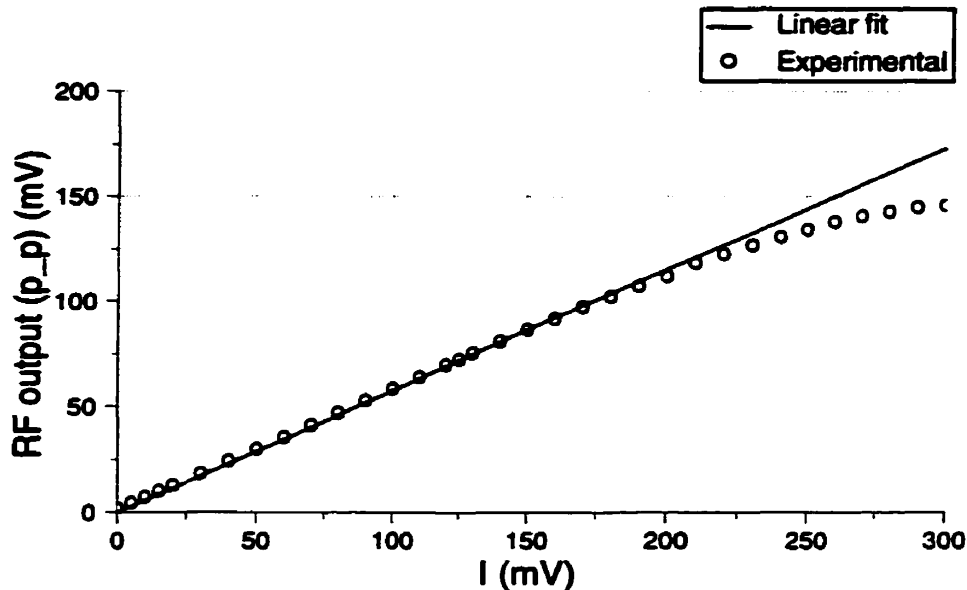

Figure 4.21: Characterization of the performance of the I/Q modulator. LO frequency was 881MHz. The peak-to-peak magnitude of the RF output was measured as the DC voltage at port I was varied with port Q grounded. A straight line is fitted through the measured data points.

A straight line is fitted on the measured data points in Figure 4.21. The performance of the I/Q modulator deviates from linearity for high voltage levels at the I-port. During the measurements the phase of the RF output was monitored on an oscilloscope and it changed by less than $\pm 3^{o}$. Ideally no phase change is expected since the modulating signal at the Q-port is kept constant at *0V*.

The next measurement was performed by varying the DC signals at both the I and Q ports of the modulator. The linear portion of the curve in Figure 4.21 was selected and thus the maximum level of the modulating signal used was *0.2V*. In this case the amplitude and the relative phase change of the RF output were measured and the results are tabulated in Table 3. A theoretical response assuming linear behaviour of the I/Q modulator is also computed and presented in Table 3.

Table 3: Response of the modulator as a function of I and Q modulating signals

I (v)	Q (v)	RF output (mV) (measured)	RF output (mV) (theoretical)
0.2	0.2	163.0 ∠0°	163.0 ∠0°
0.2	0.15	144.0 ∠-8°	144.1 ∠-8.1°
0.2	0.1	127.0 ∠-20.5°	128.9 ∠-18.4°
0.2	0.05	117.0 ∠-33.3°	118.8 ∠-31.0°
0.2	0.0	113.3 ∠-47°	115.3 ∠-45.0°
0.2	-0.05	117.0 ∠-61°	118.8 ∠-59°
0.2	-0.1	128.0 ∠-74°	128.9 ∠-71.6°
0.2	-0.15	146.0 ∠-82.5°	144.1 ∠81.9°
0.2	-0.2	165.0 ∠-90°	163.0 ∠-90°
-0.2	0.2	161.0 ∠89°	163.0 ∠90°
-0.2	0.15	141.0 ∠98°	144.1 ∠98.1°
-0.2	0.1	122.0 ∠107°	128.9 ∠108.4°
-0.2	0.05	111.0 ∠122°	118.8 ∠121.0°
-0.2	0.0	108.0 ∠135°	115.3 ∠135°
-0.2	-0.05	113.0 ∠149°	118.8 ∠-211.0°
-0.2	-0.1	123.0 ∠-198°	128.9 ∠-198.4°
-0.2	-0.15	141.0 ∠-187°	144.1 ∠-188.1°
-0.2	-0.2	160.0 ∠-180°	163.0 ∠-180.0°

Table 3: Response of the modulator as a function of I and Q modulating signals

I (v)	Q (v)	RF output (mV) (measured)	RF output (mV) (theoretical)
0.1	0.2	$132.0 \angle 16.4^o$	$128.9 \angle 18.4^o$
0.1	0.1	$85.7 \angle -3^o$	$81.5 \angle 0.0^o$
0.1	0.0	$61.7 \angle -47^o$	$57.6 \angle -45.0^o$
0.1	-0.1	$83.5 \angle -88.6^o$	$81.5 \angle -90.0^o$
0.1	-0.2	$130.0 \angle -107^o$	$128.9 \angle -108.4^o$
-0.1	0.2	$126.0 \angle 71^o$	$128.9 \angle 71.6^o$
-0.1	0.1	$76.0 \angle 91.5^o$	$81.5 \angle 90.0^o$
-0.1	0.0	$57.0 \angle 138^o$	$57.6 \angle 135.0^o$
-0.1	-0.1	$83.0 \angle -180^o$	$81.5 \angle -180.0^o$
-0.1	-0.2	$131.0 \angle -161^o$	$128.9 \angle -161.6^o$

A close agreement is observed between the experimental and theoretical results. A linear behaviour of the I/Q modulator assuming similar signal levels is a reasonable assumption. In implementing the heterodyne technique using the I/Q modulator two DS-345 signal generators [SRS] were used two provide the modulating signals at the I and Q ports. These generators were operated in locked-mode so that the relative phase between them are known and constant. The operation of the DS-345 can be computer controlled and all the parameters in the heterodyne nulling technique were varied using a computer program in a feedback loop. This enabled automation of the measurement system.

Referring to the case illustrated in Figure 4.20 the I and Q modulating signals can be described in terms of the phase and magnitude of the desired high frequency signals, r_1 and r_2. The peak-to-peak amplitudes of the modulating signals at the I and Q ports are

given by

$$I_{pp} = (r_1 + r_2)\cos\phi \ , \ Q_{pp} = (r_1 + r_2)\sin\phi \qquad [4.7]$$

assuming $r_1 > r_2$. The DC offsets of the modulating signals are given by

$$I_{off} = \left(\frac{r_1 - r_2}{2}\right)\cos\phi \ , \ Q_{off} = \left(\frac{r_1 - r_2}{2}\right)\sin\phi\,. \qquad [4.8]$$

The I and Q signals can be easily derived for other cases with ϕ ranging from 0° to 360°. It is these values that are sent to the signal generators by the computer program developed for these measurement. Since the signal levels at the I/Q ports are kept small to maintain linearity *20dB* attenuators were used in the path from the DS-345 to the I/Q ports. The sensitivity of the system is thus increased by extending the range of the modulating signals at the output of the signal generators. A larger change in the output from the DS-345 is more accurately set than a smaller one. From Figure 4.21, the maximum signal level at the I-port was found to *0.2V* for linearity. Without the *20dB* attenuator this would result in a maximum value of 0.2 for r_1 while the maximum becomes *2.0* with the *20dB* attenuator. It should be noted the parameters r_1 and r_2 are not identical to the high frequency output. They are used as variables to implement the nulling/heterodyne technique. In reality the high frequency outputs are linearly scaled by these numbers.

A block diagram of the measurement system is shown in Figure 4.22. The high frequency signal is once again split to simultaneously drive the probe signal modulating electronics and the circuit under test. An amplifier stage is used to increase the power level of the modulated probe signal while the attenuators in the circuit signal path allows for the variation of the circuit signal level. The lock-in amplifier is used to sense the deflection of the probe at its resonant frequency. This deflection amplitude is then read by the computer through a digital-to-analog converter. The measurement system was calibrated by measuring the power of the RF signal after the amplifier in the probe-signal path for known settings on the I/Q modulator. Thus the probe parameters, *A* and *K*, resulting from specified values for r_1 and r_2 could be extracted.

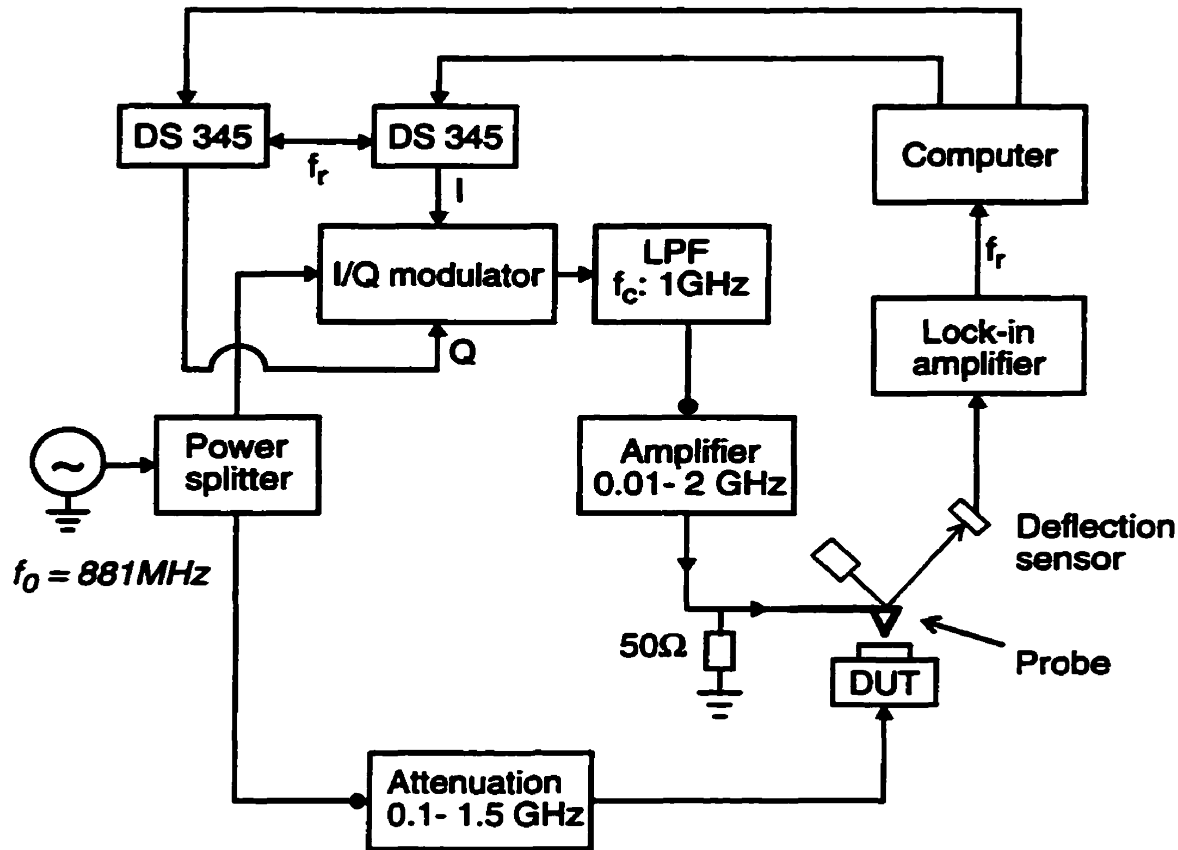

Figure 4.22: Block diagram of the measurement system using the I/Q modulator for vector voltage measurement at 881MHz.

4.5.1 Measurement Results

For the measurement results presented here, a micromachined cantilever probe was employed in the EFM instrument and the probe deflection was monitored by a beam bounce detection technique. Vector voltage measurement is first demonstrated on the thru-line described in section 4.4.1. A sinusoidal signal with an amplitude of *0.253V* was applied to the thru-line. The phase of the signal was first determined by finding the two null points with $A << Vc$. The high frequency vectors r_1 and r_2 were 180° out of phase and r_1 slightly greater that r_2. The measured normalised amplitude of deflection at the probe resonance, as the two null points are located, is shown in Figure 4.23. The theoreti-

cal response which is proportional to $|A - V_c cos\,(\phi_p - \phi_c)|$ is also fitted on the measured data. The phase of the circuit signal is obtained as $\phi_c = 327^o$.

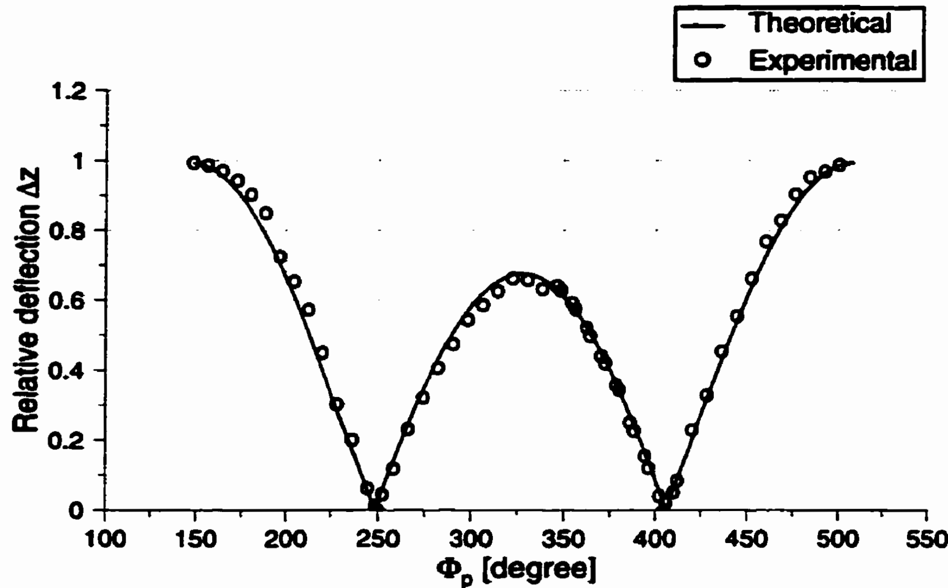

Figure 4.23: Determination of the circuit signal phase by locating the two null points. Both the measured data and the theoretical fit are displayed.

Once the phase has been set and the deflection amplitude with $\phi_p = \phi_c = 327^o$ has been nulled $(A = V_c)$, the deflection of the probe at its resonance was measured as a function of the probe phase ϕ_p. The measured normalized result is compared with the theoretical response $[1 - cos\,(\phi_p - 327^o)]$ in Figure 4.24.

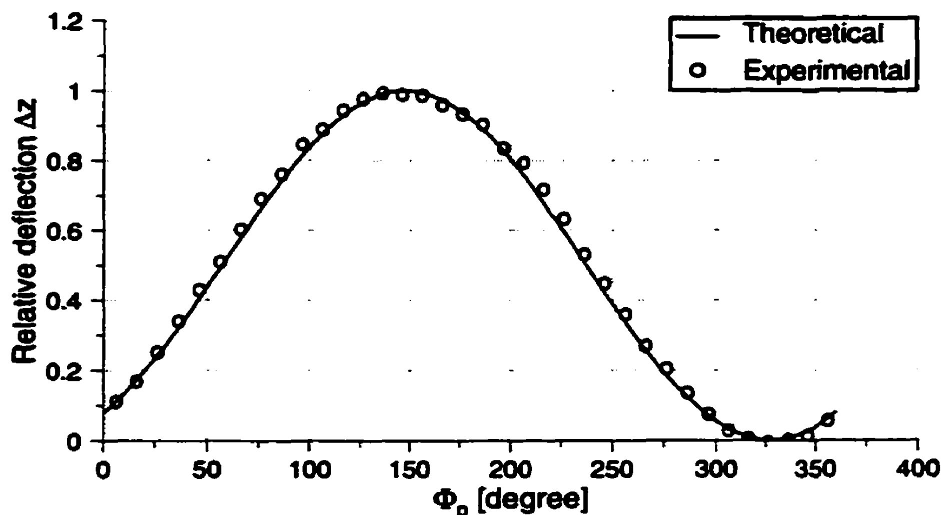

Figure 4.24: Experimental and theoretical response of the probe deflection as a function of the phase of the probe signal ϕ_p with $\phi_c = 327^o$ and the probe parameter $A = V_c$.

The phase measurement capability of the instrument was next investigated. A mechanical delay line was placed before the thru-line to introduce an adjustable phase shift in the circuit signal, $V_c \, sin(\omega_0 t + \phi_c)$. The phase change of the circuit signal was monitored on an oscilloscope. The experimental data from the EFM are compared with the oscilloscope results in Table 4 and an agreement within 3° is observed. The circuit signal amplitude was $0.26V$ in these measurements.

Table 4: Phase measurement using I/Q modulation at 881MHz

$\Delta\phi_c$ (Oscilloscope)	$\Delta\phi_c$ (EFM)
0°	0°
4.3^o	3.75^o
21.0^o	19.5^o
41.6^o	39.25^o
105.0^o	104.5^o
211.0^o	208.0^o

In the heterodyne technique for vector voltage measurement, the amplitude of the circuit signal is determined once the phase has been accurately set. A nulling technique is employed by adjusting the probe parameter A. In the algorithm used the parameter A is increased by decreasing the magnitude of the high frequency vector r_2 with r_1 kept constant. Assuming $r_1 > r_2$, the probe parameters A and K are given by $(r_1 - r_2)/2$ and $(r_1 + r_2)/2$. Here the amplitudes of the RF output is equal to the parameters r_1 and r_2 for modeling purposes. With $\phi_p = \phi_c$ the deflection of the probe at the resonant frequency, f_r, can be written as

$$|\Delta z| \propto K(A - V_c) = \left(\frac{r_1 + r_2}{2}\right)\left(\frac{r_1 - r_2}{2} - V_c\right). \qquad [4.9]$$

The theoretical response of the probe deflection as the parameter A is varied is shown in Figure 4.25 for different values of V_c.

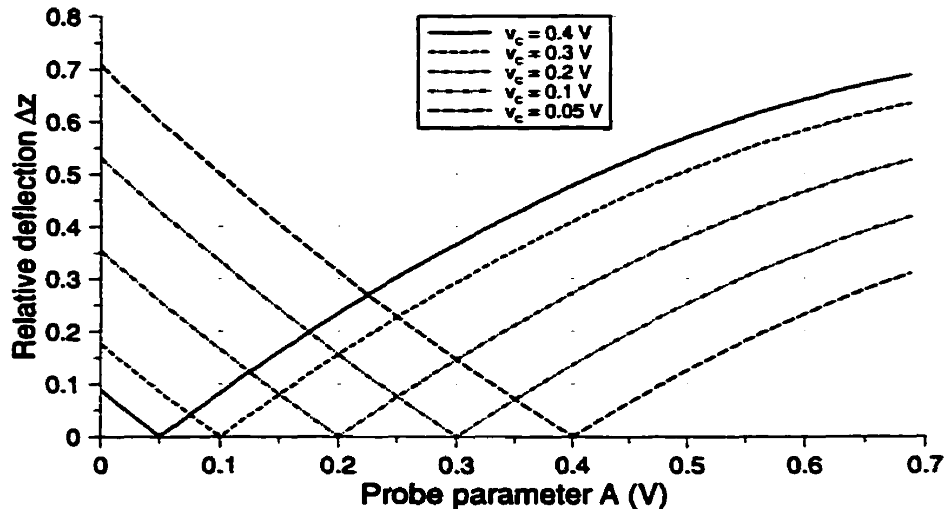

Figure 4.25: Theoretical response of the probe deflection at f_r as the probe parameter A is varied for the cases when $V_c = 0.05, 0.1, 0.2, 0.3$ and 0.4 V.

The circuit signal amplitude on the thru-line was varied and the deflection nulled after the phase has been set. The nulling curves obtained from measurement are shown in figure 4.26 where the relative probe deflection is plotted as a function of the probe parameter A for $V_c = 0.08, 0.12, 0.15, 0.20$ and 0.25 V. The measured response is similar to the theoretical one.

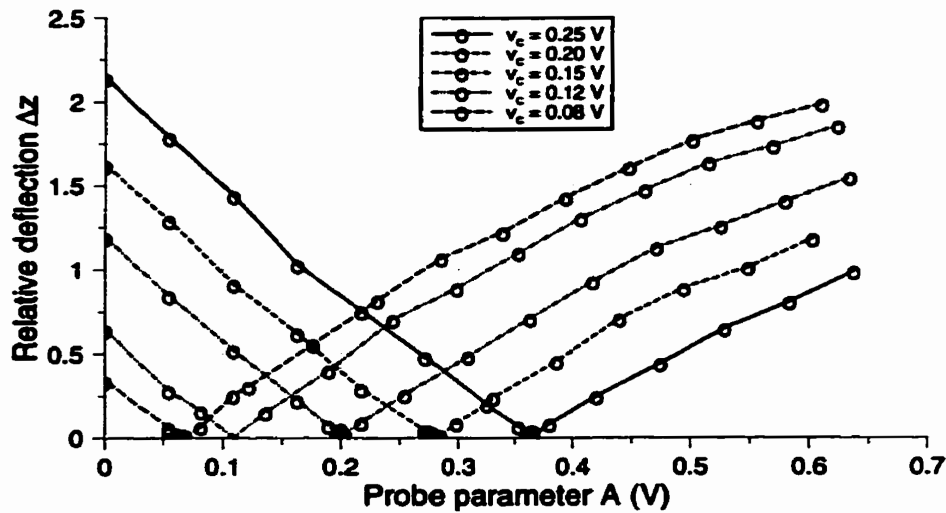

Figure 4.26: Experimental nulling curves where the probe deflection is plotted as a function of the probe parameter A for V_C = *0.08, 0.12, 0.15, 0.20* and *0.25 V.*

The probe parameter, A, extracted from these measurement do not match with the circuit signal amplitude. Probe mismatch and loss in the probe matching circuitry could be responsible for this discrepancy. A calibration curve is therefore required and the one obtained from these results proved to be non-linear. This is a result of the small non-linearity present in the performance of the I/Q modulator which is amplified in the measurement system.

The measurement was repeated and the probe parameter A, where the deflection is nulled, was measured using a *10dB* coupler placed before the *50Ω* feedthrough termination in Figure 4.22. The probe deflection nulling for amplitude and phase measurement was still controlled by the computer in a feedback loop. The resulting calibration curve where the probe parameter, A, is plotted as a function of the circuit signal amplitude is given in Figure 4.27. Three different measurements were performed with the parameter r_l = *1.6, 1.7* and *1.8*. The experimental results are easily fitted on a linear calibration curve. The measured data deviated by less than *10mV* from the linear calibration curve. The typical time taken for the measurement of a single data point was about two minutes. The measurement system can be completely automated if the non-linearity of the I/Q modula-

tor is completely characterized and taken into account during the EFM probing.

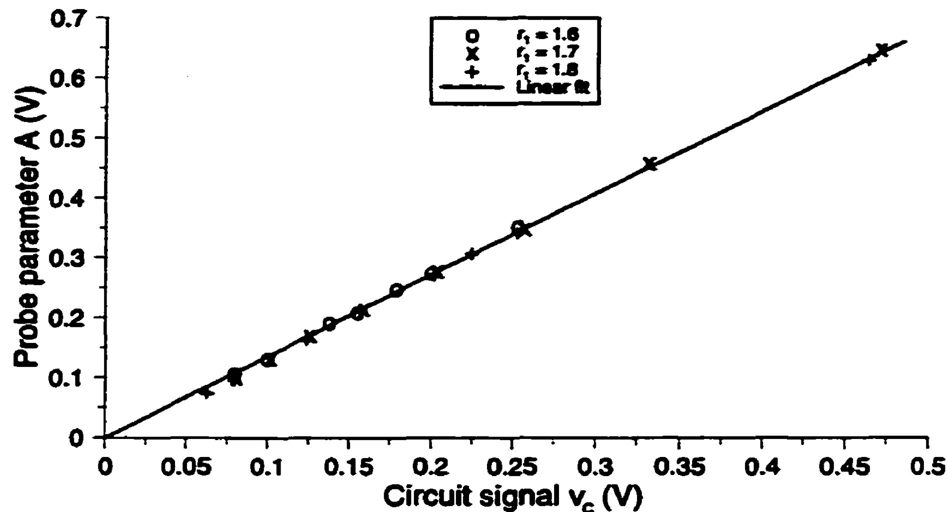

Figure 4.27: Calibration curve for amplitude measurement. The probe parameter A is plotted as a function of the circuit signal amplitude for $r_1 = 1.6, 1.7$ and 1.8. A straight line is fitted on the experimental data.

In all these measurements, the output signal from the thru-line was continuously monitored on an oscilloscope. A small level of signal disturbance was observed and it was more noticeable at smaller circuit signal levels. This effect is due to the coupling of the probe signal onto the circuit under test. The coupled signal was measured on an 50Ω oscilloscope from one port of the thru-line with the other end terminated by a *50Ω* load as shown in Figure 4.28. The amplitude of the coupled signal was in the order of *15mV*. The significant disturbance is due to a larger coupling capacitance resulting from the probe structure used.

The probe-circuit coupling can be modeled using a simple static equivalent circuit. The pyramidal tip of the micromachined probe is about *4μm* long and the tip is usually positioned about *1-2 μm* over the test point. The micromachined probe is about *200μm* long and is attached to a rather bulky holder. The coupling capacitance from the entire structure is significantly higher than what would be expected from the probing tip alone. Using a simple parallel plate model with an effective area of $0.1mm^2$ and a separation of *10μm* to model the probe holder, the coupling capacitance C_p is estimated at *0.088pF*. The

typical amplitude of the probe signal (v_p) was about *1.5V.* At the *881MHz*, the impedance (Z_c) due to the coupling capacitance, C_p, is about $2k\Omega$. The coupled signal (v_{cp}) at *881MHz* is thus estimated at *18mV.* This is close to the one measured experimentally and the probe-circuit coupling can be assumed to be mainly capacitive.

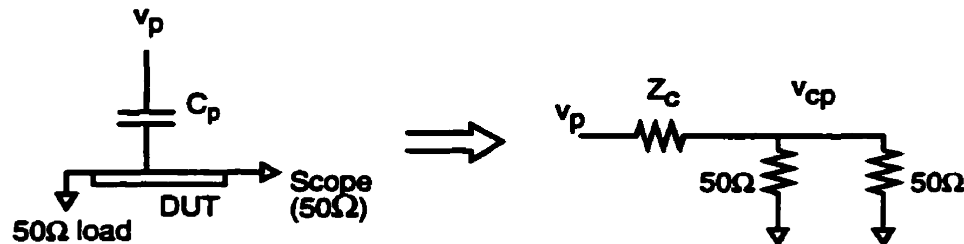

Figure 4.28: Capacitive coupling effect between a micromachined probe and a device under test. A static equivalent circuit model for the coupling effect is also given.

The probe-circuit (thru-line) interaction was also measured on a network analyzer with a set-up similar to the one shown in Figure 4.18. The forward transmission parameter (S_{21}) was measured to be *-38dB* at *0.9GHz*. For a probe signal level of *1.5V* this results in a coupled level of about *20mV* which also matches with the observed and previously modeled results. The direct coupling from the probe to the circuit can be minimised by using probing tips with a longer aspect ratio. The separation between the probe fixture and the sample can thus be increased resulting in a smaller coupling capacitance. An improved design of the probe fixture with proper ground shielding is also desirable.

The next set of measurements were performed on the TI-LNA MMIC introduced in the previous section. The gain and the return loss of the amplifier at *881MHz* were found to be *17.7dB* and *-15.6dB* respectively from Figures 4.14 and 4.15. The input and output pads were probed with the EFM instrument and the input and output signals were also measured on an oscilloscope. The results are presented in Table 5.

Table 5: Measurement on TI-LNA using I/Q Modulation.

	Input	Output	S_{21}
Oscilloscope	$54.2mV$	$415mV$	$17.6dB$
EFM	$41.5mV$ $\angle 47.3^o$	$397mV$ $\angle 36.8^o$	$19.6dB\ \angle -10.5^o$
Data sheet			$18.6dB\ \angle -33^o$

The forward transmission parameter (S_{21}) obtained from the data sheet at *900MHz* is $18.6dB\ \angle -33^o$. The discrepancy in the measurement is due to the difficulty in measuring accurately the small signal at the input of the amplifier. The errors are introduced from the coupling effect of the probe. The level of the coupled signal, measured at the output pad of the amplifier, was about $13mV$. The coupling effect is smaller here than that observed on the thru-line. This is due to the smaller dimension of the probing pad as compared to the wide interconnect line in the microstrip structure. The input signal level was increased and the EFM measurement was repeated. For $V_{input} = 83mV$, the forward transmission parameter of the amplifier was obtained as $S_{21} = 19.3dB\ \angle -15.0^o$ and with $V_{input} = 104mV$, $S_{21} = 19.2dB\ \angle -19.5^o$. The difference between the EFM S_{21} result and the specification data becomes smaller with increasing circuit signal levels. The maximum input level is however limited by the capability of the instrument to measure the amplified output signal.

The gain of the amplifier obtained from the oscilloscope measurements (17.6dB) compare well with the network analyzer result (17.7dB). In both methods the signals are measured at the external ports of the test fixture. These results are however different from the specification data due to losses and mismatch introduced by the test fixture itself. The EFM has the capability to eliminate this effect.

4.6 Mixer Modulation

A square wave modulation technique using a commercially available mixer (M1H [RELCOM]) is described in this section. In frequency mixing the received signal is applied to the R-port and a reference signal from a Local Oscillator (LO) is fed to the L-port. The intermediate frequency is derived at the I-port. A functional schematic of the M1H mixer is illustrated in Figure 4.29. The M1H is a double-balanced mixer where the L and R ports are transformer coupled while the intermediate frequency output is DC coupled. The frequency range of the high frequency signals at the L and R ports is between 1.8 to 6.2 GHz while the range at the intermediate signal at the I-port is from DC to 2GHz.

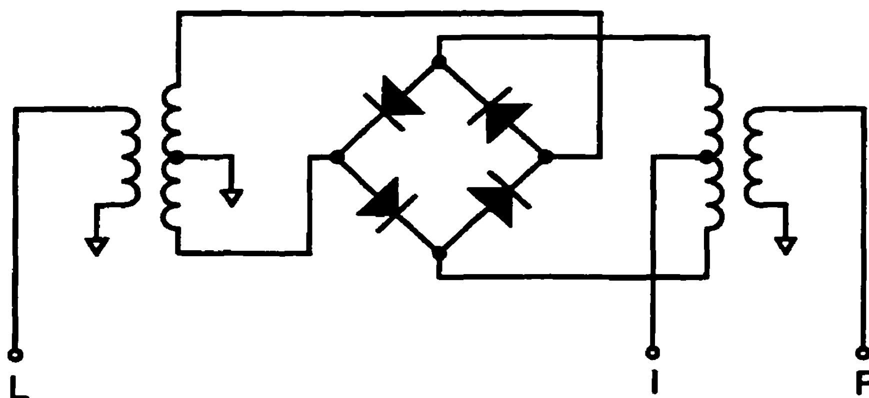

Figure 4.29: Functional schematic of M1H mixer [RELCOM].

The component is used in an amplitude modulation mode to implement the square wave modulation for vector voltage measurement. For amplitude modulation the high frequency signal is introduced at the L-port while the low frequency (usually at the probe resonance) square wave modulating signal is fed to the I-port as illustrated in Figure 4.30. The current at the I-port controls the amplitude of the high frequency carrier at the output (R-port).

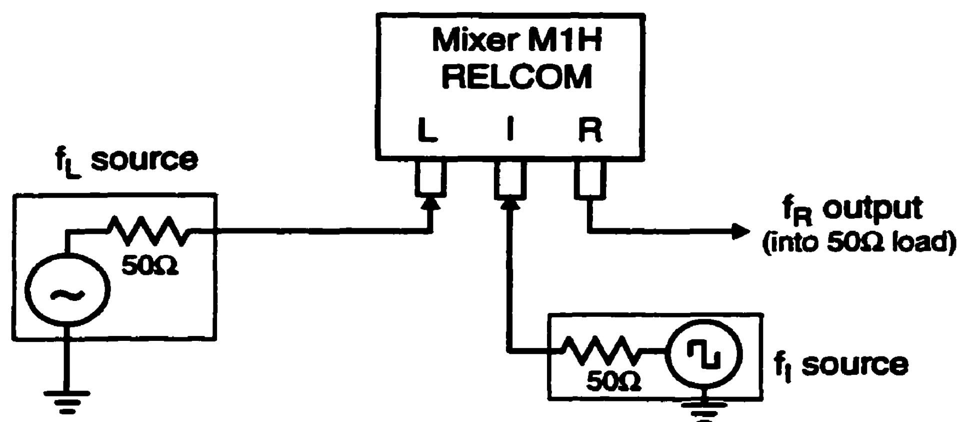

Figure 4.30: Modulator circuit for MIH mixer. A low frequency square wave signal is used to modulate the high frequency signal. The input impedance of the sources used is 50Ω.

The circuit shown in Figure 4.30 was used to test the performance of the mixer. A variable DC supply using the DS-345 signal generator was applied at the I-port. The L-port of the mixer was driven by a high frequency signal at *2GHz* obtained from an HP 8350 generator. A low-pass filter (f_c = *2GHz*) was used at the R-port to reduce higher order harmonics. The output signal was then measured using a high frequency sampling oscilloscope where the sampling head is terminated into a *50Ω* load. A *-3dBm* signal from the LO was used and the DC signal at the I-port was varied from *-0.22V* to *0.22V*. The peak-to-peak amplitude of the output signal was measured and the results are plotted in Figure 4.31.

The response of the mixer is not linear. This, however, does not prohibit the use of this mixer in the square wave modulation scheme for vector voltage measurement. Sinusoidal modulation would be impossible to implement with such a mixer. A negligible phase change of the high frequency carrier was observed as the modulating signal level (same sign) was varied. The phase of the high frequency carrier changed by 180° when the sign of the DC modulating signal was switched.

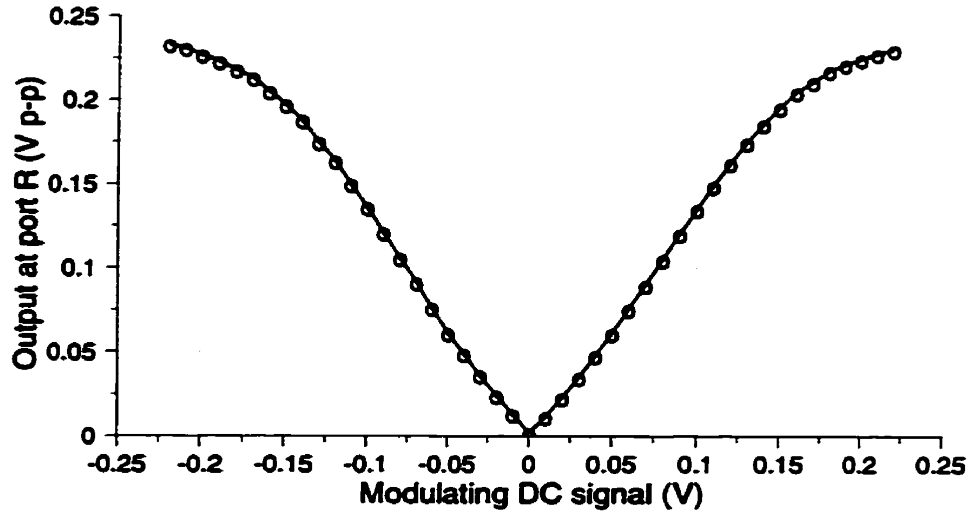

Figure 4.31: Mixer performance. The peak-to-peak amplitude of the high frequency carrier is plotted as a function of a DC modulating signal level.

The experimental-set used for heterodyne vector voltage measurement is shown in Figure 4.32. A single high frequency oscillator is used to drive the test circuit and the circuitry that generates the modulated probe signal. A DS-345 function generator supplies the modulating signal $[A_I + G_I(t)]$ at the resonant frequency of the probe to the I-port of the mixer. Due to the non-linear behaviour of the mixer, the output signal from the R-port can be written as

$$(A + G(t)) \sin (\omega_0 t + \phi_p) . \qquad [4.10]$$

The high frequency carrier is still modulated by a square wave signal but with a different amplitude and offset. This is not a major concern since a nulling technique is used for amplitude determination. For phase measurement the requirement is a constant level of modulation with $A << V_c$ and this is easily met by keeping the levels of the modulating and carrier signals constant.

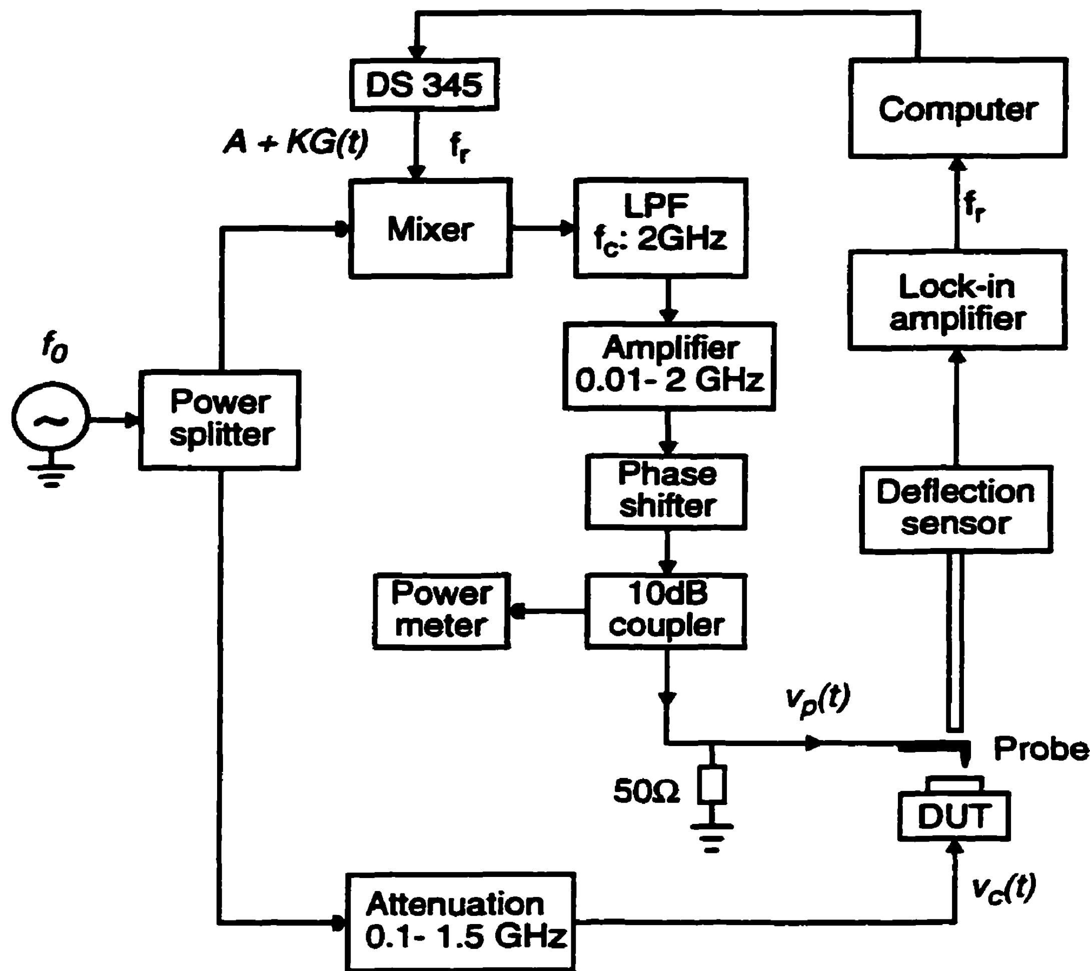

Figure 4.32: Experimental set-up for heterodyne vector voltage measurement using a mixer square wave modulation scheme.

An amplifier is used to increase the power level of the modulated probe signal which reaches a matched probe. A *10dB* coupler is used to extract the power levels of the probe signal and thus the probe parameter A. The deflection of the probe at resonance is monitored using a lock-in amplifier. The resulting data is used to operate the instrument in a feedback loop when the probe deflection is nulled for amplitude measurement of $v_c(t)$. The phase of the circuit signal is measured by manually adjusting the phase shifter and using the two null-points algorithm mentioned earlier.

4.6.1 Measurement Results

Measurement is first demonstrated on a thru-line. An operating frequency of *2GHz* was selected. While the mixer carrier bandwidth (*1.8-6.2 GHz*) allows for operation at higher frequencies, measurement bandwidth is limited by the other components in the system. A wire probe in conjunction of a fiber-interferometer deflection sensor was used in these measurements. A circuit signal with an amplitude of *171mV* was applied to the line. After the phase was set, the nulling curve shown in Figure 4.33 was obtained as the probe parameter, *A*, was varied.

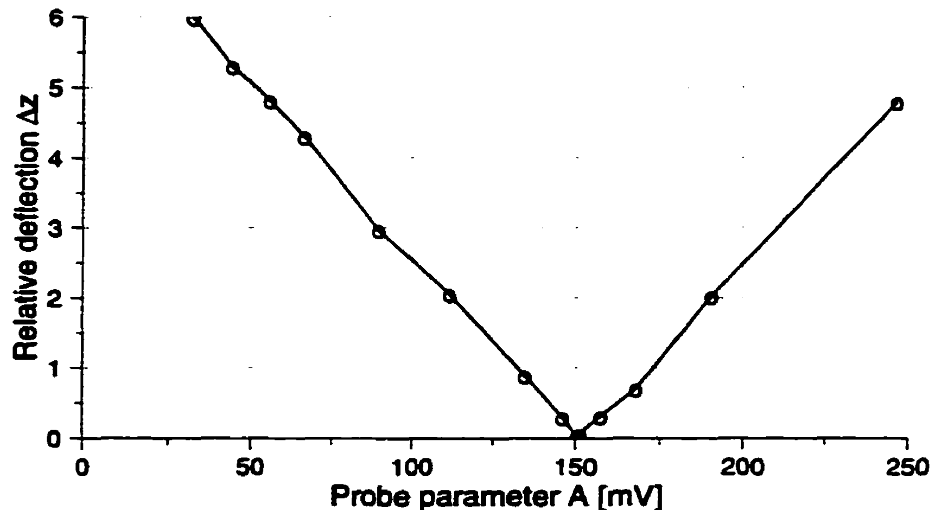

Figure 4.33: Relative deflection, Δz, of the probe as a function of the probe parameter, A, with $V_C = 171mV$ and $\phi_p = \phi_c$.

From Figure 4.33, the probe parameter, where the deflection is nulled, is measured as $A = 151mV$. Once again A is not equal to V_c probably due to probe mismatch. A calibration curve is therefore required. The probe parameter, A, was measured as a function of V_c and the results are shown in Figure 4.34. Measurement results from two experiments done at different times are shown together with a straight line fitted through the measured points. The results presented here indicate that the measurement by the instrument is repeatable. The measured data deviated from the linear calibration curve by less than *10mV*. In Figure 4.35 the measured probe deflection is plotted as a function of the probe-circuit signals

phase difference $[\phi_p - \phi_c]$. The parameter, A, was adjusted to null the deflection at $V_c = 171 mV$ as shown in Figure 4.33. The experimental results are compared with the theoretical $[1-\cos(\phi_p - \phi_c)]$ response.

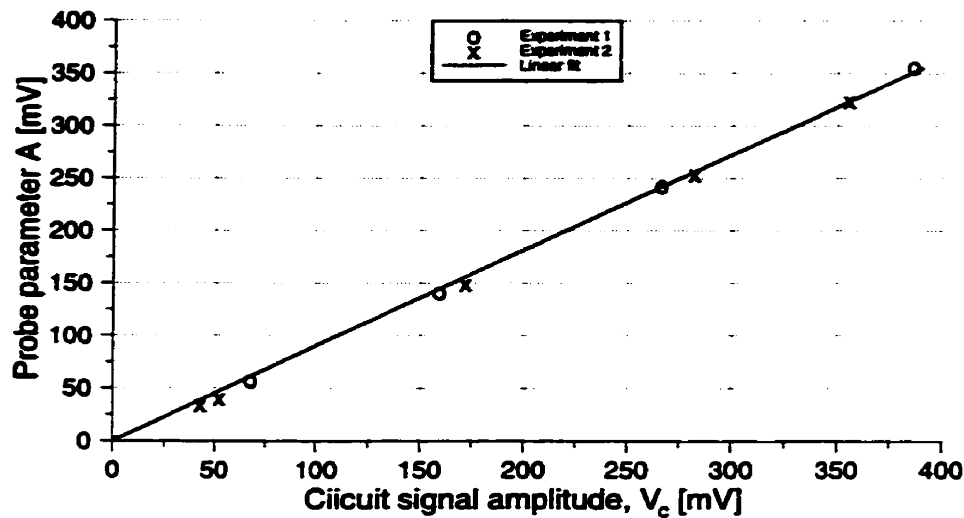

Figure 4.34: Calibration curve showing A as a function of V_c. A straight line is fitted through the results obtained from two separate experiments.

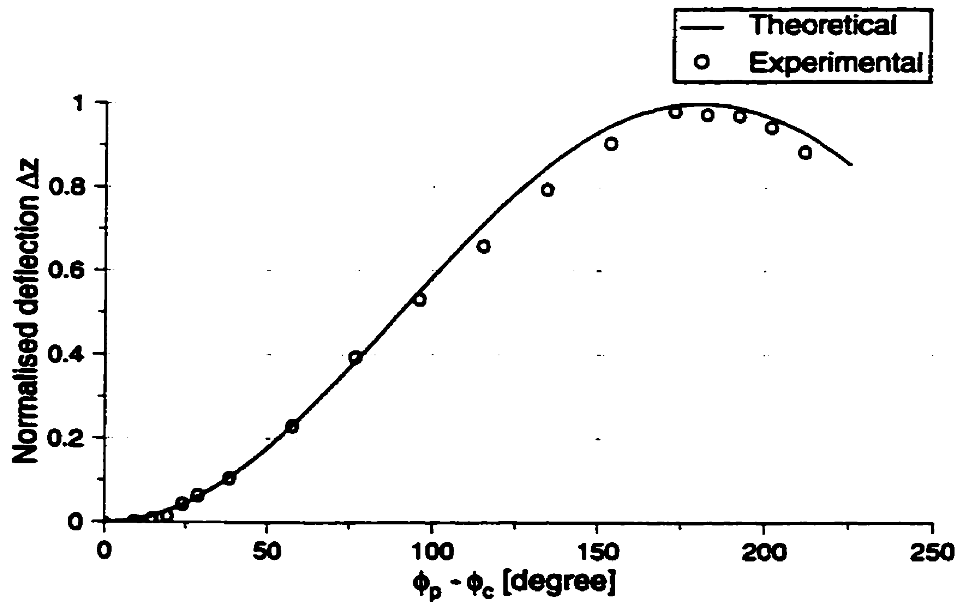

Figure 4.35: The normalised probe deflection as a function of the probe-circuit phase difference, $[\phi_p - \phi_c]$. Both the measured and theoretical results are normalised.

The next set of measurement involves the TI-LNA circuit already introduced in the previous section. The operation of the amplifier at *2GHz* was investigated by probing the internal nodes of the circuit. From Figures 4.14 and 4.15, the gain and return loss of the amplifier at *2GHz* are obtained as $S_{21} = 17.7dB$ and $S_{11} = -17.9dB$.

The amplifier was driven by a *2GHz* signal at the input and the output was monitored on a 50Ω oscilloscope. The signals at the input and output pads and the internal nodes 1 and 2, as illustrated in Figure 4.15, were probed by both the EFM instrument and the active (0.04pF) contact probe. The measurement results are tabulated in Table 6. The active (*1GHz*) contact probe was found to be usable at *2GHz*, and the probe performance was characterised by obtaining a calibration curve similar to the one shown in Figure 4.18. The results from the contact probe were then converted to circuit signal amplitude using the calibration curve.

Table 6: Vector voltage measurement on TI-LNA at *2GHz*

	Input	Node 1	Node 2	Output
EFM	$50.1\ mV$ $\angle 0^o$	$486.9\ mV$ $\angle 112^o$	$403.8\ mV$ $\angle 108^o$	$451.0\ mV$ $\angle -94^o$
Contact Probe	? $\angle ?$	$387.3\ mV$ $\angle 111^o$	$318.0\ mV$ $\angle 100^o$	$375.7\ mV$ $\angle -94^o$

The sensitivity in the phase measurement was estimated at 5°. Accurate measurement of the input signal proved to be difficult with the contact probe and the phase measurement are referenced to that of the output signal obtained by the EFM. The forward transmission parameter (S_{21}) of the TI-LNA at *2GHz* obtained from the EFM and the network analyzer measurements are compared with the specification sheet data in Table 7.

Table 7: Measurement of TI-LNA S_{21} at *2GHz*

EFM	Data sheet	Network analyzer
$19.1dB \angle -94^o$	$18.3dB \angle -77^o$	$17.7dB$

The magnitude of the S_{21} parameters shown in Table 7 compare well. The gain measured by the network analyzer is once again smaller than the specification data due to losses in the test fixture. The large discrepancy in the phase results is due to the difficulty in accurately measuring the small input signal. One source of error was the direct coupling from the probe onto the circuit. The wire probe used in these measurement was attached to a coplanar waveguide structure as opposed to the coaxial cable used in the previous measurements. The coupling level measured on the output pad of the circuit was about *15mV*. Proper shielding of the coplanar feed structure would enable a reduction of the parasitic coupling between the probe structure and the test circuit

Vector voltage measurement on a MHMIC voltage-controlled phase shifter using the mixer-based heterodyne technique is presented next. A micromachined cantilever probe was used in this measurement. The probe deflection was monitored by a beam bounce detection technique. The phase shifter is a microwave hybrid circuit fabricated on a GaAs substrate. The input and output of the phase shifter are wire bonded to microstrip lines which leads to the external ports of the packaged device. A microphotograph of the MHMIC phase shifter and its circuit schematic are shown in Figure 4.36.

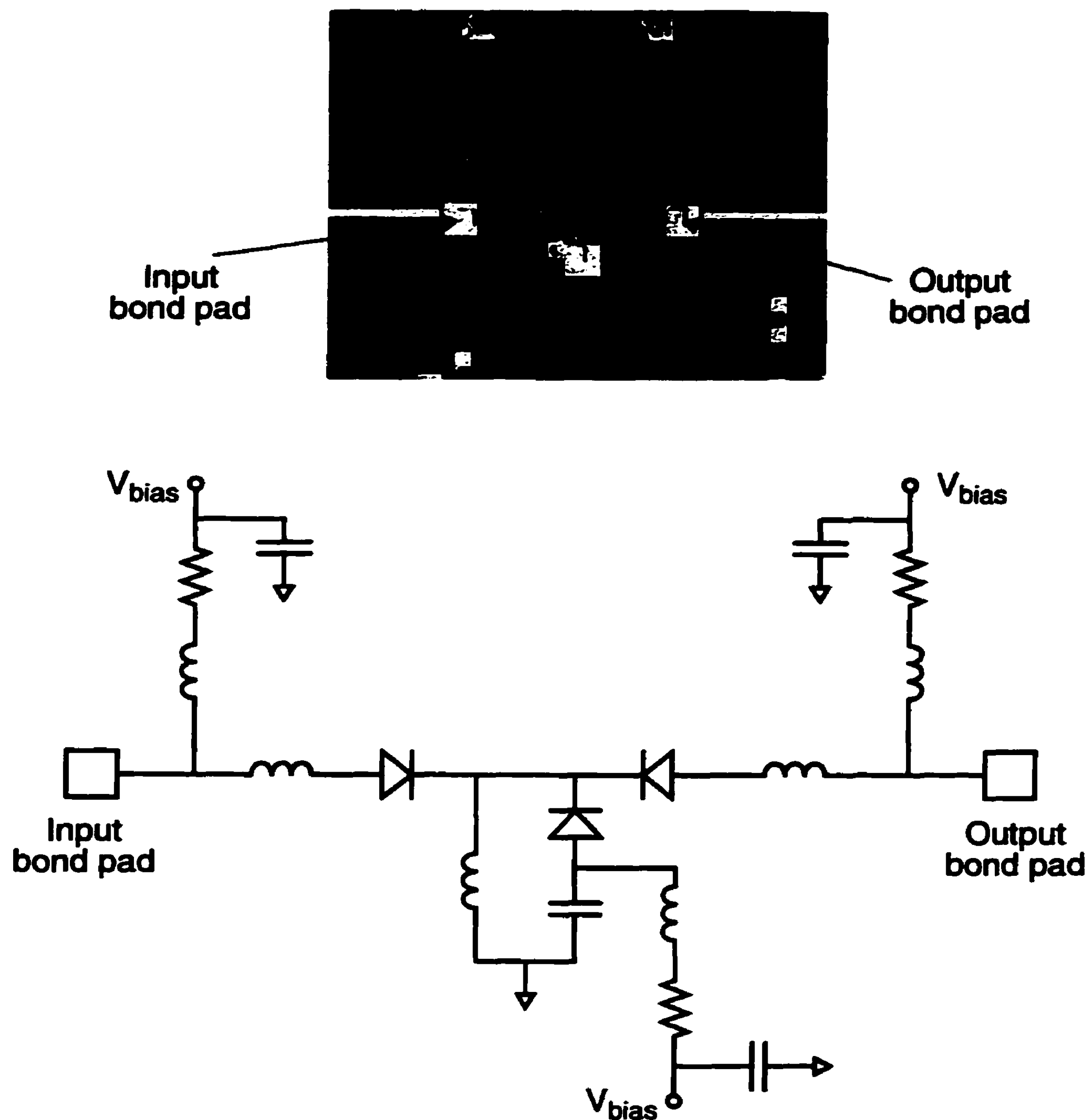

Figure 4.36: Microphotograph of the MHMIC phase shifter (top) and its circuit schematic (bottom).

The phase shifter was designed for a center frequency of *1.7GHz*. The phase change across the circuit is controlled by the bias voltage, V_{bias}. The range of V_{bias} lies between *0* and *-5 V*. The performance of the phase shifter at $V_{bias} = -2.0V$ was characterized on a network analyzer and the forward reflection and transmission parameters are shown in Figure 4.37. At *1.7GHz*, the return loss, S_{11}, was found to be *-24.1dB* while the insertion loss, S_{21}, was measured at *-4.46dB*.

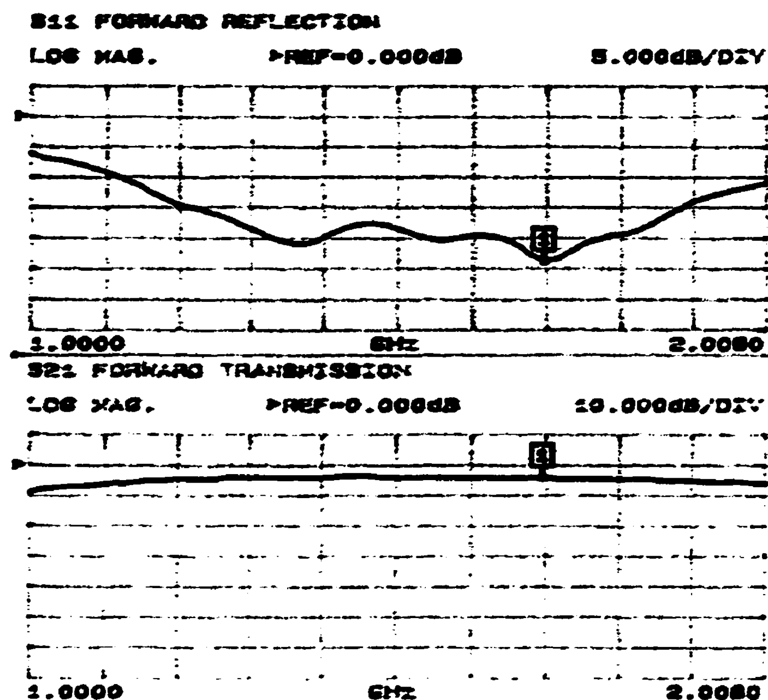

Figure 4.37: The forward reflection and transmission parameters S_{11} (top) and S_{21} (bottom) of the phase shifter with $V_{bias} = -2.0V$.

Table 8 shows the S_{11} and S_{21} parameters of the phase shifter as a function of the bias voltage measured at *1.7GHz* on a network analyzer. These results are reproduced from the specification sheet that came with the device [CRC2]. The relative phase shift introduced by the circuit is also shown in Table 8 with the result for a $V_{bias} = 0.0V$ used as the reference. The circuit is well matched at higher (magnitude) bias voltages as indicated by the smaller S_{11}.

Table 8: S-parameters of the phase shifter at *1.7GHz*.

Bias voltage (*V*)	S_{11} (mag.) *dB*	S_{21}	Rel. phase shift
0.0	-7.27	$-6.63dB \angle 79.5^o$	0.0°
-0.25	-10.0	$-6.25dB \angle 95.6^o$	16.1°
-0.5	-12.8	$-5.52dB \angle 108.0^o$	28.5°

Bias voltage (*V*)	S_{11} (mag.) *dB*	S_{21}	Rel. phase shift
-0.75	-15.7	$-5.08dB\ \angle 118.1^o$	38.6°
-1.0	-18.7	$-4.82dB\ \angle 126.6^o$	47.1°
-2.0	-25.5	$-4.41dB\ \angle 150.0^o$	70.5°
-3.0	-19.9	$-4.43dB\ \angle 165.0^0$	85.5°
-4.0	-16.6	$-4.33dB\ \angle -178.1^o$	102.4°
-5.0	-14.8	$-4.39dB\ \angle -172.1^o$	108.4°

The carrier frequency range of the M1H mixer is specified as *1.8-6.2 GHz*. However the mixer component was found to be usable at *1.7GHz* and the heterodyne technique was used for vector voltage measurement on the phase shifter circuit at that frequency. An input signal ($V_c = 0.3V$) was applied to the input of the circuit and the output port was measured on *50Ω* oscilloscope channel. Both the input and the output bond pads, indicated in Figure 4.36, were probed using the EFM and the contact active probe. The ratio of the output voltage to the input voltage (in *dB*) and the phase shift across the device were computed as ($20log(V_{out}/V_{in})$) and (ϕ_{out}-ϕ_{in}) respectively. The results obtained for different bias voltages are presented in Table 9.

Table 9: EFM and contact probing results at *1.7GHz*

V_{bias} (V)	EFM $20log(V_{out}/V_{in})$, $\phi_{out}-\phi_{in}$	Contact probe $20log(V_{out}/V_{in})$, $\phi_{out}-\phi_{in}$
0.0	$-10.21dB\ \angle -176.4^o$	$-11.31dB\ \angle -178.2^o$
-0.25	$-8.24dB\ \angle -158.1^o$	$-9.17dB\ \angle -158.0^o$
-0.5	$-6.83B\ \angle -139.6^o$	$-8.20dB\ \angle -143.3^o$
-0.75	$-6.28dB\ \angle -129.4^o$	$-7.52dB\ \angle -130.4^o$

V_{bias} (V)	EFM $20log(V_{out}/V_{in})$, ϕ_{out}-ϕ_{in}	Contact probe $20log(V_{out}/V_{in})$, ϕ_{out}-ϕ_{in}
-1.0	$-5.85dB \angle -116.7^o$	$-7.19dB \angle -117.5^o$
-2.0	$-5.22dB \angle -85.6^o$	$-6.55dB \angle -88.1^o$
-3.0	$-4.60dB \angle -64.4^0$	$-5.84dB \angle -65.5^0$
-4.0	$-4.71dB \angle -48.5^o$	$-5.54dB \angle -52.6^o$
-5.0	$-4.95dB \angle -36.1^o$	$-5.40dB \angle -38.3^o$

A good agreement is observed between the measurement results obtained from the EFM and the contact probe. However, the results do not compare well with the network analyzer measurements shown in Table 8 especially for small magnitudes of V_{bias}. The main reason for the difference is the poor return loss of the circuit at these bias voltages. The ratio V_{out}/V_{in} is equivalent to S_{21} only for a proper match (small S_{11}). The direct coupling of the probe to the test point (in the range of *10-15 mV*) is another source of error when measuring the smaller signals at the output of the circuit. The relative phase shift ($\Delta\phi$) from the probing results are calculated for higher bias voltages and compared with the network analyzer measurement in Table 10. The result for $V_{bias} = -3.0$ is used as the reference in these calculations.

Table 10: Comparison of the relative phase shift ($\Delta\phi$) at *1.7GHz*

V_{bias} (V)	$\Delta\phi$ (EFM)	$\Delta\phi$ (Contact probe)	$\Delta\phi$ (Network analyzer)
-1.0	33.2^o	32.9^o	47.1^o
-2.0	64.3^o	62.3^o	70.5^o
-3.0	85.5^o	85.5^o	85.5^o
-4.0	101.4^o	97.9^o	102.4^o
-5.0	113.8^o	112.1^o	108.4^o

A good agreement between the results is observed for V_{bias}<-2.0 V. In both the EFM and the contact probe measurements, the probe was positioned over one test point and the measurements for different bias voltages were performed. With the probe over the input pad V_{bias} was varied from *0.0* to *-5.0V*. The probe was then placed over the output test pad and V_{bias} was changed from *-5.0* to *0.0V*. A drift in the performance of the phase shifter with time could be a reason for a better comparison observed around V_{bias} = *-5.0V*.

In this chapter, heterodyne vector voltage measurements were demonstrated using three different modulation techniques. Although better results were obtained using the double-path modulation scheme it should be noted that a non-invasive probe was used in those experiments. The concept behind the double-path modulation technique is simple, but the experimental implementation of this technique results in a complicated measurement system. Thus the I/Q modulation technique was investigated with the goal to simplify the measurement system. This technique has the capability of providing automated vector measurements. The main drawback of this method was the narrow bandwidth of the I/Q modulator used. Wider bandwidth I/Q modulators are available but they are much more expensive. The heterodyne technique was also implemented using a mixer modulation scheme in order to extend the bandwidth of the measurement system. Here, the mixer enabled only amplitude modulation of the high frequency signals. Thus, an external phase shifter was required resulting in a slightly more complex measurement set-up.

Chapter 5

Pulse Sampled Waveform Measurement

So far all the results presented have dealt with the measurement of sinusoidal signals. In this chapter a pulse sampling technique that allows measurements of arbitrary, periodic waveforms is introduced. This is incorporated with the previously discussed heterodyne technique and enables for the measurement of high frequency waveforms. Measurement of digital signals at internal nodes of an integrated circuit is also demonstrated.

5.1 Measurement Technique

The use of a sinusoidal probe signal enabled vector voltage measurement as demonstrated in the previous chapter. For arbitrary waveform measurement a pulse excitation is used as the probe signal and a sampling technique is utilized [Bridges 94]. An example of an arbitrary but periodic signal $v_c(t)$ is shown in Figure 5.1(a). The test circuit signal $v_c(t)$ could be either a digital or analog waveform. The sampling signal $v_s(t)=G_\delta(t-\tau)$ is a narrow pulse train as shown in Figure 5.1(b) that repeats itself at the same rate as the circuit signal $v_c(t)$. In Figure 5.1(b) δ is the pulse width and τ is an adjustable time delay. The block diagram of the instrument used is shown in Figure 5.2. Similar to conventional testing methodology, a specified test pattern from the generator repeatedly excites the test circuit at its external ports. A photograph of an actual circuit is shown with the probe positioned over a test point of interest. In all the measurements in this section a microfabricated probe was used in conjunction with a beam bounce deflection system. A pulse generator which is synchronised with the test pattern generator outputs a high frequency

sampling signal $v_s(t)$ which can then be delayed in time. A heterodyne technique is again employed to enable the measurement of signals whose frequency components are much higher than the probe resonance frequency f_r [Said 96]. The sampling signal is thus modulated at the resonant frequency, f_r so that the signal sent to the probe is represented by

$$v_p(t) = v_s(t)\cos(2\pi f_r t)\ . \qquad [5.1]$$

Expansion of the force equation [3.23] yields several high frequency terms, a dc term and terms at f_r and $2f_r$. The probe does not respond to the high frequency terms and a static deflection is obtained from the dc term. Since the probe deflection is enhanced at f_r by its quality factor, only that component of the force is monitored using a lock-in amplifier. The deflection at f_r is formulated as

$$\Delta z|_{f_r} = \frac{\partial}{\partial z}C(x,y,z)\frac{Q}{k}[-\langle v_s(t), v_c(x,y,t)\rangle + \Delta\Phi\langle v_s(t)\rangle]\cos(2\pi f_r t)\ . \qquad [5.2]$$

$$\langle a(t), b(t)\rangle = \frac{1}{T}\int_0^T a(t)b(t)dt \quad , \quad \langle a(t)\rangle = \frac{1}{T}\int_0^T a(t)dt$$

In [5.2] $<,>$ denotes the inner product of the two signals and $< >$ denotes the average over a time period T. Q is the quality factor of the beam and k is its spring constant. The $\Delta\Phi$ term is due mainly to surface charging effect and has a very low frequency response (*mHz*). Thus, the term $\Delta\Phi<v_s(t)>$ is constant for any one measurement and it only adds a DC offset to the measured result. Since the intent here is to measure waveshapes of internal signals rather than absolute voltage levels the DC term is dropped from now on to simplify the discussion. If an ideal sampling pulse is considered, in other words a pulse that has infinitely small rise and fall times and whose width δ is much smaller than the repetition time period $T = 1/f_b$, then the deflection at f_r is proportional to $v_c(t=\tau)$ and is given by

$$\Delta z|_{f_r} = \left[-\frac{\partial C}{\partial z}\frac{Q}{k}\frac{\delta}{T}\cos\left(2\pi f_r t\right)\right] \bullet v_c(x,y,t=\tau)\ . \qquad [5.3]$$

Thus the voltage on the circuit can be sampled at one point in time corresponding to the position τ of the sampling pulse. If the pulse is scanned over the entire period by varying τ from 0 to T the entire waveshape of the test signal can be extracted. This technique is analogous to a sampling oscilloscope except that we can measure signals at internal nodes

of a circuit while an oscilloscope can only access the external ports.

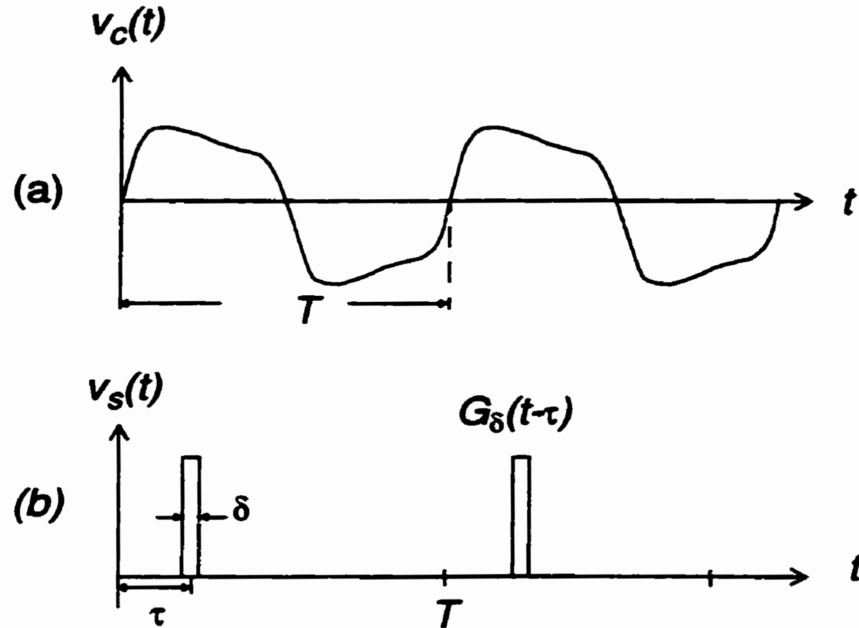

Figure 5.1: (a) Example of a periodic voltage waveform $v_C(t)$ to be measured, (b) sampling signal $v_S(t)$ with same periodicity as $v_C(t)$. Here $v_S(t)$ is sampling the test signal $v_C(t)$ at the instant $t = \tau$.

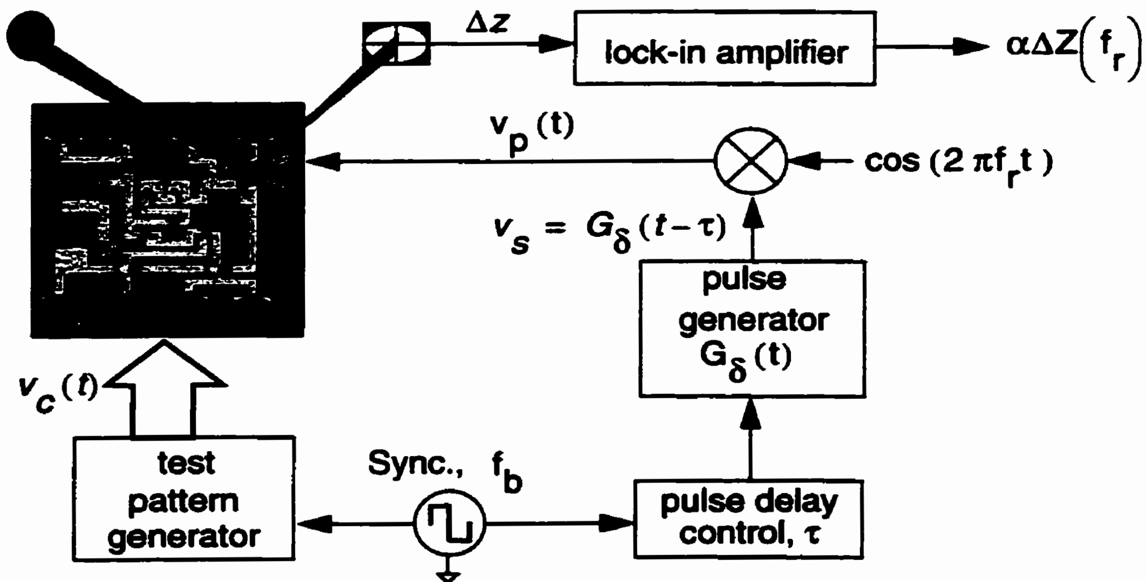

Figure 5.2: Block diagram of the pulse sampling technique. A photograph of a test circuit is shown with the EFM probe positioned over a test point of interest.

The measured signal from the deflection of the probe is a convolution between the repetitive sampling signal and the test circuit signal. The result from this technique is a signal which is proportional to the test circuit waveform if calibration to account for the other parameters in [5.3] is omitted. Accurate positioning of the probe is also unnecessary. This, nevertheless, enables the investigation of such features as propagation delay and rise and fall times of internal signals of a circuit. Ringing effects can also be observed from the waveshapes of the signals.

Absolute voltage measurement is possible without any calibration step or accurate probe positioning by using a heterodyne/nulling technique [Bridges 95]. In this method the sampling signal is modulated as $v_p(t) = [A + K\cos(2\pi f_r t)]*v_s(t)$ with A and K being some adjustable parameters. The deflection of the probe at the resonant frequency f_r is now given by

$$\Delta z|_{f_r} = \frac{\partial}{\partial z}C(x, y, z)\frac{Q}{k}[A\langle v_s(t), v_s(t)\rangle - \langle v_s(t), v_c(x, y, t)\rangle + \Delta\Phi\langle v_s(t)\rangle]\,K\cos(2\pi f_r t)\,. \quad [5.4]$$

In the case of an ideal sampling pulse the deflection becomes

$$\Delta z|_{f_r} \approx \frac{\partial}{\partial z}C(x, y, z)\frac{Q\delta}{kT}[A - v_c(x, y, t = \tau) + \Delta\Phi]\,K\cos(2\pi f_r t)\,. \quad [5.5]$$

By varying the parameter A until the deflection is nulled the voltage level at $t = \tau$ can be determined as $v_c(x, y, t = \tau) = A + \Delta\Phi$. The $\Delta\Phi$ term can be estimated by nulling the probe deflection for $v_c(t) = 0$. The measured result is independent of $C(x,y,z)$ implying that precise information about the probe position over the test point is not required and that measurement over passivated structures is possible. This technique, however, comes with the penalty that more complex and expensive electronics are required for the implementation of the modulation scheme especially at high frequencies. The experimental set-up used to implement the heterodyne sampling technique, shown in Figure 5.2, and the results from the measurements of digital waveforms are presented in the following sections.

5.2 Experimental Set-Up

The generation of the test vector and the sampling signal is a major part of the instrument and can prove to be quite difficult especially at high frequencies. In our experimental set-up a multi-channel data generator (HP80000) from Hewlett-Packard is used. Some details about the specifications of the data generator is presented in Table 11 [HP]. The HP 80000 has the capability of generating data patterns with a maximum rate of 1 Gb/s.

Table 11: HP 80000 Data Generator System.

Frequency Range	100 MHz - 1 GHz
Transition Time	< 150 ps (10%-90%)
Jitter	< 10 ps
Delay (range)	±2 ns
Delay (resolution)	2 ps

A block diagram of the experimental set-up used for the generation of the test circuit signal and the high frequency sampling pulse is shown in Figure 5.3. The first two channels of the HP80000 provide the trigger to an oscilloscope as well as the repetitive test vector ($v_c(t)$) that drives the DUT. The third and fourth channels are used to drive the electronics that generates the probe high frequency sampling signal $v_p(t)$.

A pulse-shaped signal ($v_s(t)$) from the third channel of the generator is fed to a switch that is turned on and off at the resonant frequency of the cantilever probe. The signal is thus modulated by a square wave signal whose first harmonic is at the probe resonant frequency f_r. The modulated signal then drives a transmission line bandpass filter which generates high frequency pulses from the rising and falling edges of $v_s(t)$. By using a control signal $v_{cont}(t)$ with an adjustable time delay, the second switch is used to turn off one of the two pulses generated by the filter. The width of the sampling pulses can be further reduced by choosing an appropriate pattern for $v_{cont}(t)$ and adjusting the delay between $v_{cont}(t)$ and $v_s(t)$ to turn the high bandwidth switch ON for a very short duration.

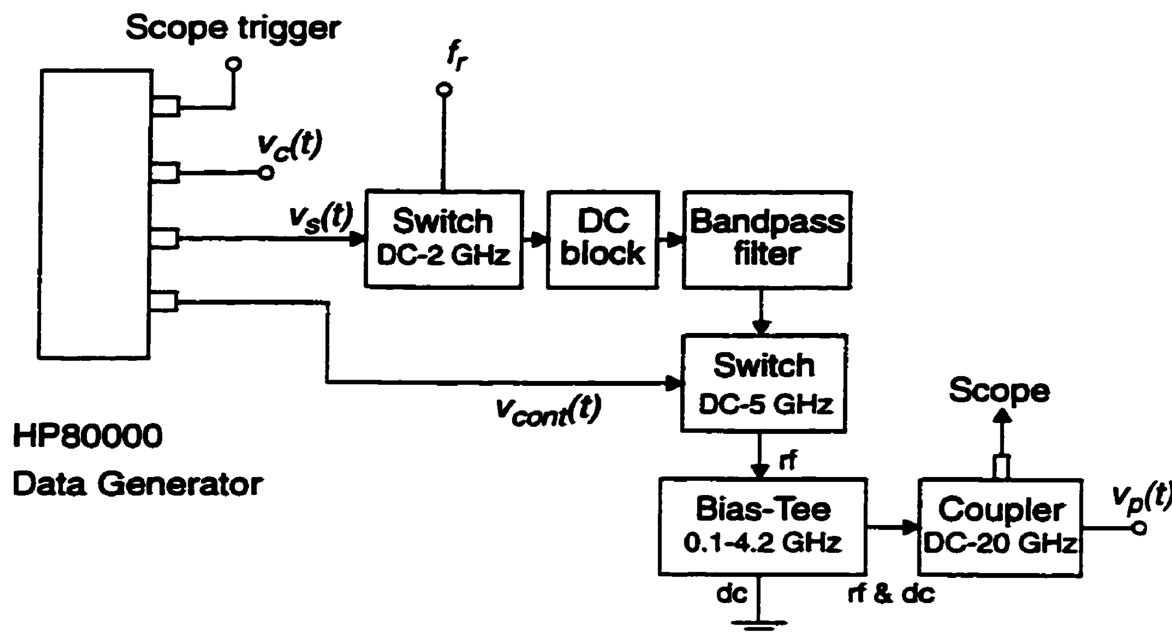

Figure 5.3: Generation of the test circuit ($v_c(t)$) and probe pulse sampling ($v_p(t)$) signals.

Since the coupling capacitance between the probe and the test circuit is small, the probe can be considered as an open circuit and the signal $v_p(t)$ is reflected back. The reflected pulse is absorbed by the high bandwidth switch by varying the path length between the probe and the switch and selecting an appropriate time delay. The shape of the sampling pulses could be monitored on an oscilloscope by using a 10:1 coaxial coupler which enabled the optimization of the various parameters. The DC block and the Bias-Tee were added to protect the instruments used in the system.

An example of a sampling pulse waveform generated by this technique is shown in Figure 5.4. The pulse width at half magnitude is about *250ps* and the peak value of the pulse is about *600mV.* Some non-idealities are also present in the sampling signal since the generation of these pulses using simple, inexpensive electronics is not a simple task at high frequencies. The signals from all four channels of the generator are synchronized and can be delayed with respect to each other with a minimum resolution of *2ps*. This enables the implementation of the adjustable time delay feature in the sampling technique by programming the instrument. Thus the generation of the test vector and the sampling signal is

controlled by a computer which is also used to collect the probe deflection data at f_r from the lock-in amplifier through an analog-to-digital converter.

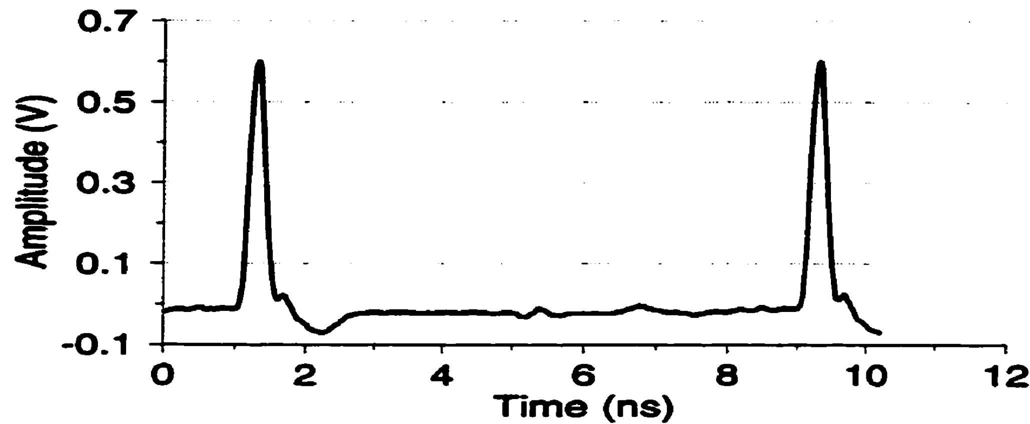

Figure 5.4: Sampling pulse waveform $v_p(t)$ with a repetition frequency of *125MHz* as captured on an oscilloscope. Some non-idealities in $v_p(t)$ are present. The FWHM of the pulse is estimated at *250ps*.

5.3 Measurement on a Microstrip Interconnect

To demonstrate the technique a 16-bit digital pattern [1010100110010101] at 125Mb/s was measured on a printed circuit microstrip interconnect. The high logic level was set at *1.0V* and the low logic level at *-1.0V*. The microstrip interconnect used was a feedthrough line and Figure 5.5(a) shows the signal on the line $v_c(x,y,t)$, that was directly measured by an oscilloscope. The modulated sampling pulse is applied to the probe and as it is shifted in time from *0* to *128 ns* the entire 16-bit test pattern was measured. The waveform was sampled in increments of 200 ps and the results are shown in Figure 5.5(b). The vertical axis is not labelled since this technique does not measure absolute voltage levels. The EFM probe was positioned approximately *1μm* over the test point. The coupling from the probe tip to the test circuit at this distance was measured to be less than *10mV*.

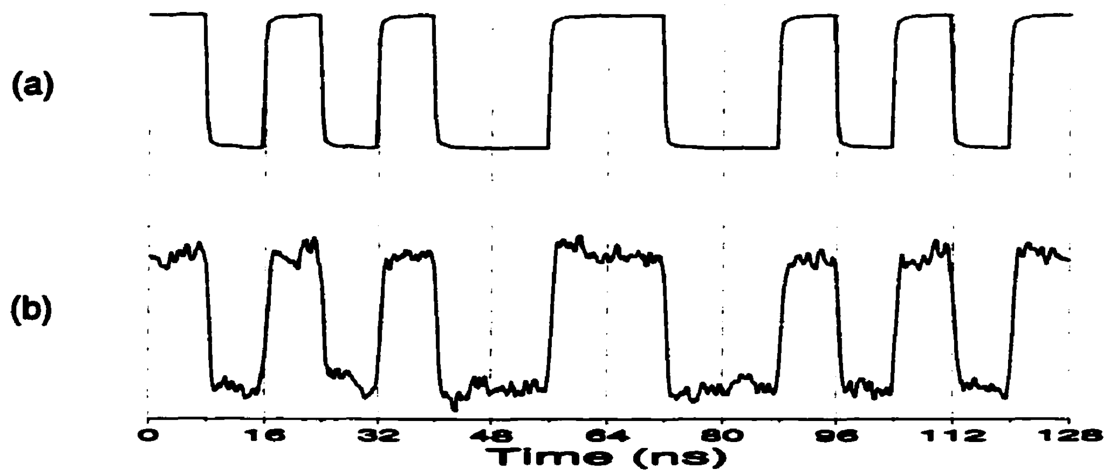

Figure 5.5: Measurement on a microstrip interconnect line at 125 Mb/s; (a) Applied digital pattern from generator measured on a oscilloscope (1010100110010101), (b) waveform measured using EFM.

Measurement results at higher bit rates are presented next. An 8 bit pattern at 1 Gb/s (01011001) was measured on the microstrip interconnect and the results are shown in Figure 5.6. The logic levels of $v_c(t)$ switched from *-1.0V* to *+1.0V*. In this case the sampling pulse was shifted in increments of 100ps.

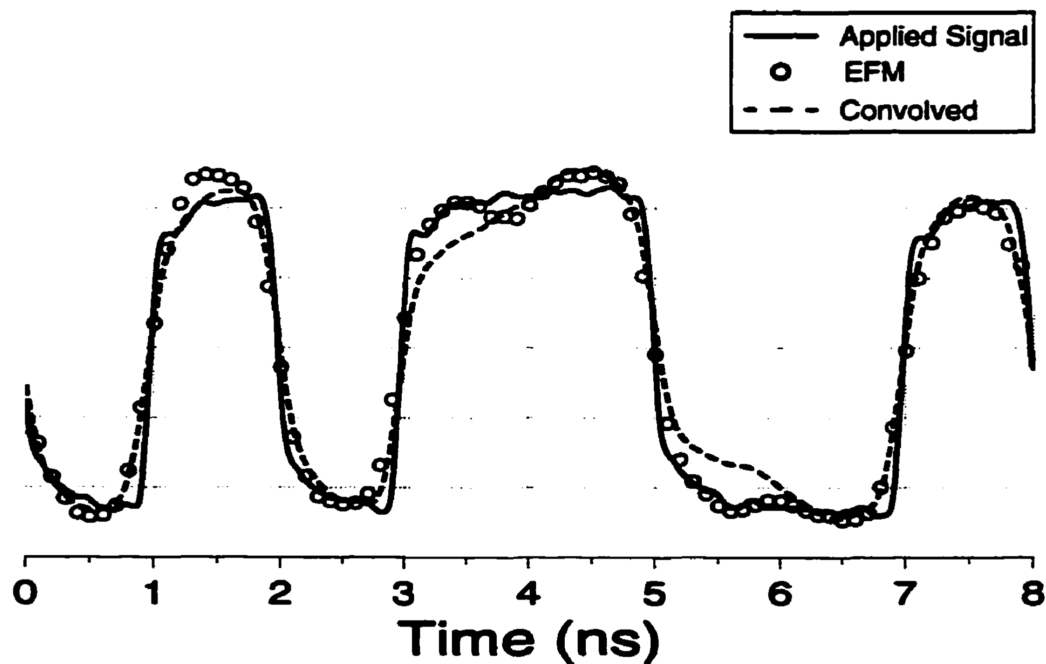

Figure 5.6: Measurement on a microstrip interconnect line at 1 Gb/s; the applied digital pattern $v_c(t)$ (01011001), the EFM result and convolution of $v_c(t)$ with $v_s(t)$ are shown.

The labelling on the vertical axis is once again omitted since absolute voltages are not being measured and the results shown are normalised for comparison purposes. The data obtained from the EFM instrument is processed by a three point smoothing routine to reduce the noise in the measurement and they are shown by the circles in Figure 5.6. The EFM result is compared to the test pattern $v_c(t)$ applied to the circuit as well as the expected result obtained from convolving the digital pattern $v_c(t)$ with the sampling signal $v_s(t)$ (shown in Figure 5.4). A good agreement is obtained between the EFM and the convolved result but they do deviate at some points over the waveform. This is primarily due to some ringing effects in the signal applied to the probe $v_p(t)$. Complete characterization of these effects is difficult. The rise and fall times of the measured result are not identical to those of the test signal on the line due to the finite width of the sampling pulse and the presence of other non-idealities as was shown in Figure 5.4. Figure 5.7 shows a zoomed-in section of the results presented in Figure 5.6. The rise time(10-90%) of the applied signal is 180 ps while those measured from EFM and the convolution results are both estimated to be about 380 ps. There is a very close agreement between these results.

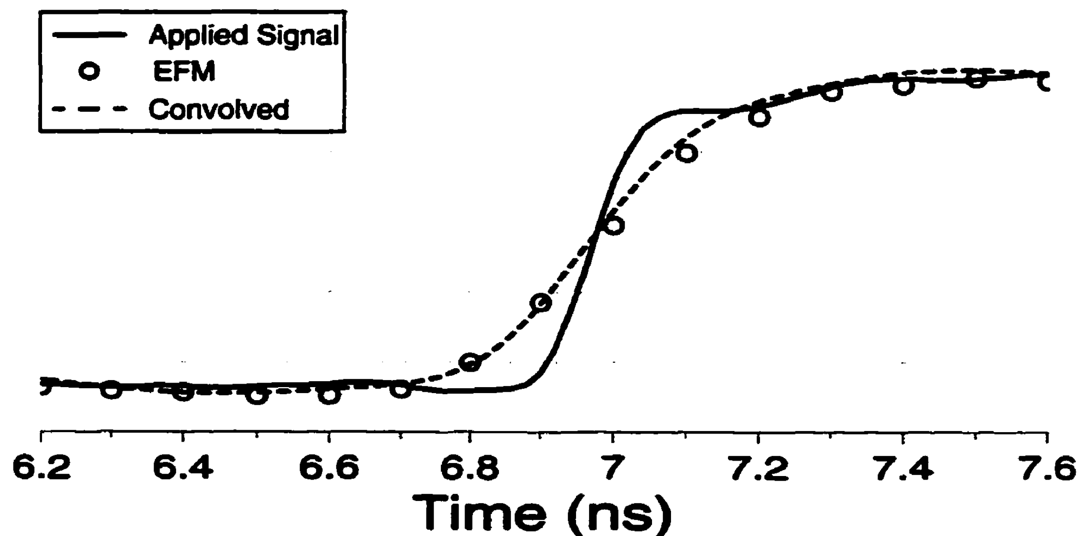

Figure 5.7: Measurement on a microstrip interconnect line at 1 Gb/s (Enlarged view of a rising edge); Rise time of applied pattern ~ 180 ps compared with rise times of measured waveform and convolved result (~380 ps).

Finally, a 16 bit pattern (0011001010111100) at 1 Gb/s was investigated as shown in Figure 5.8. Both the applied pattern and the signal measured by the EFM instrument are shown. The sampling pulse was shifted in increments of *100ps* and the data obtained were subjected to a three point smoothing procedure. These results indicate that arbitrary digital waveforms at bit rates up to 1 Gb/s can be measured. Measurement of longer bit patterns however results in a smaller signal-to-noise ratio. While a feedthrough line is not a typical circuit where this technique would be utilized it serves the purpose of verifying the principle behind this instrument.

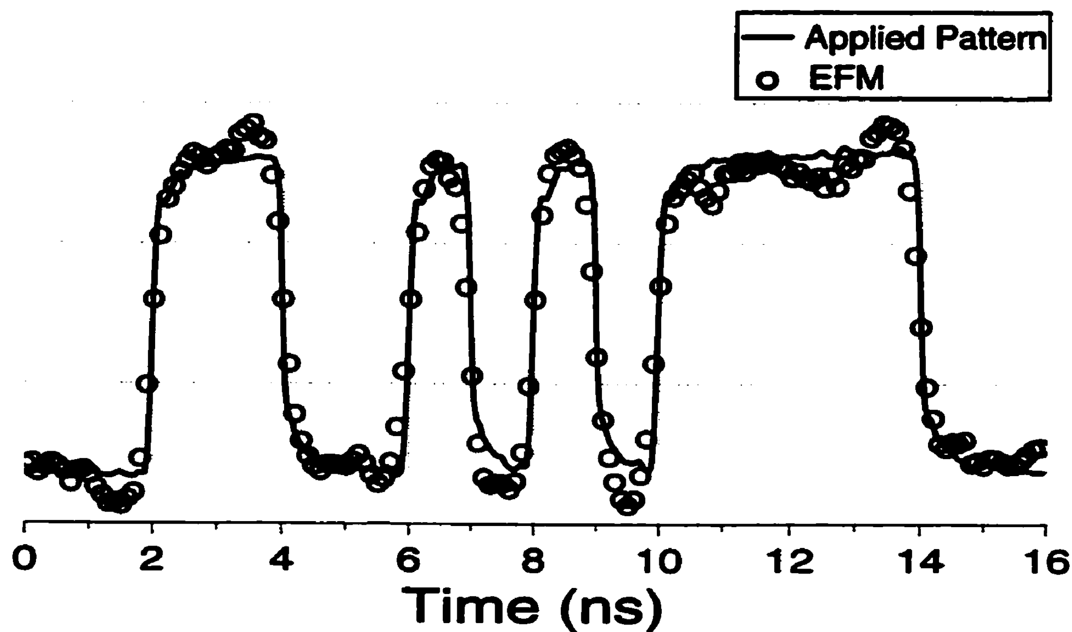

Figure 5.8: Measurement on a microstrip interconnect line at 1 Gb/s; (a) Applied digital pattern $v_C(t)$ (0011001010111100), (b) waveform measured using EFM (3 point smoothing).

5.4 Measurement on a BiCMOS Integrated Circuit

The measurement results presented in this section were made on a digital circuit fabricated in Nortel's 0.8 μm BiCMOS technology [Noruttun 97]. The test circuit used here is a chain of CMOS inverters as shown in Figure 5.9 and it provides a more appropriate

application of the instrument being developed. The inverters selected in the design of this circuit were of the minimum size available from the BiCMOS library. The gate width of the p-channel FET was specified as *11.8μm* and that of the n-channel FET as *8.8μm*. The small 20x20 μm probe pads were added to each stage to enable measurement with an active contact probe. The signals at the internal test pads were measured. These pads are typically not required for our EFM instrument.

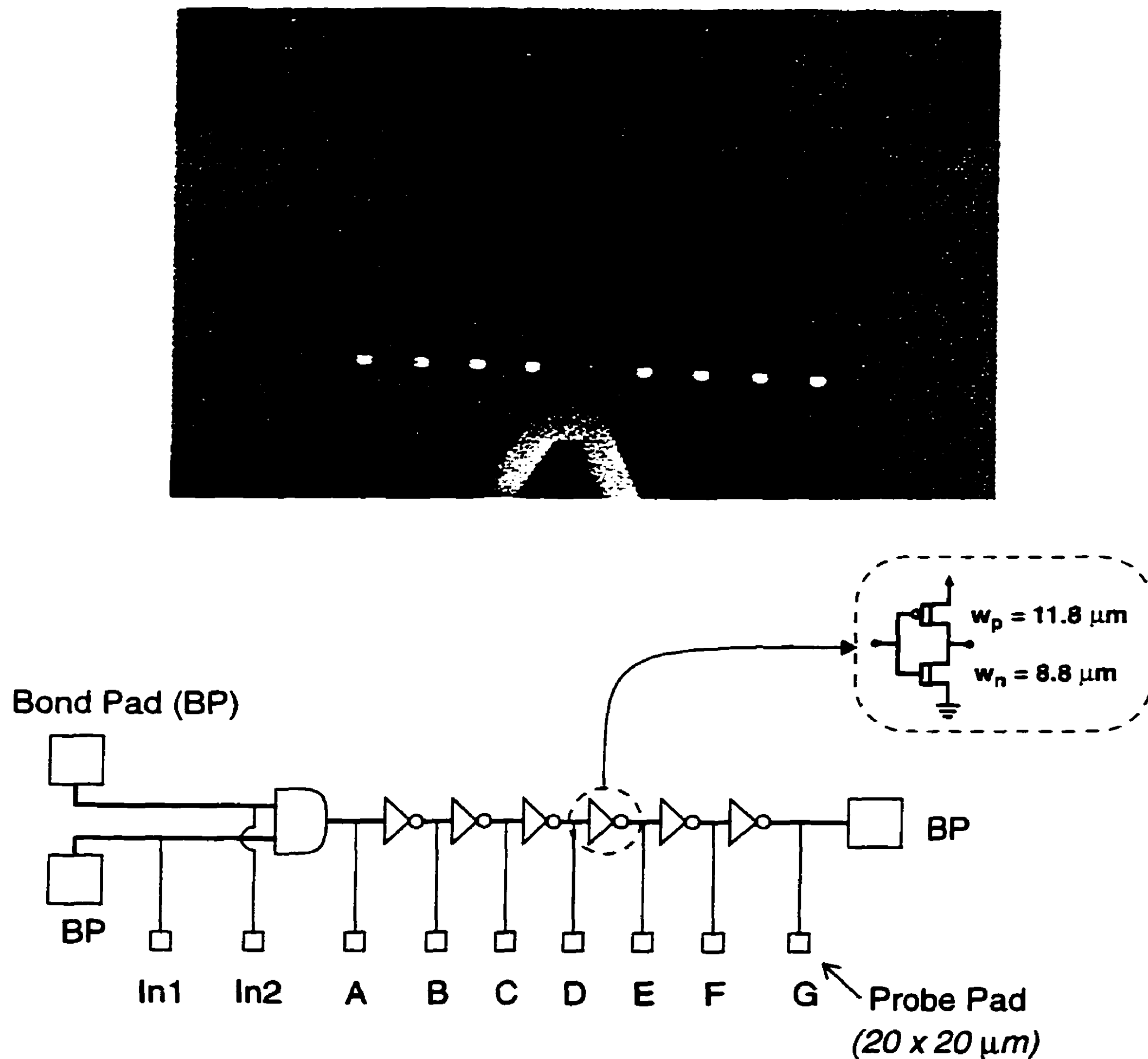

Figure 5.9: Microphotograph of Nortel BiCMOS inverter chain showing EFM probe. The circuit schematic is at the bottom with the inset showing the structure of the CMOS inverters.

The circuit was driven by applying an 8 bit digital pattern (01100101) at 1Gb/s to one of the input (In1) of the AND gate in the test circuit (shown in Figure 5.9). The other input

(In2) was kept at *+5.0V*. The waveforms at test pads A, C and D were measured using the EFM and an active *0.04 pF* contact probe (*1GHz* bandwidth). The results are presented in Figure 5.10.

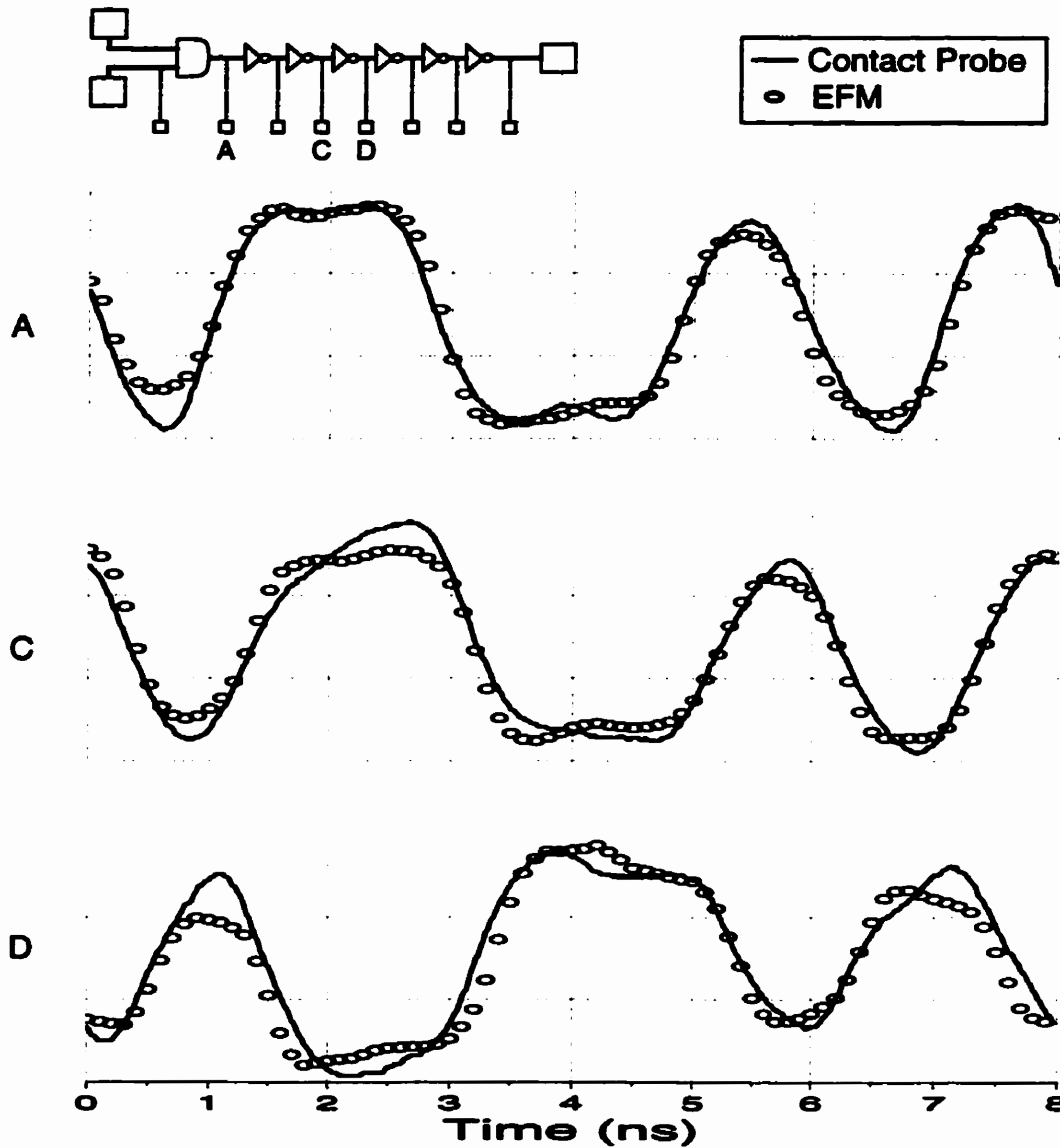

Figure 5.10: Measurement of an 8-bit 1 Gb/s digital pattern (01100101) at test pads A, C and D. Results from active contact probing and EFM (non-contact) probing are presented for each test point.

The measured signals are once again normalised for comparison purposes and a 3 point smoothing was applied to the EFM data for noise reduction. The EFM results are indicated by the circles and the waveforms are sampled every *100ps* over the entire 8-bit pattern. The logic levels can be easily distinguished and the measured signals from the two techniques compare well. The waveform measured at test pad D is an inverted and slightly delayed version of the one measured at test pad C as expected from the circuit. During these measurements surface charging of the test circuit was observed and care was taken to overcome these effects. The circuit was excited by the test pattern for a few minutes to allow it to charge up and reach steady state before any measurement was undertaken.

The BiCMOS circuit was next driven by a square wave signal at 0.5Gb/s. The signal waveform at test pad A, obtained from circuit simulation using Cadence SpectreS, is shown in Figure 5.11(a). The signal at pad A was probed using the EFM instrument with samples taken after every *100ps*. The measured result after a three point smoothing procedure is shown in Figure 5.11(b). Also shown in Figure 5.11(b) is the waveform that is expected from measurement which is obtained by convolving the simulated waveform in Figure 5.11(a) with the sampling pulse shown in Figure 5.4. The results are normalised for comparison purposes and they show good agreement.

The 28-80% rise time of the simulated waveform is obtained as *230ps* while the fall time is measured at *180ps*. The difference is attributed to the asymmetric gate widths of the p-channel and n-channel devices in the CMOS inverters. The 20-80% rise time of both the EFM and the convolved results are estimated at *370ps*. The test pad was also probed with the *0.04pF* active probe and the measured waveform is presented in Figure 5.11(c). The loading effect of the contact probe is evident in this measurement.

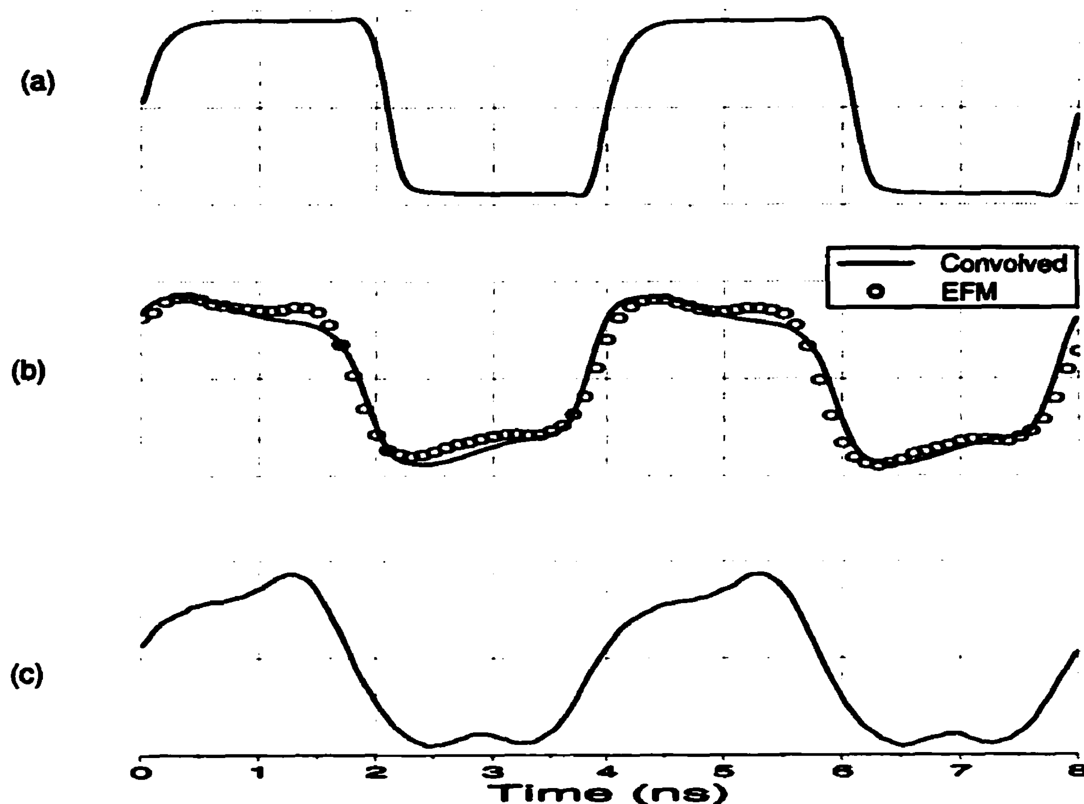

Figure 5.11: Measurement of an 4-bit 0.5 Gb/s digital pattern (1010) at test pads A. Results from (a) Cadence SpectreS simulation, (b) EFM probing and convolution of the simulated waveform shown in (a) with sampling pulse shown in Figure 5.3, (c) active contact probing are shown.

5.4.1 Propagation delay measurement

Measurement of propagation delays in the BiCMOS chain of inverters is demonstrated by probing the test pads A, C, E and G as shown by the circuit schematic in Figure 5.12. The circuit was driven by a 0.5 Gb/s clock waveform and the measured results are shown in Figure 5.12. The sampling increment used in the measurements by the EFM was *100ps*. Results from simulation and contact probing by the active probe are also shown in Figure 5.12. The propagation delay from the results shown in Figure 5.12 are measured at the middle of the high and the low logic levels. The EFM estimates a delay, τ_d, across one inverter at *150ps* while the delay predicted by simulation is on the order of *190ps*. The sig-

nal measured by contact probing was quite distorted by its parasitic capacitive loading and the limited bandwidth of the active probe. An accurate estimate of the propagation delay from these results is difficult and probably inaccurate.

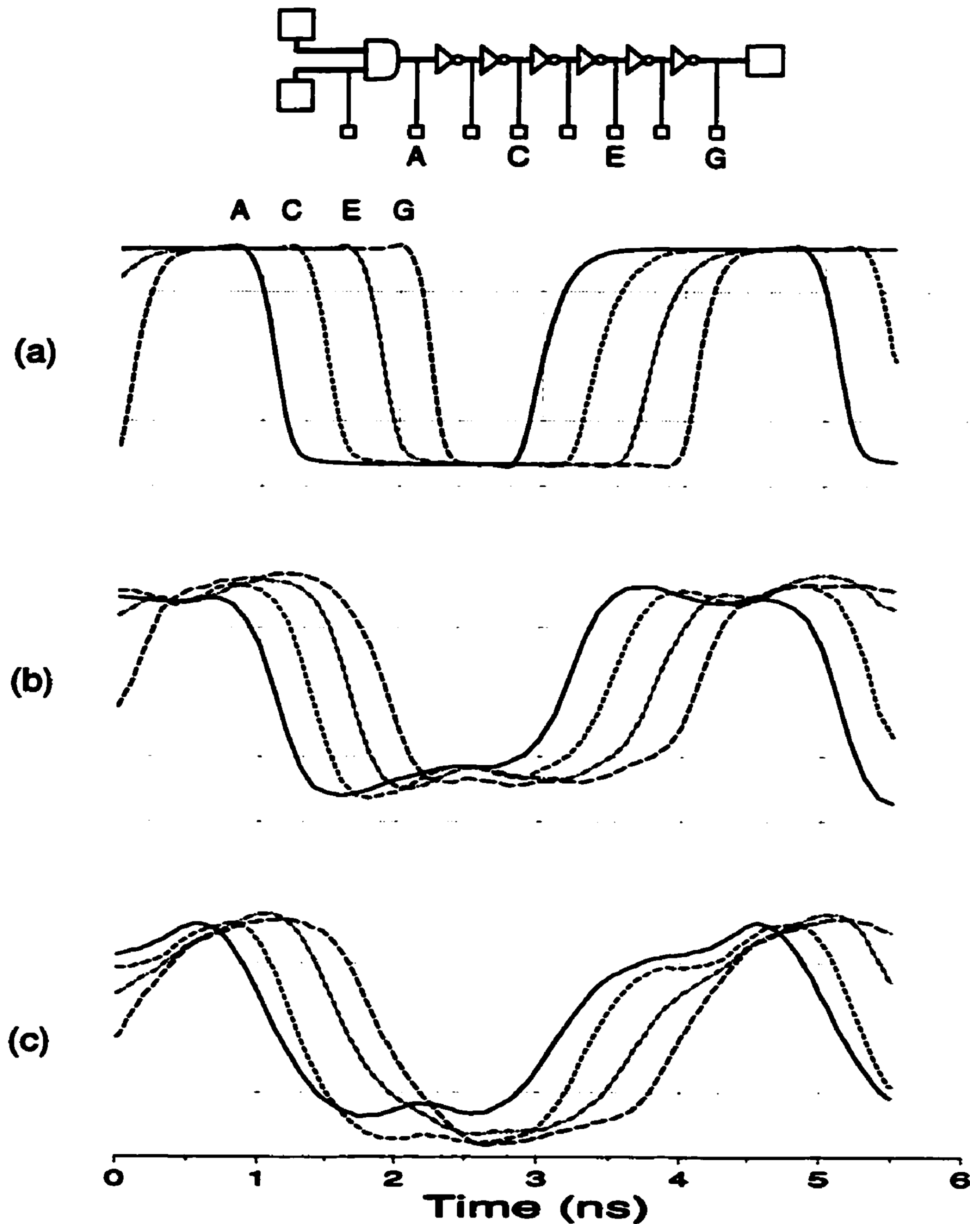

Figure 5.12: Measurement of an 4-bit 0.5 Gb/s digital pattern (1010) at test pads A, C, E and G. Results from (a) Cadence SpectreS simulation, (b) EFM probing and (c) active contact probing are shown.

It is surprising to note that the propagation delay, τ_d, predicted from simulation is larger than that measured by the EFM instrument. For the results shown in Figure 5.12(a) the entire circuit was simulated with all parasitics including the interconnect lines leading to the probe pads. The parasitic capacitance of a typical interconnect line in the design, as extracted by the simulator, is about *40fF*. This is comparable to the load, about *47fF* (Source: the BiCMOS library literature), from the gate capacitance of one inverter. The circuit was again simulated without the test pads and the interconnect lines leading to them. The waveforms at pads A, C, E and G are shown in Figure 5.13. The propagation delay measured from these results is *125ps*. The disparity between the EFM and simulation result could thus be due to an improper modeling of the parasitics of the interconnect lines which affects the predicted timing of the circuit.

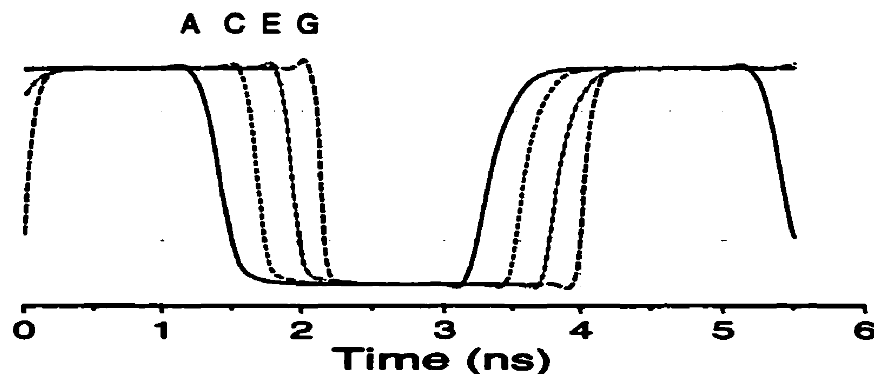

Figure 5.13: Cadence simulation of the inverter chain without test pads. Simulated waveforms at points in the circuit corresponding to test pads A, C, E and G are shown.

5.5 Instrument Sensitivity

The instrument sensitivity in terms of its delay measurement capability and the noise level in the measurement are discussed in this section. To investigate the delay measurement capability, the EFM instrument was used to sample one of the rising edges of the result presented Figure 5.6 where a microstrip interconnect line was used as the test circuit. The HP80000 signal generator was used to introduce simulated edge delays of 0, 10, 20, 50

and 100 ps, these corresponding to the five curves shown in Figure 5.14. The EFM measurement was made with a sampling increment of *10ps*. An enlarged view of the waveforms is also displayed and indicates that delay measurements are possible to within *10ps*. The RMS time jitter in the electronics of the EFM instrument was estimated to be less than *10ps* in these measurements.

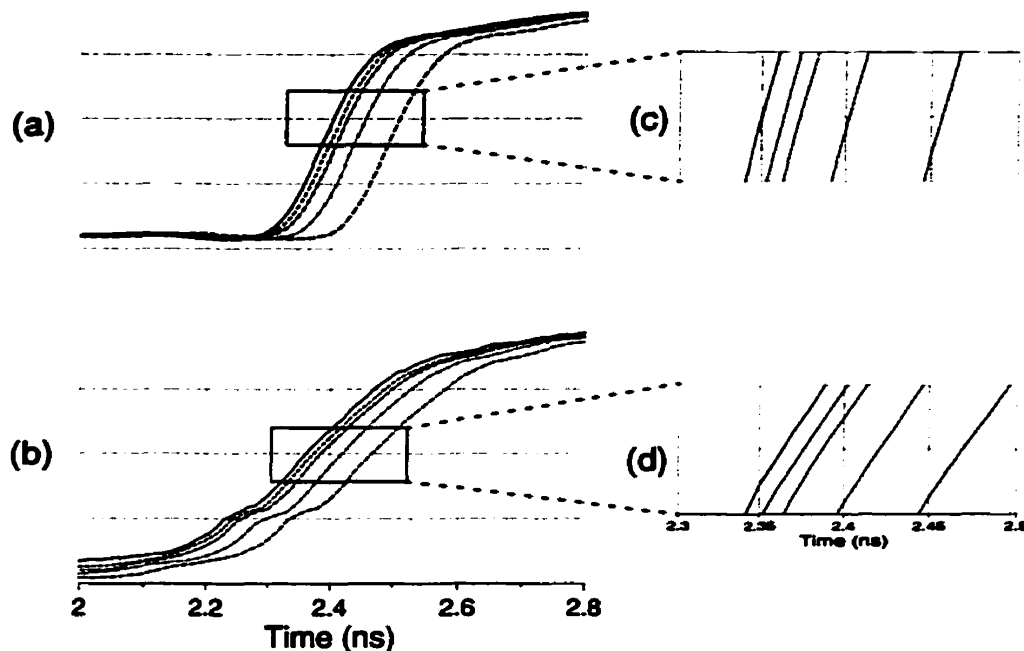

Figure 5.14: Delay measurements on a microstrip interconnect line. (a) Applied signal delayed by 10, 20, 50 and 100 ps as measured on an oscilloscope, (b) waveforms measured by EFM, (c) and (d) show an enlarged view of the curves in (a) and (b).

Errors in the measurement by the EFM are introduced by the jitter in the instrument and noise. Possible noise sources are coupling to probe from external sources, noise in the deflection sensor and probe vibration due to thermal noise. To examine these effects, one of the rising edges in Figure 5.13 was repeatedly measured. In Figure 5.15, the results from ten such measurement are plotted and they show an excellent repeatability in the performance of the instrument.

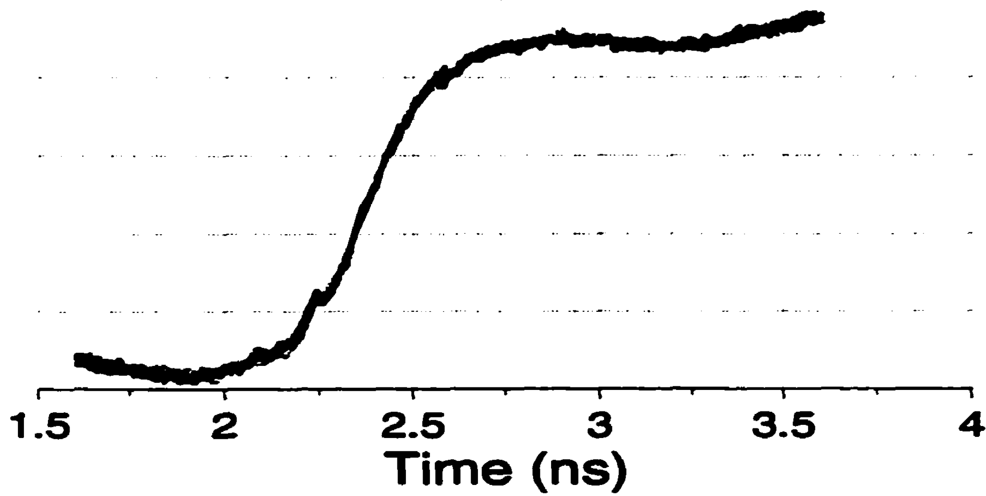

Figure 5.15: Plots showing the results obtained by measuring the rising edge of the same signal 10 times.

The noise level in these measurement was further investigated by repeatedly sampling the same point of a signal with the delay between the circuit and the sampling signals kept constant. The interconnect line was driven by a 0.5 Gb/s square waveform with the logic levels switching between *1.0V* to *-1.0V*. The points corresponding to time, t = *1.9ns* and *3.0ns* were sampled 51 times and the results are shown in Figure 5.16(a). They are plotted over the waveform obtained from sampling the signal over a time span of *8ns*.

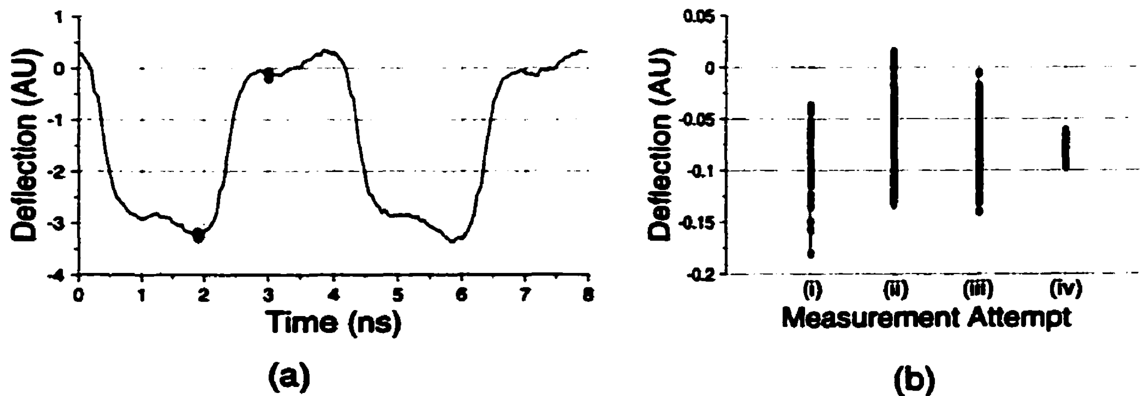

Figure 5.16: (a) Repeated sampling (51 times) of points at time t = 1.9 ns and 3.0 ns plotted over 0-8ns pattern. (b) Set of four measurements (101 data points in each) at t = 3.0 ns with data in (i), (ii) and (iii) averaged 1000 times and those in (iv) averaged 10000 times. (AU stands for arbitrary units).

Noise is a function of the measurement bandwidth as pointed out in section 3.5.3. In the measurement system each sample is averaged many times before recording the data. Figure 5.16(b) shows four measurement attempts made where the point in time corresponding to *3.0ns* was measured 101 times. In the first three attempts each data point is averaged 1000 times which correspond to a measurement bandwidth estimated at *0.8Hz* resulting in a RMS noise level of about *30mV*. The data in the fourth attempt were obtained with a measurement bandwidth of *0.08Hz* (averaged 10000 times). The RMS noise in this case was estimated at *9mV* which is in agreement with $\Delta V_{rms} \propto \sqrt{B}$ where B is the measurement bandwidth. The instrument is typically operated at a *0.8Hz* measurement bandwidth.

In order to calculate the theoretical voltage sensitivity of the measurement technique, the force at the resonant frequency of the cantilever probe is written as

$$F_z\big|_{f_r} \approx \left[-\frac{\partial C}{\partial z}\cdot\frac{\delta}{T}\cdot K\cos\left(2\pi f_r t\right)\right] \bullet v_c(x, y, t = \tau) \qquad [5.6]$$

using [5.3]. The width of the sampling pulse, δ, is assumed to be much smaller than the time period of the sampling signal, T, and the pulse duty cycle (δ/T) in these measurements is estimated at *1/32* (*250ps / 8ns*). The parameter K is introduced to account for the amplitude of the sampling pulse and for the square wave modulation employed in the measurement system. Thus, K is estimated at ($1.2*4/\pi$) taking into account the pulse reflection from the open circuited probing tip. The peak pulse amplitude is *0.6V* (from Figure 5.4). The factor $4/\pi$ comes from the first harmonic (at the resonant frequency) of the square wave modulating signal. From [5.6], the RMS force at the probe resonant frequency, f_r, is given by

$$\langle F_z^2(f_r)\rangle^{1/2} \approx -\frac{\partial C}{\partial z}\cdot\frac{\delta}{T}\cdot K\cdot\frac{1}{\sqrt{2}}\cdot v_c(x, y, t = \tau) \qquad [5.7]$$

The voltage sensitivity of the measurement technique using equation [3.20] is given by

$$\Delta V_{rms} = \frac{2T}{\delta K|\partial C/\partial z|}\sqrt{\frac{2kk_B T_a}{Q\omega_r}} \qquad V/\sqrt{Hz}. \qquad [5.8]$$

The capacitance derivative is estimated as *50pF/m* assuming a tip-to-sample separation of *1μm* [Bridges 92b]. Using this and typical values for the other parameters of the micromachined probe used in this measurement (Q = *32*, k = *0.064N/m*, and f_r = *12.275KHz*) ΔV_{rms} is estimated as $12.3\text{mV}/\sqrt{Hz}$. A measurement bandwidth of 0.8Hz results in a minimum detectable voltage of *11mV*. This theoretical estimate is in the same order of magnitude as the one measured experimentally.

The effect of timing jitter on the instrument capability was analyzed by repeated sampling of a 0.25Gb/s square wave pattern as shown in Figure 5.17. The waveform was repeatedly sampled at points corresponding to time, t = *1.0, 2.35* and *4.0 ns*. The jitter effect is expected to be more noticeable at a point on the rising or falling edge as compared to the flat portion of the waveform. However, the noise levels measured from these results were of the same level in all three cases. This demonstrates that the jitter effect is small compared to other noise sources in the measurement system.

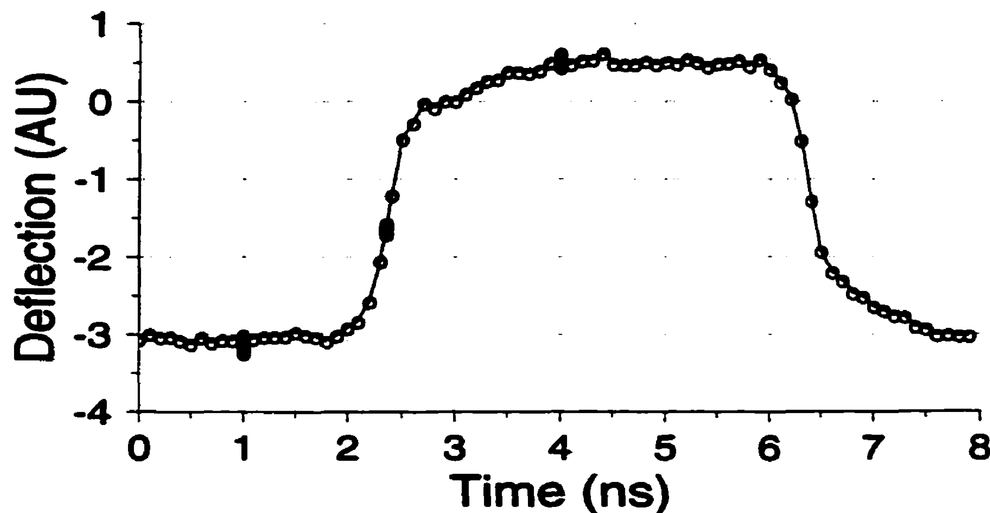

Figure 5.17: Repeated sampling (81 times) of signal at time t = 1.0, 2.35, 4 ns plotted over 8ns long pattern.

Chapter 6

Conclusion

Existing techniques for internal probing of microelectronic circuits were reviewed. Brief descriptions of their operating principles were given and the measurement methods were evaluated in terms of their capabilities and limitations.

An alternative instrument based on the electrostatic force microscope was investigated for on-chip measurements of high frequency signals. The operating principle behind the instrument and its main components were described. The mechanical properties of the cantilever probes and the performance of the deflection sensors were characterized. The performance of the instrument was evaluated in terms of spatial resolution, invasiveness and voltage sensitivity.

A heterodyne technique based on amplitude modulation was described for non-contact measurements of high frequency signals. The use of a nulling technique for absolute vector voltage measurements was implemented. Measurements in the *GHz* range was possible by employing a square wave amplitude modulation in the heterodyne technique. Different schemes were investigated for the implementation of the square wave amplitude modulation using simple and inexpensive microwave components.

A double-path modulation system was implemented and vector voltage measurements were performed at *1GHz* on a simple feed-through microstrip interconnect as well as on the internal nodes of a commercial MMIC low noise amplifier. The EFM results were compared with the measurements obtained using a network analyzer and an active contact

probe and with specification data. Excellent agreement was obtained thus demonstrating the capability of the instrument.

The heterodyne technique for vector voltage measurement was also implemented using an I/Q modulator. This technique enabled considerable simplification and automation of the measurement system. Extensive characterization of the non-linearities in the component would enable complete automation of the measurement method. Vector voltage measurements at *881MHz* were demonstrated on a thru-line and on the internal nodes of a MMIC amplifier. Experimental results were compared with specification data and network analyzer measurements. A fairly good agreement was obtained. The accuracy of vector measurements of small amplitude signals was adversely affected by the direct coupling from the probe to the circuit. A micromachined cantilever probe was employed in the instrument and the coupling capacitance between the probe and the circuit proved to be significant. This effect can be minimised by using properly shielded probe fixtures and by employing probing tips with a longer aspect ratio.

A mixer modulation system was also employed for heterodyne vector voltage measurements. This technique allowed an extension of the frequency range of measurements. Measurements of internal sinusoidal signals at *2GHz* were performed on a MMIC amplifier. The EFM results were compared with those obtained from active contact probing and network analyzer measurements and with specification data. A good agreement was observed for large signals. The measurements of smaller signals were again affected by the probe-circuit parasitic coupling. Vector voltage measurements were also performed at *1.7GHz* on a MHMIC phase shifter. The EFM and active contact probing results compared well with network analyzer measurements at large bias voltages. The return loss of the circuit was found to be dependent on the bias voltage and a better match was obtained with higher magnitude bias voltages.

In vector voltage measurement, the discontinuous probe was matched manually using delay lines. Vector measurements were made at a single frequency at a time. The use of an adjustable electronic phase shifter would enable automatic matching of the probe. Swept

frequency measurements, similar to a network analyzer, would then be possible. For high frequency measurements the probe discontinuity should be carefully analyzed for parasitic effects. An improved probe design with a 50Ω transmission line that reaches the probing end of the cantilever beam would enable higher frequency measurements.

Arbitrary periodic high frequency waveforms were extracted using a heterodyne pulse sampling technique. A high frequency pulse generation system was implemented using simple components. The measurement system was demonstrated by extracting periodic digital patterns on a thru-line and on the internal nodes of a BiCMOS circuit. Digital patterns up to 1Gb/s were measured using the technique. The experiment results compared well with simulated results and those obtained from active contact probing. Propagation delay measurements were also demonstrated on the BiCMOS circuit. The voltage sensitivity was found to be *30mV* with a measurement bandwidth of *0.8Hz*. The delay measuring capability of the instrument was also investigated and measurements were found to be accurate to within *10ps*. The use of a narrower pulse width and a sampling signal with fewer non-idealities can improve the measurement capability of the EFM instrument.

References

[Albrecht 91] T.R. Albrecht, P. Grutter, D. Home, and D. Rugar, "Frequency Modulation Detection using High-Q Cantilevers for Enhanced Force Microscope Sensitivity," *Journal of Applied Physics*, vol. 69, no. 2, pp. 668-673, January 1991.

[Binnig 82] G. Binnig, C.F. Quate, and C. Gerber, "Surface Studies by Scanning Tunneling Microscopy," *Physical Review Letters*, vol. 49, no. 1, pp. 57-61, 5 July 1982.

[Binnig 86] G. Binnig, C.F. Quate, and C. Gerber, "Atomic Force Microscope," *Physical Review Letters*, vol. 56, no. 9, pp. 930-933, 3 March 1986.

[Bloom 94] D.M. Bloom, "Voltage-Contrast Scanning Probe Microscopy," Microelectronic Engineering, vol. 24, pp. 3-9, 1994.

[Bohm 94a] C. Bohm, C. Roths, and E. Kubalek, "Scanning-Force-Microscope Test System for Device Internal Test with High Spatial and Temporal Resolution," *Microelectronic Engineering*, vol. 24, pp. 91-98, 1994.

[Bohm 94b] C. Bohm, C. Roths, and E. Kubalek "Contactless Electrical Characterization of MMICs by Device Internal Electrical Sampling Scanning-Force-Microscopy," *IEEE MTT-S Digest*, pp. 1605-1608, 1994.

[Bohm 96a] C. Bohm, M. Otterbeck, S. Lipp, L. Frey, R. Reuter, A. Leyk, W. Mertin, F. J. Tegude, and E. Kubalek, "Design and Characterization of Integrated Probes for Millimeter Wave Applications in Scanning Probe Microscopy," *IEEE MTT-S Digest*, pp. 1529-1532, 1996.

[Bohm 96b] C. Bohm, J. Sprengepiel, M. Otterbeck, and E. Kubalek, "Voltage Contrast in Submicron Integrated Circuits by Scanning Force Microscopy," *Journal of Vacuum Science Technology B*, vol. 14, no. 2, pp. 842-844, March/April 1996.

[Bridges 92a] G.E. Bridges, T.S Forzley and D.J. Thomson, "Novel Near-Field Probe for On-Wafer Integrated Circuit Measurement," *Microelectronics Journal*, vol. 23, no. 7, pp. 362-369, 1992.

[Bridges 92b] G.E. Bridges and D.J. Thomson, "High Frequency Circuit Characterization using the AFM as a Reactive Near Field Probe", *Ultramicroscopy*, vol. 42-44, pp. 321-328, 1992.

[Bridges 93] G.E. Bridges, R.A Said and D.J. Thomson, "Heterodyne Electrostatic Force Microscopy for Non-Contact High Frequency Integrated Circuit Measurement," *Electronics Letters*, vol. 29, no. 16, pp. 1448-1449, 5 August 1993.

[Bridges 94] G.E Bridges, R.A. Said, M. Mittal, and D.J. Thomson, "Sample Waveform Measurement in Integrated Circuits using Heterodyne Electrostatic Force Microscopy," *Review of Scientific Instruments*, vol. 65, no. 11, pp 3378-3381, November 1994.

[Bridges 95] G.E Bridges, R.A. Said, M. Mittal, and D.J. Thomson, "High-Frequency Pattern Extraction in Digital Integrated Circuits using Scanning Electrostatic Force Microscopy," *Journal of Vacuum Science Technology B*, vol. 13, no. 3, pp 1375-1379, May/June 1995.

[Campbell 93] A.N. Campbell, E.L. Cole, B.A. Dodd, and R.E. Anderson, "Internal Current Probing of Integrated Circuits using Magnetic Force Microscopy," *IEEE International Reliability Physics Symposium*, pp. 168-177, 1993.

[Cascade] Cascade Microtech. Application Notes. Beaverton, Oregon, USA.

[Clauberg 90] R. Clauberg, H. Beha, A. Blacha, and H.K. Seitz, "Picosecond Photoemission probing of Integrated Circuits: Capabilities, Limitations and Applications," *IBM Journal of Research and Development*, vol. 34, no. 2-3, pp. 173-187, March/May 1990.

[Corsi 94] F. Corsi, D. De Venuto, and G.V. Pottacci, "Primary Electron Pulse Shape Evaluation in an EBT System," *IEEE Transactions on Instrumentation and Measurement*, vol. 43, no. 4, August 1994.

[CRC1] Communications Research Centre (D. Roscoe, private communication), Ottawa, Canada.

[CRC2] Communications Research Centre (B. Clarke, private communication), Ottawa, Canada.

[David 93] G. David, P. Bussek, A. Auer, F.J. Tegude, and D. Jager, "Electro-Optic Probing of RF Signals in Submicrometre MMIC Devices," *Electronics Letters*, vol. 31, no. 25, pp. 2188-2189, 7th December 1995.

[DI] Digital Instruments. Santa Barbara, California, USA.

[Dimarogonas 96] A.D. Dimarogonas. *Vibration for Engineers*. po. 470, Prentice-Hall, Inc., NJ, USA, 1996.

[Gao 95] Y. Gao and I. Wolff, "A Miniature Magnetic Field Probe for Measuring Fields in Planar High Frequency Circuits," *IEEE MTT-S Digest*, pp. 1159-1162, 1995.

[Gao 96] Y. Gao and I. Wolff, "A Simple Electric Near Field Probe for Microwave Circuit Diagnostics," *IEEE MTT-S Digest*, pp. 1537-1540, 1996.

[GGB] GGB Industries Inc., Naples, Florida, USA.

[Gupta 79] K.C. Gupta, R. Garg, and I.J. Bahl. *Microstrip Lines and Slotlines*, Artech House, Inc., Dedham, Massachusetts, USA, 1979.

[Ho 93] F. Ho, A.S. Hou, and D.M. Bloom, "High-Speed Integrated Circuit Probing Using a Scanning Force Microscope Sampler," *Electronics Letters*, vol. 30, no. 7, pp. 560-562, 31 March 1994.

[Hou 92] A.S. Hou, F. Ho, and D.M. Bloom, "Picosecond Electrical Sampling Using a Scanning Force Microscope," *Electronics Letters*, vol. 28, no. 25, pp. 2302-2303, 31 March 1994.

[HP] Hewlett-Packard. HP80000 Data Generator System Installation Guide, October 1994.

[Huang 92] Y. Huang, J. Slinkman, and C.C. Williams, "Modeling of Impurity Dopant Density Measurement in Semiconductors by Quantitative Scanning Force Microscopy," *Ultramicroscopy*, vol. 42-44, pp. 298-303, 1992.

[Huang 96] Y. Huang, C.C. Williams, and M.A. Wendman, "Quantitative Two-Dimensional Dopant Profiling of Abrupt Dopant Profiles by Cross-Sectional Scanning Capacitance Microscopy," *Journal of Vacuum Science Technology A*, vol. 14, no. 3, pp. 1168-1171, May/June 1996.

[Jones 87] K.E. Jones, E.W. Strid and K.R. Gleason, "mm-Wave Wafer Probes Span 0 to 50 GHz," *Microwave Journal*, vol. 30, pp. 177-183, April 1987.

[Kim 93] J. Kim, S. Williamson, J. Nees, S. Wakana, and J. Whitaker, "Photoconductive Sampling Probe with 2.3ps Temporal Resolution and 4μV Sensitivity," *Applied Physics Letters*, vol. 62, no. 18, pp. 2268-2270, May 1993.

[Lai 95] J. Lai, M. Chandrachood, A. Majumdar, and J.P. Carrejo, "Thermal Detection of Device Failure by Atomic Force Microscopy," *IEEE Electron Device Letters*, vol. 16, no. 7, pp. 312-315, July 1995.

[Lee 90] T.T. Lee, T. Smith, H.C. Huang, E. Chauchard, and C.H. Lee, "Optical Techniques for On-Wafer Measurements of MMICs," *Microwave Journal*, vol. 33, pp. 91-102, May 1990.

[Leyk 95] A. Leyk, C. Bohm, D.W. van der Weide, and E. Kubalek, "104GHz Signals Measured by High Frequency Scanning Force Microscope Test System," Electronics Letters, vol. 31, no. 13, pp. 1046-1047, 22 June 1995.

[Mertin 93] W. Mertin, C. Roths, F. Taenzler, and E. Kubalek, "Probe-Tip Invasiveness at Indirect Electro-Optic Sampling of MMIC," *IEEE MTT-S Digest*, pp. 1351-1354, 1993.

[Meyer 88] G. Meyer and N.M. Amer, "Novel Optical Approach to Atomic Force Microcopy," *Applied Physics Letters*, vol. 53, no. 24, pp. 2400-2402, 12 December 1988.

[Meyer-Arendt 89] J.R. Meyer-Arendt. *Introduction to Classical and Modern Optics*, pp. 414. Prentice Hall, Inc., NJ, USA, 1989.

[Mini-Circuits] Mini-Circuits. Product Catalogs. Brooklyn, New York, USA.

[Mittal 94] M. Mittal. *Internal Node Microwave Monolithic Integrated Circuit Diagnostic Using Scanning Electrostatic Force Microscopy.* MSc. Thesis, Department of Electrical and Computer Engineering, University of Manitoba, Winnipeg, Manitoba, Canada, 1994.

[Mueller 94] U. Mueller, C. Boehm, J. Sprengepiel, C. Roths, E. Kubalek, and A. Beyer, "Geometrical and Voltage Resolution of Electrical Sampling Scanning Force Microscopy," *IEEE MTT-S Digest*, pp. 1005-1008, 1994.

[Mulhern 91] P.J. Mulhern, T. Hubbard, C.S. Arnold, B.L. Blackford, and M.H. Jericho, "A Scanning Force Microscope with a Fiber-Optic-Interferometer Displacement Sensor," *Review of Scientific Instruments*, vol. 62, no. 5, pp. 1280-1284, May 1991.

[Muralt 87] P. Muralt, H. Meier, D.W. Pohl, and H.W.M. Salemink, "Scanning Tunneling Microscopy and Potentiometry on a Semiconductor Heterojunction," *Applied Physics Letters*, vol. 50, no. 19, pp. 1352-1354, 11 May 1987.

[Nechay 95] B.A. Nechay, F. Ho, A.S. Hou, and D.M. Bloom, "Applications of an Atomic Force Microscope Voltage Probe with Ultrafast Time Resolution," *Journal of Vacuum Science Technology B*, vol. 13, no. 3, May/June 1995.

[Neubauer 90] G. Neubauer, S.R. Cohen, G.M. McClelland, D. Horne, and C.M. Mate, "Force Microscopy with a Bidirectional Capacitance Sensor," *Review of Scientific Instruments*, vol. 61, no. 9, pp. 2296-2308, September 1990.

[Neumeister 94] J.M. Neumeister and W.A. Duckel, "Lateral, Normal, and Longitudinal Spring Constants of Atomic Force Microscopy Cantilevers," *Review of Scientific Instruments*, vol. 65, no. 8, pp. 2527-2531, August 1994.

[Nonnenmacher 92] M. Nonnenmacher, M.P. O'Boyle, and H.K. Wickramasinghe, "Surface Investigation with a Kelvin Probe Force Microscope," *Ultramicroscopy*, vol. 42-44, pp. 268-273, 1992.

[Noruttun 97] D. Noruttun, G. Bridges, R. Said, D. Thomson, R. Qi, S. Cheung, and T. Lam, "Failure Analysis of High Speed Microelectronics using Non-Contact Probing," *Proceedings of the 1997 Micronet Annual Workshop*, pp 53-54, Ottawa, Canada, March 1997.

[Osofsky 92] S.S Osofsky and S.E. Schwarz, "Design and Performance of a Non-Contacting Probe for Measurements on High-Frequency Planar Circuits," *IEEE Transactions on Microwave Theory and Techniques*, vol. 40, no. 8, pp. 1701-1708, August 1992.

[Pfeifer 95] T. Pfeifer, H-M Heiliger, H.G. Roskos, and H. Kurz, "Generation and Detection of Picosecond Electric Pulses with Freely Positionable Photoconductive Probes," *IEEE Transactions on Microwave Theory and Techniques*, vol. 43, no. 12, pp. 2856-2862, December 1995.

[PSI] Park Scientific Instruments. Mountain View, California, USA.

[Putman 92] C.A.J. Putman, B.G. De Grooth, N. F. Van Hulst, and J. Greve, "A Detailed Analysis of the Optical Beam Deflection Technique for use in Atomic Force Microscopy," *Journal of Applied Physics*, vol. 72, no. 1, pp. 6-12, 1 July 1992.

[Rabjohn 87] G. Rabjohn, J. Wolczanski, and R. Surridge, "High-Frequency Wafer-Probing Techniques," *Canadian Journal of Physics*, vol. 65, no. 8, pp. 850-855, August 1987.

[Relcom] RELCOM. Palo Alto, California, USA.

[Rugar 89] D. Rugar, H.J. Mamin, and P. Guethner, "Improved Fiber-Optic Interferometer for Atomic Force Microscopy," *Applied Physics Letters*, vol. 55, no. 25, pp. 2588-2590, 18 December 1989.

[Rugar 90] D. Rugar, H.J. Mamin, P. Guethner, S.E. Lambert, J.E. Stern, I. McFadyen, and T. Yogi, "Magnetic Force Microscopy: General Principles and Application to Longitudinal Recording Media," *Journal of Applied Physics*, vol. 68, no. 3, pp. 1169-1183, 1 August 1990.

[Said 94b] R.A. Said, G.E. Bridges, and D.J. Thomson, "Scanned Electrostatic Force Microscope for Noninvasive High Frequency Potential Measurement," *Applied Physics Letters*, vol. 64, no. 11, pp. 1442-1444, March 1994.

[Said 94a] R.A. Said, G.E. Bridges, and D.J. Thomson, "Non-invasive Scanned Probe Potentiometry for Integrated Circuit Diagnostics," *IEEE Transactions on Instrumentation and Measurement*, vol. 43, no. 3, pp. 469-474, June 1994.

[Said 95] R.A. Said. *Scanning Force Potentiometry Techniques for Semiconductor Circuit Characterization*. PhD Thesis, Department of Electrical and Computer Engineering, University of Manitoba, Winnipeg, Manitoba, Canada, 1995.

[Said 96] R. Said, D. Noruttun, R. Qi, G.E. Bridges, and D.J. Thomson, "Internal Sampling Oscilloscope for High Frequency Circuit Testing," *Proceedings of the 1996 ANTEM Conference*, pp 527-530, Montreal, Canada, August 1996.

[Sarid 91] D. Sarid. *Scanning Force Microscopy with Applications to Electric, Magnetic and Atomic Forces*. pp. 133. Oxford University Press, Inc., 200 Madison Avenue, N.Y., N.Y. 1991.

[Saurenbach 90] F. Saurenbach and B.D. Terris, "Imaging of Ferroelectric Domain Walls by Force Microscope," *Applied Physics Letters*, vol. 56, no. 17, pp. 1703-1705, April 1990.

[Shafai 94] C. Shafai, D.J. Thomson, and W. Simard-Normandin, "Two Dimensional Delineation of Semiconductor Doping by Scanning Resistance Microscopy," *Journal of Vacuum Science Technology B*, vol. 12, no. 1, pp. 378-382, January/February 1994.

[Shakouri 93] M.S. Shakouri, A. Black, B.A. Auld, and D.M. Bloom, "500GHz GaAs MMIC Sampling Wafer Probe," *Electronics Letters*, vol. 29, no. 6, pp. 557-558, 18th March 1993.

[Song 94] J. Song, D.J. Thomson, and G.E Bridges. *Super Luminescent Diode based Optical Fiber Interferometer for Force Microscopy.* Tech. Rep. UMECE TR-94-102, University of Manitoba, Canada, 1994.

[SRS] Stanford Research Systems. DS-345 Function Generators. Sunnyvale, California, USA.

[Stern 88] J.E. Stern, B.D. Terris, H.J. Mamin, and D. Rugar, "Deposition and Imaging of Localized Charge on Insulator Surfaces using Force Microscope", *Applied Physics Letters*, vol. 53, no. 26, pp. 2717-2719, December 1988.

[Strid 86] E.W. Strid, "26 GHz Wafer Probing for MMIC Development and Manufacture," *Microwave Journal*, vol. 29, pp. 71-82, August 1986.

[T-Tech] T-Tech, Inc. *Quick Circuit* Milling Machine, Atlanta, Georgia, USA.

[Takahashi 95] H. Takahashi, S. Aoshima, And Y. Tsuchiya, "Sampling and Real-Time Methods in Electro-Optic Probing Systems," *IEEE Transactions on Instrumentation and Measurement*, vol. 44, no. 5, October 1995.

[TI-LNA] Texas Instruments. *TGA 8061 Application Notes*, Dallas, Texas, USA.

[Weaver 91] J.M.R. Weaver and D.W. Abraham, "High Resolution Atomic Force Microscopy Potentiometry," *Journal of Vacuum Science and Technology B*, vol. 9, no. 3, pp. 1559-1561, May/June 1991.

[Wickramasinghe 89] H.K. Wickramasinghe, "Scanned-Probe Microscopes," *Scientific American*, pp. 98-105, October 1989.

[Wiesendanger 94] R. Wiesendanger. *Scanning Probe Microscopy and Spectroscopy*. pp. 219. Cambridge University Press, Cambridge, Great Britain. 1994.

[Wiesenfeld 90] J.M. Wiesenfeld, "Electro-Optic Sampling of High Speed Devices and Integrated Circuits," *IBM Journal of Research and Development*, vol. 34, no. 2-3, pp. 141-161, March/May 1990.

[Winkler 90] D. Winkler, R. Schmitt, M. Brenner, and B. Lischke, "Flexible Picosecond Probing of Integrated Circuits with Chopped Electron Beams," *IBM Journal of Research and Development*, vol. 34, no. 2-3, pp. 189-203, March/May 1990.

[Yu 93] R. Yu, M. Reddy, J. Pusl, S. Allen, M. Case, and M. Rodwell, "Full Two-Port On-Wafer Vector Network Analysis to 120GHz using Active Probes," *IEEE MTT-S Digest*, pp. 1339-1342, 1993.